EXAMINATION OF VARIOUS TECHNIQUES FOR MEASURING WIND VELOCITIES USING CLEAR-AIR RADARS, WITH EMPHASIS ON VERTICAL WIND MEASUREMENTS

by

JORGE LUIS CHAU

B.S., University of Piura, Perú, 1991

M.S., University of Colorado, 1995

A thesis submitted to the

Faculty of the Graduate School of the

University of Colorado in partial fulfillment

of the requirements for the degree of

Doctor of Philosophy

Department of Electrical and Computer Engineering

1998

This thesis for the Doctor of Philosophy degree by

Jorge Luis Chau

has been approved for the

Department of

Electrical and Computer Engineering

by

Ben B. Balsley

Arthur D. Richmond

Date _____

The final copy of this thesis has been examined by the signators, and we find that both the content and the form meet acceptable presentation standards of scholarly work in the above mentioned discipline.

Chau, Jorge Luis (Ph. D., Electrical Engineering)

Examination of various techniques for measuring wind velocities using clear-air radars, with emphasis on vertical wind measurements

Thesis directed by Research Professor Ben B. Balsley

In this work, I examine various techniques for measuring wind velocities using clear-air radars. Special emphasis has been given to the vertical wind measurements. All the observations were obtained in the lower atmosphere (below 20 km) using the Jicamarca 50 MHz radar system near Lima, Perú. I have concentrated my efforts on: (a) examining different radar techniques for horizontal wind estimation, (b) improving the understanding of angle-of-arrival radar measurements, and (c) comparing a number of techniques for the measurement of the vertical wind velocities.

I have measured horizontal wind velocities by a variety of both time- and frequency-domain spaced antenna (SA) techniques. Comparisons of these techniques for both zonal and meridional components have been carried out in a statistical sense. Two sets of data were analyzed under both "quiet" (low wind, low variability) and "active" (high wind, high variability) conditions. I have found that the simpler techniques that assume horizontally isotropic scattering compare well with the more complicated full correlation analysis techniques. Briefly, while all SA techniques give essentially the same horizontal wind direction, considerable discrepancies are apparent in the wind speed, particularly above 15 km.

With regard to technique comparisons for vertical velocity, two types of measurement techniques using a concurrent data set are compared. Both Zenith (i.e., using a vertically-directed single beam) techniques and spaced antenna (SA) techniques are compared using a concurrent 5-day data set obtained with a special configuration of the Jicamarca 50 MHz radar antenna. Two separate Zenith

techniques are implemented using different antenna beam-widths (a 0.85° and a 3° beam-width). Different SA approaches are also implemented using a: "quasi" Doppler beam swinging (DBS) approach and four "classical" SA approaches. "Classical" SA approaches make use of horizontal wind and AOA measurements to get "corrected" vertical velocities. Statistical results are presented for both quiet and active conditions.

DEDICATION

To Jenny and Tiffany

ACKNOWLEDGMENTS

First of all, I would like to thank my lovely wife (Jenny) and daughter (Tiffany), without their constant support throughout these years the END of this thesis would have not been possible.

Special thanks to my advisor Ben Balsley for his continuous help not only in the scientific arena but also in personal matters. His simple way of facing the obstacles has contributed to ease my "complicated" way of work.

Ronald Woodman patiently taught me the "teje y maneje" of gathering experimental radar data. Discussions on how to implement the experiments and on how to process and interpret the data, has enormously contributed to the success of this research.

I would like to thank Susan Avery, Zoya Popovic, Art Richmond, Koni Steffen and Judy Curry for being members of my committee.

The Jicamarca staff is also acknowledged. The games of ping-pong and "fulbito" and the "historical" anecdotes contribute to a pleasant "hands-on" experience. The dedication and knowledge of Fernando Villanueva made possible the gathering of good and uninterrupted data (you still own me a "cebiche").

Thanks also to my officemates. Luis "the coolest one" Liziola for sharing his "cool" IDL routines, especially "make_x.pro". Meche Huaman (my "Comadre") for bringing "el toque femenino" to the office, for her time and support, and of course for her delicious "platillos". Mike Jensen for bringing the diversity to the group (Kites = Radars?).

Frequent and fruitful discussions with Peter May helped me to investigate better the SA techniques and AOA measurements. I also would like to thank Denise

Thorsen for reading and commenting on a portion of this work (AOA chapter) and Art Richmond for his careful reading of early manuscripts.

Brief but important discussions with the following scientists are greatly appreciated: Erhan Kudeki (narrow-wide beam idea, SA implementation), Jürgen Röttger (specular echoes and AOA measurements), Dick Doviak (scattering theory, AOA determination), Richard Lataitis (SA techniques), Christopher Holloway (SA techniques), Greg Nastrom (vertical velocity issues), Robert Palmer (vertical velocity issues), Mike Jones (gravity waves), Rod Frehlich (statistical uncertainties).

Finally, I would like to thank my parents for their support and time in the final stages of this "journey".

The work in this thesis was funded through grants from the National Science Foundation under agreements ATM-9214657 and ATM-9614700.

CONTENTS

FIGURES

FIGURE

TABLES

TABLE

CHAPTER 1

INTRODUCTION

Atmospheric vertical motions are very important in predicting and understanding atmospheric processes that are responsible for our weather and climate. For example, it is fairly common knowledge that the upward displacement of a mass of saturated air will produce precipitation. However, vertical motions are usually so small that when meteorologists use the term "wind" they usually are referring to the horizontal motions. This usage is in line with the Webster's dictionary definition of wind as: "A natural motion of the air; especially, a noticeable current of air moving in the atmosphere parallel to the earth's surface."

Throughout this thesis, we will be discussing and comparing atmospheric results obtained by VHF clear-air radars in the lower atmosphere (below 22 km), where most meteorological processes are confined. Clear-air radars offer the unique capability of directly measuring vertical motions. However, vertical motions obtained by these radars are not incorporated into numerical weather prediction (NWP) models; rather the vertical velocity is a derived field (Dunn [1991]). One can expect model performances to improve as clear-air radar measurements of the vertical velocity become more widely available to, and accepted by, the meteorological community. In contrast, horizontal winds measured by clear-air radars are more accepted and are being incorporated in meteorological models. For example, wind observations at Christmas Island (central Pacific) are being used routinely by the National Meteorological Center (NMC) and the European Centre for Medium Range Weather Forecasts (ECMWF) in their analysis and forecast products (Gage et al. [1988]).

The term clear-air radar can be misleading; although radar studies of the

atmosphere via scattering from clear-air refractive index fluctuations are the norm, VHF radars are also sensitive to strong precipitation (e.g. Currier et al. [1992]; May and Rajopadhyaya [1996]). These types of radars are also called: (a) wind profilers, because the measurement of vertical profiles of the three-dimensional wind is their main application, or (b) ST radars for the height range they cover (lower stratosphere and troposphere). However, clear-air radars are not limited to meteorological applications. They are also used in middle atmospheric and ionospheric studies. Moreover, the first wind measurements by these type of radars were done at the ionospheric facility (at that time) of Jicamarca, Perú in 1974 (Woodman and Guillén [1974]). A comprehensive history of clear-air radar studies can be found in Hardy and Gage [1990].

Given the meteorological community's skepticism of radar measured vertical velocities, this thesis represents a concentrated effort to examine different ways atmospheric vertical motions can be obtained by clear-air radars. The core of this work, i.e., the comparisons of vertical velocity techniques, is covered in Chapter 6. In order to better understand vertical motions, we first present some of their important aspects in Chapter 2. In this chapter, we outline their importance, methods for measuring them and some of their characteristics (from theory and from observations). In addition, we summarized the current concerns with vertical velocities measured by clear-air radars. Then, we focus in on the vertical velocity problem in Chapter 3. In Chapter 2, we also see the importance of accurate horizontal wind velocity and angle-of-arrival measurements, in a specific type of vertical velocity technique. Since these techniques could offer new insights into the vertical velocity accuracy, we have dedicated Chapter 4 to compare a variety of techniques that measure horizontal wind velocities (zonal [u] and meridional [v] components), and Chapter 5 to improve the understanding of angle-of-arrival measurements. Finally, a summary of results and future activities is outlined in Chapter 7.

CHAPTER 2

CLEAR-AIR VERTICAL MOTIONS

The vertical velocities we study throughout this thesis are those obtained by VHF radars under clear-air conditions. Obviously, clear air does not contain such awesome phenomena as tornados or baseball-sized hail found in severe storms. Clear-air structure, nevertheless, is rich in meteorological events that can lead to the development of these storms.

Much of our current knowledge of the role of vertical velocity in weather and climate is a result of the observational analysis of large-scale synoptic wind fields obtained using non-radar methods (see Section 2.2.1). Such analyses are highly smoothed and subject to uncertainties, and give us no information about temporal and spatial variability on smaller scales. Local vertical velocities, on the other hand, contain contributions from convection, waves, turbulence. Instantaneous vertical velocities can be as large as several meters per seconds. These local influences (e.g., orography) are likely to dominate the much weaker synoptic-scale vertical motions, which are typically in the range of a few centimeters per second.

In this section we summarize the importance of knowing the vertical motions of clear air. We also provide a review of the current methods of inferring or directly-measuring this quantity. We include some characteristics of the vertical wind obtained from theory and from observations, along with a review of the current concerns of the accuracy of direct radar measurements of the vertical velocity. Our summary covers synoptic-scale (days to weeks, 100 to 500 km) and mesoscale (minutes to days, 1 to 100 km) vertical motions.

2.1 On the importance of knowing vertical atmospheric motions

In the the following paragraphs we discuss the importance of vertical motions in: meteorology, atmospheric research, air pollution, modeling and horizontal wind estimation.

2.1.1 The importance of vertical air motions in meteorology

Rising air is typically associated with cloudy conditions and precipitation. Subsiding air, on the other hand, produces adiabatic heating and clearing conditions. Because descending air is compressed and warmed, cloud formation and precipitation are unlikely in an anticyclone and "fair" weather can usually be expected with the approach of a high pressure system. Cyclones and "stormy" weather, on the other hand, can be expected with the approach of a low pressure system.

Vertical air motion is one of the most important variables for many forecasting applications and much of synoptic meteorology is involved with the prediction of vertical velocity. Many forecasting "rules of thumb" have their roots in the dynamical equations for vertical motion (e.g. strong positive vorticity advection equates to upward vertical motion). If a forecaster could monitor the vertical velocity field in real time, his predictions of severe weather would be improved. It is within the zero-to-six-hour time frame where credible forecasts of severe weather have the greatest impact on protecting life and property, and it is precisely within this time frame that continuous observations of the vertical velocity can best help weather forecasting. Given continuously available vertical velocity profiles, a forecaster could better monitor storm movement and development in real time (the now-casting approach).

Although mesoscale vertical motion (e.g., motions due to cold fronts and baroclinic storm systems) plays a significant role in the dynamics of synoptic-scale systems, it is not resolved by conventional data analysis (radiosonde and forecasting tools).

It may be possible to deduce horizontal divergence from the vertical profile of vertical velocity at a single station. This idea relies upon the relationship between horizontal divergence and the vertical gradient of vertical velocity for an incompressible fluid, $\nabla_H \cdot \boldsymbol{u} = -\partial w/\partial z$. Thus, to the extent that a representative profile of vertical motions is obtainable at a single station, it would be possible to infer the vertical divergence profile from the vertical velocity profile (Gage [1990]). Horizontal divergence is a very important dynamical quantity in weather forecasting.

2.1.2 The importance of vertical air motions in atmospheric research

A partial listing of atmospheric research topics that involves vertical motions follows:

• Studies of orographic effects. Vertical velocity measurements from clear-air radars show that the morphology of atmospheric activity in the troposphere and lower stratosphere correlates well with the presence/absence of major mountain ranges. Examples of these studies (Ecklund et al. [1985]; Balsley and Carter [1989]; Liziola and Balsley [1997]; Nastrom and VanZandt [1996]) include the generation of mountain waves, the propagation of these waves into the upper atmosphere under specific mean conditions, the retardation/acceleration of waves by wave breakdown, and the detrimental effects of atmospheric gravity waves on the accuracy of wind measurements.

• Knowledge of the vertical motions in mesoscale convective systems (MCSs) is important for understanding the physical processes operating within these systems (e.g. precipitation production, stratiform and convective region dynamics). One also needs to understand how these features interact with the large-scale environment through the transport of heat, moisture and momentum (e.g. Houze [1989]).

• Knowledge of the vertical wind field is of considerable importance in understanding the troposphere-stratosphere exchange processes crucial for climate change processes.

• In tropical regions, vertical velocity information helps to understand the important scale interactions that take place between convection and large scale circulations (e.g., Walker circulation). For example, Gage et al. [1991a] presented an example of a possible correlation of El Niño events with measurements of mean vertical motions.
• In atmospheric wave studies, vertical velocity measurements are important in: (a) quantifying large-scale transport and thermal signatures of wave-driven residual circulation at both lower and upper levels, (b) identifying the magnitude, nature, and spectral character of various wave and turbulence processes, and (c) assessing wave field anisotropy and forcing via vertical fluxes of horizontal momentum.

2.1.3 The importance of vertical air motions in air pollution

Many extensive and long-lived air pollution events can be linked directly to temperature inversions that develop in regions of sinking air ($w < 0$) associated with slow-moving anticyclonic centers of high air pressure.

Moreover, at night time, when incoming solar radiation is smallest, low level temperature inversions tend to prevail. If such conditions are accompanied by light winds, then diffusion rates will be particularly small and pollutants emitted from ground sources will accumulate in the inversion layer.

2.1.4 The importance of vertical air motions in modeling

On an extended scale, both vertical velocity and horizontal velocity data from a network of clear-air radars could be used in the initialization and updating of regional National weather prediction (NWP) models. Vertical velocity measurements are also important for the verification of numerical-model-derived kinematic, thermodynamic and micro-physical fields.

For example, given measurements of the synoptic-scale vertical velocity, a single station could provide time histories of the vertical motion that exist within baroclinic storm systems. This capability would permit more realistic descriptive

models to be formulated.

Modeling studies presented by Starr and Cox [1985] showed ascent on the mesoscale to synoptic-scale is quite important to the evolution of macroscopic cloud properties. Macroscopic characteristics such as cloud thickness, aerial coverage and optical depth have been shown to be quite sensitive to the large-scale vertical motion.

2.1.5 The importance of vertical air motions in horizontal wind estimation

At times and places where vertical motions are appreciable, vertical velocity measurements are necessary in order to obtain more accurate measurements of horizontal winds using clear-air radars. For example, Weber et al. [1992] concluded that, in the presence of large vertical velocity disturbances, hourly averaged horizontal winds can be sometimes be less meaningful than the measurements made more frequently at intervals of a few minutes.

2.2 Methods of Estimating the Vertical Wind Velocity

The methods of estimating clear-air vertical motions can be classified conveniently into: non-radar and clear-air radar methods. These methods are described separately in the following paragraphs.

2.2.1 Non-radar methods

Non-radar methods for deriving the vertical motion, w, are those used typically by the meteorological community. Such methods involve large-scale measurements, and provide indirect estimates from synoptic analysis. Intercomparisons of these standard methods began half a century ago (Panofsky [1946]) and are a continuous topic of research (Durran and Snellman [1987]; Dunn [1991]).

Non-radar methods of vertical velocity estimation are usually applied using isobaric coordinate systems, i.e., using pressure (p) as the vertical coordinate instead

of height (z), so that $\omega(p) = \mathrm{D}p/\mathrm{D}t$ is inferred rather than $w(z) = \mathrm{D}z/\mathrm{D}t$. These two vertical velocity quantities are related through,

$$\omega = -\rho g w \tag{2.1}$$

where ρ is the air density and g is the acceleration due to gravity. This expression may not be a good approximation when: (a) the ageostrophic wind component is relatively large (e.g. as in most boundary layer events); (b) the local pressure tendency is relatively large (e.g. in an intensifying system); (c) the atmosphere is not in hydrostatic equilibrium (e.g. in a thunderstorm). Some of the most common non-radar methods of estimating w are outlined below.

2.2.1.1 Adiabatic method

This method is based on the assumption that changes of state of atmospheric air are adiabatic. Techniques that use this method are: the advective technique, the single-station technique, the graphical technique and the isentropic technique. The adiabatic method is inaccurate in situations where strong diabatic heating is present, i.e., in storms in which heavy rainfall occurs over a large area (e.g. Panofsky [1946]; Holton [1992]; Bluestein [1992]). One disadvantage of this method is that determination of the local rate of change of temperature ($\partial T/\partial t$) is required at very close intervals.

2.2.1.2 Kinematic method

This method depends on the principle of conservation of mass as expressed by the equation of continuity (e.g. Panofsky [1946]; Pedder [1981]). Application of the kinematic method requires knowledge of the horizontal divergence of the horizontal velocity. In order to determine this divergence the partial derivatives are generally estimated from the fields of zonal and meridional velocities by using finite-difference approximations. However, a 10% error in evaluating one of the horizontal

wind components can easily cause the estimated divergence to be in error by 100%. Despite the inaccuracy of the divergence measurements, kinematic computations of w profiles based upon unsmoothed wind data do contain useful information. This is because divergence errors are vertically correlated. Synoptic-scale vertical motions computed kinematically and adjusted by the O'Brien scheme (O'Brien [1970]) have been shown to correlate well with cloud and precipitation patterns (Bluestein [1992]).

2.2.1.3 Methods using Quasi-Geostrophic theory

These methods of diagnosing the vertical velocity requires only information on the geopotential distributions at a single time, and utilizes both the vorticity equation and the thermodynamic equation. Quasi-geostrophic methods make use of the omega equation (e.g Dunn [1991]). The omega equation unlike the continuity equation, provides a method of estimating w that does not depend on observations of the ageostrophic wind. In fact, direct wind observations are not required at all, nor does the omega equation require information on the temperature tendency, as required in the adiabatic method. Accurately estimating the terms needed in these methods from noisy observational data can be quite difficult (e.g. Holton [1992]; Barnes [1986]; Durran and Snellman [1987]).

2.2.2 Clear-air radar methods

Clear-air radars typically observe weak backscatter from half-wavelength components of turbulent inhomogeneities in the atmospheric radio refractive index (e.g. Woodman and Guillén [1974]). At low tropospheric altitudes the radar refractive index is usually dominated by the humidity term. Above mid-tropospheric altitudes, the refractive index is dominated by turbulence in the thermal field. The intensity of backscattered power depends upon both the magnitude of the background gradient of refractive index as well as the intensity of the turbulence. Sometimes the spatial distribution of radar refractive index in clear-air can be associated

with meteorological phenomena such as waves, turbulent layers, fronts, etc. The most important radar techniques that measure vertical velocities of these "invisible" targets are described below.

2.2.2.1 The VAD (Velocity Azimuth Display) technique

In the VAD technique, the zenith angle (θ) is fixed and the antenna is swept in azimuth at a constant rate (e.g. Peterson and Balsley [1979]). Data at many altitudes are obtained essentially simultaneously as the radar antenna is swept 360° in azimuth. For a homogeneous and time-invariant wind field within the field of view at a given altitude, the radial velocity so obtained will vary sinusoidally with azimuth. The amplitude of the sine curve is equal to the horizontal wind speed and the phase is related to the wind direction. In addition, the offset of the sinusoid from zero velocity (C_0) is proportional to the vertical velocity ($C_0 = w \cos\theta$).

When divergence of the horizontal wind is important, the offset C_0 becomes

$$C_0 = \left[w + \frac{z_0}{2} \tan^2\theta (\nabla_h \cdot \boldsymbol{u}) \right] \cos\theta \tag{2.2}$$

where $\nabla_h \cdot \boldsymbol{u}$ is the divergence term and z_0 is the height range (Doviak and Zrnič [1993], p. 312). The divergence and vertical velocity can be calculated directly if VAD measurements are made at two or more different zenith angles. This modified VAD approach is known as EVAD (extended VAD, e.g. Larsen et al. [1991]).

Vincent and Reid [1983] suggested a variation to this technique, using at least two coplanar beams pointed symmetrically relative to vertical. Measuring the radial velocities at angles θ and $-\theta$, and assuming the mean horizontal and vertical velocities are the same in both beams, the mean vertical velocity at height range z_0 can be obtained from

$$\bar{w}(z_0) = \frac{\bar{v}_r(\theta, z_0) + \bar{v}_r(-\theta, z_0)}{2\cos\theta} \tag{2.3}$$

where $\bar{v}_r$ represents the mean radial velocity at the respective beams.

2.2.2.2 The Zenith technique

The Zenith technique can be thought of as the vertical portion of the Doppler beam swinging (DBS) method. The DBS method is the radar method currently used by most clear-air radars. In the Zenith technique the antenna remains fixed at the zenith. Since the radial velocity measured in this mode is the vertical velocity, one need to make no assumptions regarding homogeneity, particularly if narrow beam antennas are used. Current concerns on the accuracy of Zenith techniques are covered in Section 2.4.

2.2.2.3 Spaced antenna techniques

All spaced antenna techniques require at least three non-collinear, vertically-directed receiving antennas. The vertical velocity is obtained from

$$v_r = u \sin \Theta_u + v \sin \Theta_v + w(1 - \sin^2 \Theta_u - \sin^2 \Theta_v)^{1/2} \tag{2.4}$$

where u, v are the horizontal velocity components (zonal and meridional), $\sin \Theta_u$, $\sin \Theta_v$ are the zonal and meridional direction cosines of the "effective" beam direction, and v_r is the radial velocity (positive going away from the radar). If these angles are measured from the phase of the cross-spectra functions (e.g. Van Baelen and Richmond [1991]; Palmer et al. [1991]; Larsen et al. [1992]), or from cross-correlation functions (e.g. Röttger and Ierkic [1985]; Larsen and Röttger [1991]), the vertical velocity obtained is often called corrected velocity (Larsen and Röttger [1991]). However, if different beam directions are obtained with the SA system, through post beam set (PBS, Röttger and Ierkic [1985]) or through post statistics steering (PSS, Kudeki and Woodman [1990]), the vertical velocity can be inferred from Equation 2.4. More on these techniques is presented in Section 6.2.

2.2.2.4 One form of the adiabatic method

One form of the adiabatic method described in Section 2.2.1.1 above, can be used with wind and temperature data from a single radar station. The station needs to have both a clear-air radar and a radio acoustic sounding system (RASS) (Nastrom and Warnock [1994]; Yamamoto et al. [1996]). With this type of station, wind and temperature measurements are available with the necessary temporal sequence to use this method on a routine basis. For example, Yamamoto et al. [1996] have shown preliminary measurements of vertical velocities obtained with the MU radar-RASS system. Assuming hydrostatic equilibrium, Yamamoto et al. obtained the vertical velocity from

$$w \approx -\frac{g}{N^2}\frac{\partial \ln T}{\partial t} \tag{2.5}$$

where g is gravity, T is temperature and N is the Brunt-Väisälä frequency. Yamamoto et al. found that "frequency spectra of the derived vertical wind were more consistent with a gravity wave model than those spectra calculated from direct measurements of the vertical wind".

In addition, some of the discussed non-radar methods could be applied to a network of clear-air radars, such as the National Oceanic and Atmospheric Administration (NOAA) wind profiler demonstration network (WPDN) (Lee et al. [1995]; Mace et al. [1995]; Mace and Ackerman [1996]). For example, Mace et al. [1995] have shown how to use a kinematic method with a network of wind profilers.

Most of the clear-air radar techniques outlined above can also be applied to other ground-based remote sensing instruments for vertical velocity measurements. However, these instruments do not rely on the backscatter echoes of refractive index irregularities and are not under consideration here. For example, coherent Doppler lidars use a Zenith technique but backscattered echoes are from atmospheric aerosol particles (e.g. Frehlich et al. [1994]). As a second example, Doppler weather radars uses a VAD technique and their targets are mainly hydrometeors (e.g. Doviak and

Zrnič [1993]).

2.3 Vertical Velocity Characteristics

In the following sections we outline some theoretical and observed characteristics of the vertical velocity under different conditions.

2.3.1 Vertical velocity characteristics from theory

Typically, vertical velocity is constrained to be zero at the ground and is assumed to be zero at the tropopause (Bluestein [1992], p. 296). The former is required by the kinematic lower boundary condition; the latter is a dynamic requirement owing to to the reversal of the quasi-horizontal temperature gradient. In spite of this assumption, the tropopause itself does undulate up and down. If w is nonzero, its sign is often the same at all levels in a column of the troposphere. The levels where $\partial w/\partial z$ reverses are called the levels of non-divergence (LND). Although one LND is most often expected, no physical principle is violated if there are more than one. In addition, rising motions ($w > 0$) above a LND must be accompanied by convergence below and compensating divergence aloft. Similarly, sinking motions ($w < 0$) must be accompanied by divergence below and convergence aloft (continuity equation in a non-compressible fluid).

Over a sloping terrain, w may not be zero due to "orographic forcing". This forcing depends on both the horizontal wind speed and the steepness of the slope of the surface. This effect may be so large that orographic effects may completely mask the effects of dynamical forcing.

Many temperature inversions in the lower atmosphere are attributable to sinking motion. When air subsides ($w < 0$), its temperature increases at the dry adiabatic lapse rate $\approx 10°$/km. In some instances, the subsidence continues to a particular level and then the air diverges horizontally. The more rapid the decrease of temperature with height, the more unstable the air, and the greater the vertical

motions.

Based upon basic physics principles, when a volume of air is warmer than its surroundings, the upward pressure-gradient force exceeds the downward gravity force. This results in a positive buoyancy and the air rises; conversely when a volume of air is colder than its surroundings it is negatively buoyant and it sinks (Battan [1979]).

The largest theoretically-determined vertical velocities averaged over a season are on the order of a few millimeters per second. These values occur in the equatorial zone and are associated with the ascending branch of the Hadley cell. Vertical velocity magnitudes decrease considerably in the lower stratosphere. At greater altitudes, the mean vertical motions driven by wave forcing are expected on theoretical grounds to be considerably larger, but nevertheless are ≈ 1000 time less than characteristic horizontal mean motions (Fritts and Luo [1995]).

The conceptual model of Mattocks and Bleck [1986] predicts the existence of a transverse circulation around a jet streak. A jet streak is an isotach (line of constant wind speed) maximum embedded in a jet, that is an "intense" (> 15 m s^{-1}), "narrow" (width is at least a half to an order of magnitude less than its length) quasi horizontal or horizontal current of wind that is associated with strong vertical shear (Bluestein [1992]). According to this model, vertical velocities should show ascent above the jet and descent below if measured in the entrance region on the cold side of the jet streak or on the warm side in the exit region. An oppositely directed vertical circulation would be expected for observations made in the warm (entrance) and cold (exit) quadrants.

2.3.2 Some observed vertical velocity characteristics

2.3.2.1 Mean vertical motions

Excepting convective conditions, mean vertical velocities are usually much less than horizontal velocities in the free atmosphere. Large-scale vertical motions are usually less than few centimeters per second. Such small motions are traditionally inferred from synoptic analysis of the large-scale wind field (Panofsky [1951]; Dunn [1991]). Belt and Fuelberg [1982] found that vertical velocities calculated with sub-synoptic scale data were as much as 6 cm s^{-1} larger than those calculated with synoptic scale data in the same conditions.

Assuming that long-term mean vertical velocities ($\bar{w}$) at a single station are representative of large-scale vertical motions, Nastrom et al. [1985] and Larsen et al. [1988] have compared radar-observed mean vertical velocities to vertical velocities obtained from analyzed wind fields produced by the National Meteorological Center (NMC) and the European Centre for Medium-Range Weather Forecast (ECMWF), respectively. Nastrom et al. [1985] concluded that the single-station radar measurements were representative of the synoptic-scale vertical velocities, particularly when the measurements were not contaminated too severely by lee waves. This meteorological "noise" can swamp the synoptic-scale signal at times. Although the observed velocities significantly overestimated the calculated velocities, the signs of the two velocities were generally the same. However, the magnitudes of the w measured over a flat terrain (Flatland, Illinois), where the effects of lee waves are not expected, show large discrepancies with predicted values (Nastrom and VanZandt [1994]; Nastrom et al. [1994]). Instead of being very small, the long-term mean vertical velocity ($\bar{w}$) at Flatland is observed to be downward throughout the troposphere, with values > 5 cm s^{-1} when averaged over periods ranging from hours to months, rather than nearly zero as expected. In addition, $\bar{w}$ is usually observed to be slightly upward in the lower stratosphere.

Similar descending patterns in the troposphere and ascending in the lower stratosphere are sometimes seen by radars at other mid-latitude sites. These results have been reported using the MU radar in Japan (Fukao et al. [1991]) and the SOUSY radar in Germany (Yoe et al. [1992]). Both the MU and the SOUSY radar results have been associated to the proximity to the jet stream, where the $\bar{w}$ reversal occurs at a height near the jet stream maximum. However, when the position of the jet is shifted, that is not usually the case, the pattern reverses, i.e., ascent in the troposphere and descent in the lower stratosphere. It is worth pointing out, that the maximum vertical velocities obtained with the SOUSY radar were a factor of 3 greater than those measured with the MU radar.

The results at tropical sites (Pohnpei [Western Pacific], Christmas Island [Central Pacific] and Piura [Eastern Pacific]), show also similar patterns to those most often seen at mid-latitudes (Balsley et al. [1988]; Gage et al. [1992]; Huaman and Balsley [1996]), except that the stratospheric results at Pohnpei show downward velocities under clear conditions. However, the magnitudes of the tropical mean vertical velocities are very much smaller than those observed at mid-latitudes. "Adiabatic warming associated with the tropospheric subsidence appear to be in approximate balance with calculated radiative cooling to space in the clear atmosphere, but ascending motions appears to be somewhat larger than is needed to balance diabatic heating in the lower stratosphere, assuming a clear atmosphere free of ice or other aerosols" (Gage et al. [1991a]).

2.3.2.2 The variability of vertical velocity

Non-averaged vertical velocity observations in the atmosphere are dominated by short-period internal gravity waves with typical rms amplitudes (σ_w) of 10 to 20 cm s^{-1} (Gage [1990]). Non-averaged w measurements are much more easily realized than measurement of the much smaller long-term mean vertical motions that

requires careful averaging of large numbers of individual measurements (e.g. Gage et al. [1991a]; Balsley et al. [1988])

Motions due to atmospheric turbulence and waves are usually the major source of variance of the measured non-averaged vertical velocities. Observed vertical velocities due to various wave and turbulence motions, while generally smaller than associated horizontal velocities, are far larger (more than 2 orders of magnitude) than the mean vertical motions. Although clear-air radars appear to be suitable for these measurements, the effect of this variability has to be considered in some measurements of synoptic (i.e. longer term) scale vertical velocities (e.g. Nastrom et al. [1985]).

Vertical observations presented by Ecklund et al. [1985] showed, mainly, two conditions: quiet ($\sigma_w < 20$ cm s^{-1}) and active ($\sigma_w > 20$ cm s^{-1}). The variations observed during the active periods, appear to be related to orographic waves that develop as wind flows over rough terrain. Presumably, tilting isentropic surfaces associated with lee waves are responsible for the increased variance (Gage and Nastrom [1990]). The vertical velocity spectra under active conditions are distinctly different from the flat spectra observed under quiet conditions. Specifically, the vertical velocity spectrum under active conditions contains much more low-frequency energy.

Comparisons of w obtained over rough terrain (Platteville, Colorado) and those obtained over a flat terrain (Flatland, Illinois) indicate that terrain indeed does dominate many of the features of mesoscale variability in w. Moreover, the results over a flat terrain do not show the enhanced vertical velocity spectrum (VanZandt et al. [1991]). Also, vertical velocities measured at mid-latitudes (Nastrom and VanZandt [1994]) show much bigger daily variance than those obtained at equatorial sites (Huaman and Balsley [1996]).

An overall view of the variability of vertical velocity fields over Poker Flat,

Alaska, is contained in Balsley and Garello [1985]. Briefly, the short-period vertical velocity variance profiles for the winter months show little change with altitude below 15 km. Above 15 km the profile increases steadily. During the summer months, vertical variance below 12 km is enhanced above the winter values and above 12 km the summer values are lower. The low level increase during the summer months could be due to convection. The decrease at higher altitudes could be due to a wave-breaking process.

2.4 Current concerns with the Zenith technique

As we mentioned earlier, the Zenith technique is currently employed by most clear-air radars. For example, the vertical wind has been measured across the tropical Pacific at all Tropical Pacific Profiler Network (TPPN) sites from the inception of the TPPN network (Balsley et al. [1988]; Gage et al. [1991b, 1991a]; Huaman and Balsley [1996]). In the absence of appreciable cloud cover, typical mean vertical velocities show a slight downward subsidence (≈ -1 cm s^{-1}) throughout the troposphere. While this value is small and difficult to measure, it is, as discussed above, consistent with atmospheric cooling by radiation to space under clear-air conditions. Velocity values under more convective conditions depart greatly from these subsidence values, particularly in the region of so-called "hot towers" associated with deep tropical convection, where upward vertical motions can easily exceed 15 m s^{-1} (i.e. values well over three orders of magnitude larger than clear-air subsidence).

In spite of these reasonable results, there exist a series of puzzling mean vertical velocity measurements (e.g. Balsley and Riddle [1984]; Fukao et al. [1991]; Nastrom and VanZandt [1994]) that bring into question the accuracy of these direct (Zenith technique) radar measurements. For example, Fukao et al. [1991] found that in most of the cases they studied, the direction of the vertical circulation near a Jet stream could not be explained by the slope of the time-averaged potential

temperature surfaces alone, since the combination of the horizontal winds and the slopes of the isentropic surfaces would have led to a prediction of a circulation directly opposed to that observed.

In contrast to these puzzling observations, many case-studies have shown that "instantaneous" (< 5 min averaged) radar vertical motions are consistent with the associated meteorological mesoscale events, such as the cases presented by Low [1996]; May and Rajopadhyaya [1996]; Ralph et al. [1993]; Nastrom et al. [1990a]. These case studies have provided convincing evidence for the applicability of vertical winds, particularly of the "instantaneous" and mesoscale studies. For example, Ralph et al. [1993] observed consistent vertical motions and pressure perturbations associated with a ducted gravity wave.

Ascertaining the validity of vertical velocity measurements is extremely difficult. This difficulty arises because of the lack of a definitive w to compare with. The standard meteorological techniques for estimating the vertical motions (Section 2.2.1) involve derivations from large-scale synoptic analysis, so that such techniques obviously return a broad-scale temporal and spatial average. Comparisons between these techniques and the Zenith radar technique have been made, and show reasonable agreement (Nastrom [1984]; Nastrom and VanZandt [1994]), although there can be contamination from lee-wave effects near mountains (Nastrom et al. [1985]; Larsen et al. [1988]) or from heavy rain (Balsley et al. [1988]). Moreover, geophysical variability places a limit of about 2 cm s^{-1} on clear-air mean vertical motions, averaged over an hour or more (Nastrom et al. [1990b]).

The most often considered factors that could contaminate vertical velocities obtained by Zenith techniques, are outlined in the following paragraphs.

2.4.1 Antenna beam pointing inaccuracies

Only a slight off-vertical tilt of the beam (less than 0.1°) will produce a major contamination of the ≈ 1 cm s^{-1} measured vertical wind component by the ≈ 10 m s^{-1} horizontal wind. In a first attempt to examine the effects of antenna pointing problems in vertical wind measurements, Huaman and Balsley [1996] made a series of measurements using the Piura (Perú) profiler. This site is the eastern terminus of the TPPN. They found that initial measurements of the vertical wind at Piura had been made using a slightly off-vertical antenna beam. The calculated angle between the true vertical and the antenna pointing direction was extremely small (0.057°). In spite of this, they were able to demonstrate that the contribution of the horizontal wind using this slightly-tilted (2° half-power beam-width) antenna was sufficient to produce almost a factor of two error in the mean vertical wind measurements. The antenna was modified to correct this problem, and the resulting mean vertical wind profiles compared very favorably with comparable profiles at other TPPN sites. Huaman and Balsley [1996] concluded that: (a) such small pointing errors can contaminate long-term mean vertical wind data, and (b) VHF radars are indeed capable of measuring the mean vertical wind with the requisite accuracy in the **tropics**, provided that one is very careful with the antenna phasing.

2.4.2 Tilted refractive index structures

In general, it can be assumed that anisotropic refractive index structures, are not horizontally stratified and are tilted at small angles (e.g. Röttger [1984]; Röttger et al. [1990b]). This tilt may be the result of the presence of waves (e.g. Gage et al. [1981]; Muschinski [1996]) as well as due to baroclinic disturbances. Although these measured tilt angles are typically small ($\approx 1° - 2°$), the difference between the true vertical velocity and the radial velocity in a nominally vertical beam can be quite significant, as shown by Larsen and Röttger [1991] and Palmer et al.

[1991]. The effects of tilted layers are expected to be proportional to the antenna beam-width (e.g. Muschinski [1996]), i.e., the smaller the beam-width the smaller the contamination on the directly-measured vertical velocity. However, if the tilt angles can be measured, a "corrected" vertical velocity could be obtained (Röttger and Ierkic [1985]). Higher-frequency radars do not suffer from aspect sensitivity effects and, therefore, may avoid some of the problem associated with VHF vertical velocity measurements.

2.4.3 Gravity waves

Nastrom and VanZandt [1994] suggested that the dominant effect causing "apparent" unreasonably large mean vertical motions at mid-latitudes is the effect of small changes in the refractive index induced by gravity waves with a vertical component of propagation. In waves with upward energy propagation (downward phase propagation), the vertical velocity and static stability are negatively correlated; thus, regions of downward-moving air have higher reflectivity on a statistical basis in such waves and will produce apparent downward velocities. This hypothesis is independent of the antenna beam-width. The Nastrom and VanZandt studies incorporated two mid-latitude profilers: (a) the Flatland profiler located near Urbana, Illinois, and (b) a second profiler temporarily located at Liberal, Kansas. They reported much larger subsidence values than those observed at equatorial sites (Balsley et al. [1988]; Gage et al. [1991a]). Their hypothesis has been supported by Hoppe and Fritts [1995] using data from echoes obtained near the polar summer mesopause. The effects of gravity waves on vertical velocities would be also seen by other radar methods (SA, VAD, etc).

2.4.4 Wind field gradients

Recently Palmer et al. [1997a] and Larsen and Palmer [1997], have shown how gradients in the wind field could affect vertical velocity and angle-of-arrival

(AOA) measurements. The effects of divergence on vertical velocity measurements using the Zenith technique, are a function of the beam-width, divergence value, and altitude. These biases are proportional to antenna beam-width, i.e., the smaller the beam-width, the smaller the bias. Divergence will also affect the AOA measurements. Nonetheless, "the bias in the vertical beam radial velocity measurements produced by divergence has the same form and the same effect as the bias that would be expected for aspect-sensitive scatter and inclined refractivity layers" (Larsen and Palmer [1997]). Larsen and Palmer have also shown that vorticity will affect the AOAs but will not bias the vertical velocities. However, if these affected-by-vorticity AOAs are utilized to correct an "unbiased" vertical velocity using Equation 2.4, the corrected vertical motion will be biased by these "fictitious" AOAs.

CHAPTER 3

FOCUSING IN ON THE VERTICAL VELOCITY PROBLEM

Given the significant discrepancies in vertical velocity measurements by different radar techniques, particularly in the long-term mean values, we have implemented a variety of techniques for measuring atmospheric vertical motions. All of these measurements have been obtained concurrently using the Jicamarca VHF radar. Our goals are to intercompare the different techniques and to study the validity of various explanations that attempt to account for vertical velocity discrepancies (Chapter 6).

Two Zenith techniques have been implemented for these studies. One technique uses a very narrow antenna beam-width, while the other uses a wide antenna beam-width. Both beams are nearly collocated (the distance between the two antennas is about 65 m from center-to-center). Since both techniques make use of orthogonal polarizations, their measurements can be considered independent. Using these two antenna beam-widths, we study two possible causes of vertical velocity discrepancies that depend on the antenna beam-width, i.e., tilted refractive index structures and wind field divergence.

We have also implemented a series of SA techniques. Most of these techniques (the so-called SA "classical" techniques) correct estimates of vertical velocity that have been contaminated by horizontal velocity "leakage". This leakage is associated with both the antenna pointing inaccuracies as well as with the existence of tilted refractive index structures. Note that other type of SA techniques infer vertical velocities by using a "quasi" DBS approach in a multi-beam configuration. The usage of many beams allows the averaging out of effects that depend on beam-pointing

direction.

Gravity wave effects are not directly tested in the measurements. This is mainly because wave dynamics over Jicamarca (near the Equator) are expected to be much different than conditions present at mid-latitudes. For example, the hourly mean variance at the Piura ST radar ($\approx$ 1000 km North of Jicamarca) is $\approx$ 20 times less than in mid-latitudes (Huaman and Balsley [1996]). Using Nastrom and VanZandt [1994] expressions for the effects of gravity waves, vertical velocity biases near the Equator should be a fraction of a centimeter per second.

Since the corrected vertical velocity estimates obtained by the classical SA methods require the measurement of horizontal velocities and AOAs (see Equation 2.4), we first study the accuracy of these two measurements. Studies of horizontal velocities (Chapter 4), given the large number of SA techniques found in the literature, help us to determine which horizontal velocity techniques are most appropriate to vertical velocity corrections.

During these horizontal velocity comparisons, in view of the lack of an absolute standard, we face the problem of using a reference profile. A good choice would have been to use the widely-accepted DBS measurements. Unfortunately, DBS measurements were not obtained as part of these studies. This omission was because of the relatively small maximum angles of the oblique beams ($< 6^\circ$) at Jicamarca. Tsuda et al. [1986] have shown that for angles $< 10^\circ$ under anisotropic scattering conditions, the DBS horizontal velocity will be underestimated because the effective beam direction will be closer to zenith than the real beam direction. This underestimate is caused by the anisotropic angular pattern of the scattering/reflecting inhomogeneities (aspect sensitivity). Therefore, we have arbitrarily chosen one of the most commonly used full correlation analysis technique as a reference.

The AOA studies that will be discussed in Chapter 5 will help us to: (1)

correctly interpret the AOA measurements obtained with SA systems, and (2) properly use the measurements in vertical velocity corrections. For example, we will study the geometrical effects suggested by Vincent et al. [1987] and May [1993] on AOAs measured with "non-collocated" (or bistatic) SA systems.

CHAPTER 4

A STATISTICAL COMPARISON OF HORIZONTAL WINDS OBTAINED BY A VARIETY OF SPACED ANTENNA TECHNIQUES USING THE JICAMARCA VHF RADAR

4.1 Introduction

Horizontal wind velocity profiles can be measured in the troposphere and lower stratosphere using very high frequency (VHF) radars. There are two main methods that can be used in these measurements. One of these methods, the Doppler or Doppler Beam Swinging (DBS) method (Balsley [1981]), uses three or more narrow beams pointed in different directions. In this method, the wind velocity vector is determined by measuring the Doppler shift of the signal arising from the radial motion of the refractive index variations in the sampled scattering volume. The DBS method is used by most operational wind profilers (e.g. Strauch et al. [1984]; Gage et al. [1991b]). The second method, called the spaced-antenna (SA) method, was originally developed to look at ionospheric returns (Briggs et al. [1950]) and uses a vertically-directed antenna for transmission and three or more horizontally spaced receiving antennas (Larsen and Röttger [1989]; Hocking et al. [1989]). The SA method makes use of the fact that backscattered signal is the diffraction pattern of the illuminated refractive index irregularities. This diffraction pattern moves across the ground at twice the velocity of the scatterers. Normally, winds are calculated from the signals detected by each of the three (or more) antennas using correlation techniques (e.g. Briggs [1984]; Meek [1980]). Since the diffracted signal is sampled at more than a single location by this method, it should not be surprising that the amount of information that can be extracted increases. Röttger and Larsen [1990]

give a detailed review of the DBS and SA methods.

Practically speaking, the DBS analysis can only be analyzed by the estimation of the moments of the radial velocity estimates, although the performance of various moment estimators may vary (May et al. [1989]). On the other hand, there is a number of techniques that can be applied to the SA returns. Some of these techniques are variations of the classical approach presented by Briggs [1984]. Other techniques are more closely related to the DBS method in the sense that they obtain the velocity vector from "radial velocities". Examples of such techniques include post beam steering (Röttger and Ierkic [1985]), post statistics steering (Kudeki and Woodman [1990]), and time domain interferometry (Vandepeer and Reid [1995]).

In general, the techniques differ not only in how the signals are interpreted, but also in which domain they are processed (i.e. time or frequency). Frequency-domain techniques offer several advantages over their time-domain counterparts. For example, frequency-domain techniques allow relatively easy removal of undesired frequency contamination such at that resulting from sea clutter, system interference and/or precipitation echoes. Corrections for ground clutter and noise are also simpler in the frequency domain. Moreover, spectral analysis is also computationally more efficient than correlation analysis.

Comparisons of a few SA techniques has been given by Franke et al. [1990], Sürücü et al. [1992] and Holdsworth [1997] using either MF radar results or computer models. Additional comparisons with the VHF MU radar (see Fukao et al. [1990]) have been made by Van Baelen et al. [1991], Sheppard et al. [1993] and Brown et al. [1995].

We present here a comparison of a variety of VHF SA techniques using a total of 13 days worth of data obtained using the multi-module antenna at the Jicamarca Radar Observatory in Perú. These comparisons were made in the troposphere and lower stratosphere and concern only horizontal wind measurements. We have

attempted to quantify the differences of the many SA techniques and to demonstrate some of the specific advantages and disadvantages between them.

A brief introduction to the relevant SA techniques is presented in Section 4.2, along with details of the implementation procedures. A description of the antenna setup and the experimental parameters appears in Section 4.3. Results from two separate observational periods (i.e. "quiet" and "active" wind conditions) are presented in Section 4.4. Explanation of possible causes of differences determined between the techniques is discussed in Section 4.5, and a summary of the results is presented in Section 4.6.

4.2 Spaced-Antenna Techniques

In the literature, one can find a variety of multi-receiver techniques whose differences depend either on how they are implemented (time or frequency domain) or on how the frequency information is used. These techniques have been given different names, e.g., full correlation analysis (FCA), full spectral analysis (FSA), radar interferometry (RI), spatial interferometry (SI), frequency domain interferometry (FDI), time-domain interferometry (TDI), imaging Doppler interferometry (IDI), etc.

To avoid confusion in presenting our results, we will describe briefly only those techniques that use a single-frequency, multiple-receiving antennas, and that are a part of this study.

To infer horizontal winds, the majority of the SA systems calculate the motion of the diffraction pattern across the ground associated with the motions of the atmospheric scatterers in the resolution volume. If the scatterers are assumed frozen, the diffraction pattern is advected with a velocity equal to twice the horizontal wind in that volume ("point source effect", e.g. Briggs [1980]). By observing the maximum value of the cross correlation of signals from several receiver pairs, the wind

can be estimated using the time lag of that maximum. However, the decorrelation of the received signals caused by the relative motion of the scatterers, i.e., those motions arising from turbulent eddies, causes an error that leads to an overestimation of the wind speed. It is at this point that we encounter our first velocity estimator that will result in a so-called "apparent" velocity. Depending on how this decorrelation is treated, the domain used (time or frequency), and/or the assumptions made, one can find different techniques in the literature. We have implemented some of these techniques and classified them by either time or frequency domain techniques

4.2.1 Time-Domain techniques

Time domain techniques dealing with the decorrelation of signals follow essentially a full correlation analysis (FCA). FCA allows not only for the temporal but also for the spatial decorrelation of the diffraction pattern. FCA uses the complex cross-correlation functions (CCF) from all the receiver combinations, and also includes the autocorrelation function (ACF). CCFs are defined in the spatial and temporal domain by:

$$\rho(\varepsilon,\eta,\tau) = \frac{< v^*(x,y,t)\,.\,v(x+\varepsilon,y+\eta,t+\tau) >}{< v^2(x,y,t) >} \tag{4.1}$$

where $v(x,y,t)$ is the voltage measured at time t and at antenna located at (x,y), and $<>$ denotes ensemble averaging. The spatial displacements and time delay are denoted by ε, η, and τ.

Depending upon which functional form of the diffraction patterns is assumed, the following techniques have been described in the literature:

• FCA by Briggs (here: FCAB). Briggs [1984] gives a detailed formulation and a "recipe" to implement this technique. The basic assumption in this case is that contours of equal spatial and temporal correlation of the ground diffraction pattern can be approximated by a family of ellipsoids of the general form:

$$|\rho(\varepsilon,\eta,\tau)| = \rho(A\varepsilon^2 + B\eta^2 + C\tau^2 + 2F\varepsilon\tau + 2G\eta\tau + 2H\varepsilon\eta) \tag{4.2}$$

and, using intersections of the ACF and CCFs, the *A, B, C, H, F, G* parameters are obtained. A a "true" horizontal velocity can be calculated using these parameters.

• FCA by Meek (here: FCAM). This technique has been described by Meek [1980]. The concepts are similar to FCAB, but with a Gaussian correlation function assumed for the magnitude of the CCFs. Only the width of the mean ACF and the positions and magnitudes of the maxima in the CCF are required to calculate a "true" velocity (here: FCAMt). We have implemented this technique by fitting a Gaussian function to the magnitudes of the ACF and CCFs.

• FCA by Kudeki (here: FCAK). Kudeki [1995] derived the following explicit formula

$$|\rho(\varepsilon,\eta,\tau)| = 1 - A\varepsilon^2 - B\eta^2 - C\tau^2 - 2F\varepsilon\tau - 2G\eta\tau - 2H\varepsilon\eta \tag{4.3}$$

which is valid for "small" values of ε, η and τ. Then, using measured CCF samples at, say, $(\varepsilon,\eta,\tau) = (\varepsilon_0,0,0)$, $(0,\eta_0,0)$, ..., $(\varepsilon_0,\eta_0,\tau_0)$, the *A, B, C, F, G, H* parameters can be obtained using a single value decomposition (SVD) solution to the overdetermined set of equations. Knowing these parameters, a "true" velocity can be calculated in a way similar to the FCAB "true" velocity.

• Relaxing the assumption of the elliptical symmetry in the shape of the CCFs, Woodman [1995] arrived at a new approach (here: FCAW) to determine a "true" velocity for statistically isotropic patterns, as well as for anisotropic patterns when the receiving antennas are aligned along the axis of symmetry. For any baseline $\mathbf{d} = (\varepsilon,\eta)$ the intersection of the ACF, $|\rho(0,0,\tau)|$, with the CCF, $|\rho(\varepsilon,\eta,\tau)|$ occurs at a delay, τ_c, and the projection of the wind velocity, $\mathbf{v}$ over $\mathbf{d}$ is given by,

$$v_d = \frac{\mathbf{v}.\mathbf{d}}{2\,d} = \frac{d}{4\tau_c} \tag{4.4}$$

by evaluating the projection of two or more different directions, it is possible to determine the two-dimensional wind vector. Note that Armstrong and Coles [1972] and Briggs and Maude [1978] also used the "crossings" of CCFs to estimate drift velocities.

• Following the work by Doviak et al. [1996], Holloway et al. [1997a] has presented what are essentially two separate time-domain techniques for estimating the wind velocities for horizontally isotropic scattering (i.e., $A = B$ and $H = 0$ in Equation 4.2). One of these techniques uses the crossings of the ACF and the CCFs to determine the wind velocity using Equation 4.4. The other technique uses the ratio of the CCFs to the ACF, $|\rho(\varepsilon, \eta, \tau)|/|\rho(0, 0, \tau)|$, to calculate the wind velocity. Taking the log of this ratio, the slope S of this curve (with respect to time) is given by:

$$S = \beta_h^2 \, d \, v_d \tag{4.5}$$

and its intercept b at the $\tau = 0$ axis is given by:

$$b = -\frac{\beta_h^2 \, d^2}{4} \tag{4.6}$$

where β_h is related to the scale length of the diffraction pattern [Holloway et al., 1997a, Equation 5].

We have implemented two versions of the latter of these two techniques. The first version uses the "raw" ACF and CCFs (here: FCAH(r)) and the projected velocity is obtained using Equation 4.5 and Equation 4.6 and is given by:

$$v_d = -\frac{d \, S}{4 \, b} \tag{4.7}$$

In the second version, Holloway et al. [1997a] fit a Gaussian function to the magnitudes of the ACF and CCFs (here: FCAH(p)), and the projected velocity is given by:

$$v_d = \frac{d\hat{\tau}_p}{2\hat{\tau}_p^2 - 4 \ln (A_d/A_0)\hat{\tau}_c^2} \tag{4.8}$$

where $\hat{\tau}_p$ is the estimated delay to the peak, $\hat{\tau}_c$ is the estimated width, A_d is the magnitude of the Gaussian fitted to the CCF used, and A_0 is the magnitude of the ACF (≈ 1). Once a Gaussian function is assumed, Equation 4.4 and Equation 4.7 are the same and equal to Equation 4.8.

The last time-domain technique that we have implemented is more closely related to the DBS method than to a classical SA (FCA) approach. This technique is called Time-Domain Interferometry (here: TDI) introduced first by Vandepeer and Reid [1995] and modeled later by Thorsen et al. [1997]. This technique is based on the angle-of-arrival (AOA) and Doppler velocity (v_r) measurements from the zeroth and first lags of the CCFs and ACF functions. Note that both the time-domain techniques described before, and the TDI technique can utilize complementary data sets; the former techniques use only the magnitude of the CCFs, while the latter use only the phases. Basically the three-dimensional TDI wind velocity is obtained from a set of equations of the form,

$$v_{r_t} = -(l_t\, u + m_t\, v + (1 - l_t^2 - m_t^2)^{1/2}\, w) \tag{4.9}$$

where u, v and w are the zonal, meridional and vertical components of the wind velocity; v_{r_i} is the radial velocity and l_t and m_t the zonal and meridional direction cosines at some time t. The wind field is then determined from a linear least squares fit to a system of equations similar to Equation 4.9. Since the phases of CCFs are used, a calibration procedure is necessary in order to remove systematic biases in the receiving lines.

4.2.2 Frequency-Domain techniques

Since cross-correlation and cross-spectrum functions (CSFs) of complex receiver signals are Fourier transform pairs, it is expected that there should be frequency-domain estimators analogous to the time-domain techniques.

The first frequency-domain technique we have implemented is the "Radar Interferometry" technique (here: RIV) introduced by Van Baelen and Richmond [1991], where the horizontal wind field is determined from the phase slope of CSFs. By the "shift theorem" of Fourier transforms, one can view the RIV horizontal velocity as the Fourier equivalent of the "apparent" velocity described above, i.e.

the velocity obtained when turbulence is neglected.

The second frequency-domain technique we have implemented is the full spectral analysis (FSA) technique (Briggs and Vincent [1992]; Sheppard and Larsen [1992]). Here, we have used the FSA technique developed by Briggs and Vincent [1992], where they assumed a Gaussian form for the CCF defined in Equation 4.2, and Fourier transformed it to get a CSF. In order to derive the *A, B, C, F, G, H* parameters, determinations of the phase slope, the amplitude, and the width of the CSFs are needed. The FSA analysis, like its time-domain analogous FCA, produces two velocities estimates, namely, an "apparent" and a "true" velocity. The "apparent" velocity is the same as the velocity given by the RIV technique. In the present study, when we mention the "FSA velocity", we are referring to the "true" estimate.

Holloway et al. [1997a] also presents a frequency-domain technique that is valid for horizontally isotropic scattering (here: RIH). The RIH projected velocity is obtained from the expression:

$$v_d = \frac{2\, k_0\, S_\phi\, \sigma_v^2}{\beta_h^2\, d} \tag{4.10}$$

where S_ϕ is the phase slope, σ_v is the width of the cross-spectrum; β_h is a parameter described earlier, and k_0 is the radar wave number. Here, the turbulence contribution is included in σ_v. In the frequency domain, the parameter β_h is obtained by a measurement of S_ϕ, σ_v and the normalized power of the cross spectra (P_d),

$$\beta_h = \frac{1}{d}\left[2\, S_\phi^2\, \sigma_v^2 - 4 \ln P_d\right]^{1/2} \tag{4.11}$$

In the techniques just described (RIV, FSA, RIH), we have fitted a Gaussian function to the magnitude, and a line to the phase slope of the cross-spectra functions. As recommended by Sheppard et al. [1993], we have smoothed the CSF magnitudes in order to prevent excessive fitting failures and to improve the spectral width estimation.

The last frequency-domain technique under study is the post statistics steering (here: PSS) (Kudeki and Woodman [1990]; Palmer et al. [1990]; Sürücü et al. [1992]; Palmer et al. [1993]). PSS like the TDI technique, is more closely related to the DBS method than to a classical SA approach. This technique synthesizes desired beam directions using simple arithmetic operations with measured CSFs. Once the beams are synthesized, the moments can be calculated using a first-moment method (FM) such as the one described by May and Strauch [1989], and the derivation of the wind field is analogous to the DBS method (e.g. Strauch et al. [1984]). The "apparent" beam directions (ignoring aspect sensitivity), are calculated considering the geometry involved, the height sampled and the transmitting and receiving antenna patterns. More details on the implementation of the PSS techniques can be found in Appendix D.

In Table 4.1 we summarize the SA techniques incorporated in our study. We have listed in Table 4.1 technique abbreviations, a reference, the type of horizontal scattering considered, whether turbulence is considered or not, the type of fitting we have performed in the CCFs or CSFs, and the domain. We have calculated the time-domain "apparent"velocities using the parameters from the FCAM technique and have labeled them FCAMa.

4.3 Jicamarca Experiment

We have used the Jicamarca radar for our intercomparison studies. The radar operates at $\approx$ 50 MHz and has an $\approx$ 300 m by 300 m antenna array. The antenna is composed of 64 separate modules. Each module consists of a 12 by 12 array of cross-polarized half-wave dipoles. Figure 4.1 shows the antenna configuration for our measurements. For transmission, we phased four modules (section D) to point precisely vertically, with a one-way half-power beam width (HPBW) of $\approx 4^{\circ}$. Antennas A, B, C were used for reception. Each receiving antenna was

Table 4.1: SA technique abbreviations and some characteristics.

Technique	Reference	Scattering[a]	Turbulence	Fitting	Domain
FCAB	Briggs [1984]	Anisotropic	Yes	None	Time
FCAMa	Briggs [1984]	Isotropic[b]	No	Gaussian	Time
FCAMt	Meek [1980]	Anisotropic	Yes	Gaussian	Time
FCAK	Kudeki [1995]	Anisotropic	Yes	None	Time
FCAW	Woodman [1995]	Isotropic[b]	Yes	None	Time
FCAH(r)	Holloway et al. [1997a]	Isotropic[b]	Yes	None	Time
FCAH(p)	Holloway et al. [1997a]	Isotropic[b]	Yes	Gaussian	Time
TDI	Vandepeer and Reid [1995]	Anisotropic	Yes	None	Time
RIV	Van Baelen et al. [1991]	Isotropic[b]	No	G/L[c]	Frequency
FSA	Briggs and Vincent [1992]	Anisotropic	Yes	G/L[c]	Frequency
RIH	Holloway et al. [1997a]	Isotropic[b]	Yes	G/L[c]	Frequency
PSS	Kudeki and Woodman [1990]	Isotropic[b]	Yes	None	Frequency

[a] Type of scattering in the horizontal plane
[b] or Anisotropic with an axis aligned with the velocity vector
[c] Gaussian/Linear for amplitude/phase

pointed on-axis ($\approx -1.46^\circ$ from vertical along the the y-axis, i.e. toward the SW) with an $\approx 8.2^\circ$ one-way HPBW. We did not use the entire Jicamarca antenna for transmission, since this would not have been efficient for the SA measurements (e.g. Røyrvik [1983]). The outputs from each of the antennas used in our study were independently received, sampled, and recorded. Ground clutter effects were reduced separately in both the real and imaginary signal channels. To do this, we calculated the mean complex voltages in each of the blocks used for the incoherent averaging. We then fitted a second degree polynomial to the real and imaginary mean values. Ground clutter effects were removed by subtracting this function from the voltages to provide time series for subsequent analysis.

We obtained a multi-day data set during two different periods separated by about two months. An 8-day run was taken in January, 97 (from January 20, 09:05 LT to January 27, 10:30 LT) and a 5-day run was taken in March, 1997 (from March 25, 16:50 LT to March 29, 22:15 LT). The operational parameters for each data set are presented in Table 4.2.

Figure 4.1. Antenna setup for the SA experiment at Jicamarca. The transmitting antenna is the D module, pointing vertically; and the receiving antennas are A,B and C modules. Notice that neither of the antenna axe, (x, y), are aligned with the geographic coordinates (E, N). Moreover, the antenna surface is not exactly horizontal, but is tilted $\approx 1.46^{\circ}$, approximately towards the Southwest.

Independent measurements were obtained every ≈ 3 minutes during these periods for all heights between 3 km and 21 km, for each antenna/receiver set. This combined data set was used to analyze all of the techniques studied, excepting the TDI technique. For the TDI analysis, we broke the time series used above into 4 separate sets. Each set consisted of 64/32 points in the quiet/active period (see Table 4.2). Each TDI velocity estimate was obtained solving a set of eight AOA/v_r measurements (see Equation 4.9). Thus, TDI velocity profiles were obtained $\approx$ every 6 minutes.

A calibration procedure was performed before and after each data set to determine the phase differences between the receiving lines. Briefly, a common signal (an output from one of the antennas or amplified sky noise) was fed in parallel to

Table 4.2: Operating parameters for the experiments conducted at Jicamarca

Parameter	Data Set 1	Data set 2
Starting time	20-Jan-97	25-Mar-97
Ending time	27-Jan-97	29-Mar-97
Pulse repetition period	1 ms	2 ms
Number of coherent integrations	128	128
Number of incoherent integrations	6	6
Number of points	256	128
Effective sampling time	256 ms	256 ms
Height resolution	0.45 km	0.45 km
Initial height	3 km	3 km
Number of heights	40	40
Polarization	Down(x)	Up(y)
Transmitting power	100 kW	100 kW
Atmospheric Conditions	quiet	active

each of the receiving lines (cables, front-ends, amplifiers and receivers) and the data was recorded and processed with parameters similar to those in Table 4.2. Phase differences determined from this process were used in the subsequent analysis.

The center-to-center spacing of the receiving antennas were 36 m (AB), 36 m (BC) and 50 m (AC). Such spacings are reasonable for tropospheric and stratospheric studies at VHF (e.g. Larsen and Röttger [1989]).

4.4 Results

The results presented here have been subjected to two "cleaning" processes. The first process, which was essentially a "pre-cleaning", rejected data that did not satisfy the requirements of the technique used (e.g., low correlation of the maxima or intersections of the CCFs in some of the time-domain techniques or poor Gaussian/linear fitting of the magnitude/phase of the CSFs in most of the frequency-domain techniques). Also, a common criterion for all the techniques was to reject estimates with low SNR (< -6 dB). A second "post-cleaning" was performed at the output stages of each technique to eliminate outliers. Data lying outside the range $\bar{x} \pm 2\sigma$ were rejected, where $\bar{x}$ was a 30-minute smooth estimate (including outliers)

and σ^2 was the variance of the data set $x - \bar{x}$.

In order to quantify the agreement of the different SA techniques, we adopted a "reference profile". This profile, which facilitated our intercomparisons, was chosen somewhat arbitrarily. We elected to use the FCAM "true" velocity (here: FCAMt) as our reference. The FCAMt technique had less failure points than the other techniques, following each of the two cleaning stages and exhibited a greater consistency in the measurements. In addition, this technique is one of the most widely used SA techniques (Franke et al. [1990]; Sürücü et al. [1992]; Thorsen et al. [1997]) for wind estimation.

We have divided our comparisons into two periods: a "quiet" period, with low tropospheric wind velocities ($\leq$ 10 m s^{-1}), and an "active" period where winds were much stronger. These comparisons are described separately in the following paragraphs.

4.4.1 Quiet period results

The quiet period corresponds to the 8-day data set taken in January, 1997. Results showing the mean horizontal velocity profiles (magnitude and direction), and relative magnitude differences obtained using twelve different techniques, along with the mean signal-to-noise ratio (SNR) profile) are plotted in Figure 4.2. Each of the separate techniques is indicated by separate symbols, as shown in the figure caption.

Examination of Figure 4.2 shows that the magnitudes of the observed winds are typically $<$ 15 m s^{-1} and increase slightly with increasing altitude. All techniques show a good agreement on the direction of the horizontal wind, with a mean westward wind for the observable regions between $\approx$ 8.5-21 km, and a mean south-westward wind for the region below $\approx$ 8.5 km.

The relative magnitude difference between techniques, Δ, is defined as

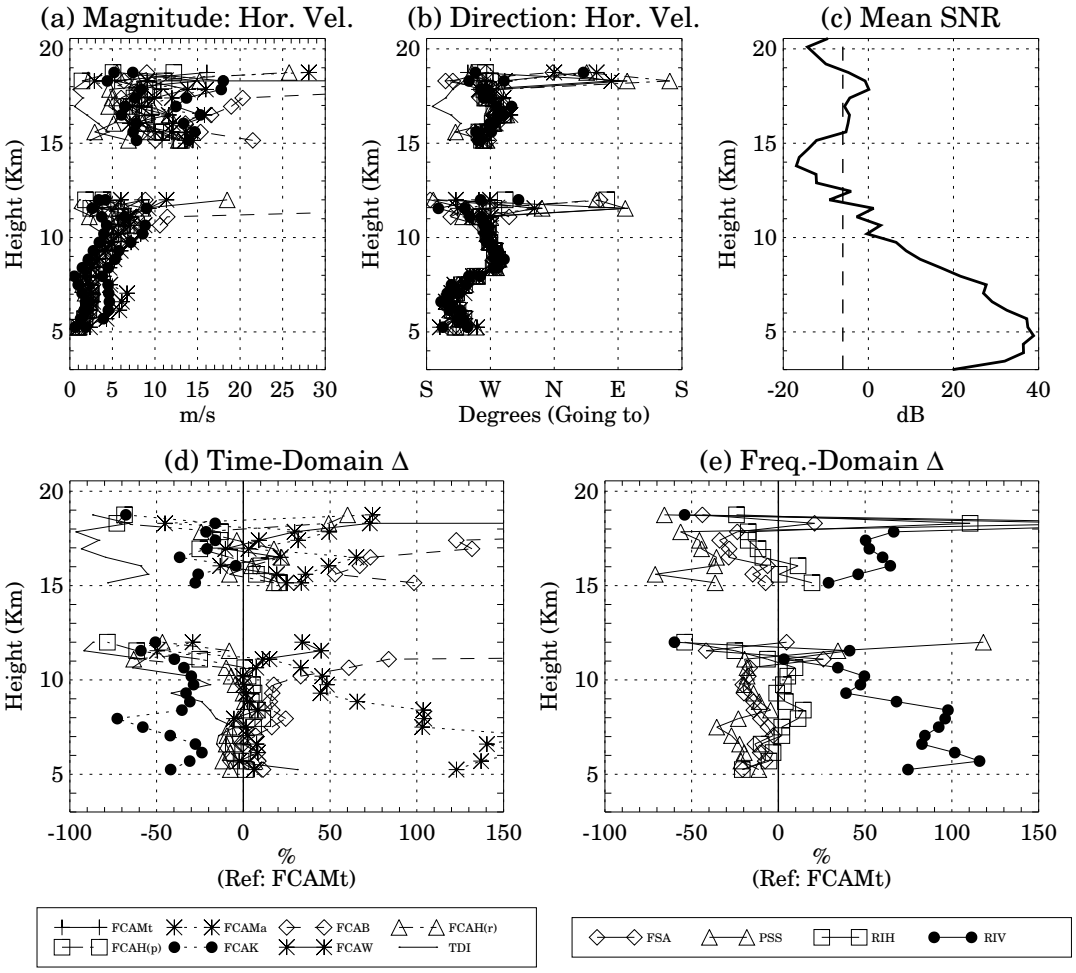

Figure 4.2. Mean horizontal velocity profiles from all techniques for the quiet period (20-Jan-97 to 27-Jan-97). (a) Magnitude, (b) Direction and (c) Mean SNR profile (the vertical dashed line represents the SNR threshold used to reject data). Relative magnitude difference in percent (Δ) for (d) time-domain techniques and (e) frequency-domain techniques at the bottom. See Section 4.2 for description of the different techniques.

$(\sqrt{u_i^2 + v_i^2}/\sqrt{u_r^2 + v_r^2} - 1)$, where (u_i, v_i) and (u_r, v_r) represent respectively the zonal and meridional components of the ith technique and the reference technique r (i.e., FCAMt). This relative difference, shown in Figure 4.2 (d)-(e), shows that the overestimated measurements are clearly coming from the "apparent" velocities (FCAMa, RIV), while the underestimated velocities are, primarily, from some frequency domain techniques dealing with turbulence (FSA, PSS) as well as the FCAK and TDI techniques. The FCAW, FCAH(r) and FCAH(p) appear to correspond most closely to the reference. Note that, for all of the techniques shown, the biases (Δ) appear to increase with decreasing SNR.

We have generated a series of statistical velocity intercomparisons using correlation coefficients (ρ_d), mean differences (μ_d), standard deviation of the differences (σ_d) and percent of failures (α), again using the FCAMt as a reference velocity. These parameters were obtained from scatter plots and histograms similar to the single example presented in Figure 4.3. In this figure, we have compared 3-minute zonal velocity FSA estimates to our reference (FCAMt) for both high SNR heights (5-10 km) and low SNR heights (16-18 km). At high SNR heights (Figure 4.3 (a)-(b)) this comparison shows a high correlation coefficient ($\rho_d \approx 0.85$), a close-to-zero μ_d (= 0.343 m s^{-1} and represented by the vertical dashed line in the histogram), and a relatively small σ_d (1.78 m s^{-1}) between these two techniques. However, at low SNR heights (Figure 4.3 (c)-(d)) the comparison gets worse (a lower ρ_d, larger μ_d and larger σ_d). In addition, the FSA measurements show a clear underestimation (Figure 4.3-(c)) and a noisier histogram (Figure 4.3 (d)). The latter result is clearly due to the small number of valid measurements at heights of low SNR.

We have obtained comparable statistical results for all the techniques for both zonal and meridional hourly wind velocities. These results are summarized for the zonal wind velocity during the quiet period for three height ranges in Figure 4.4. Similar results for the meridional wind velocity under quiet conditions are plotted in

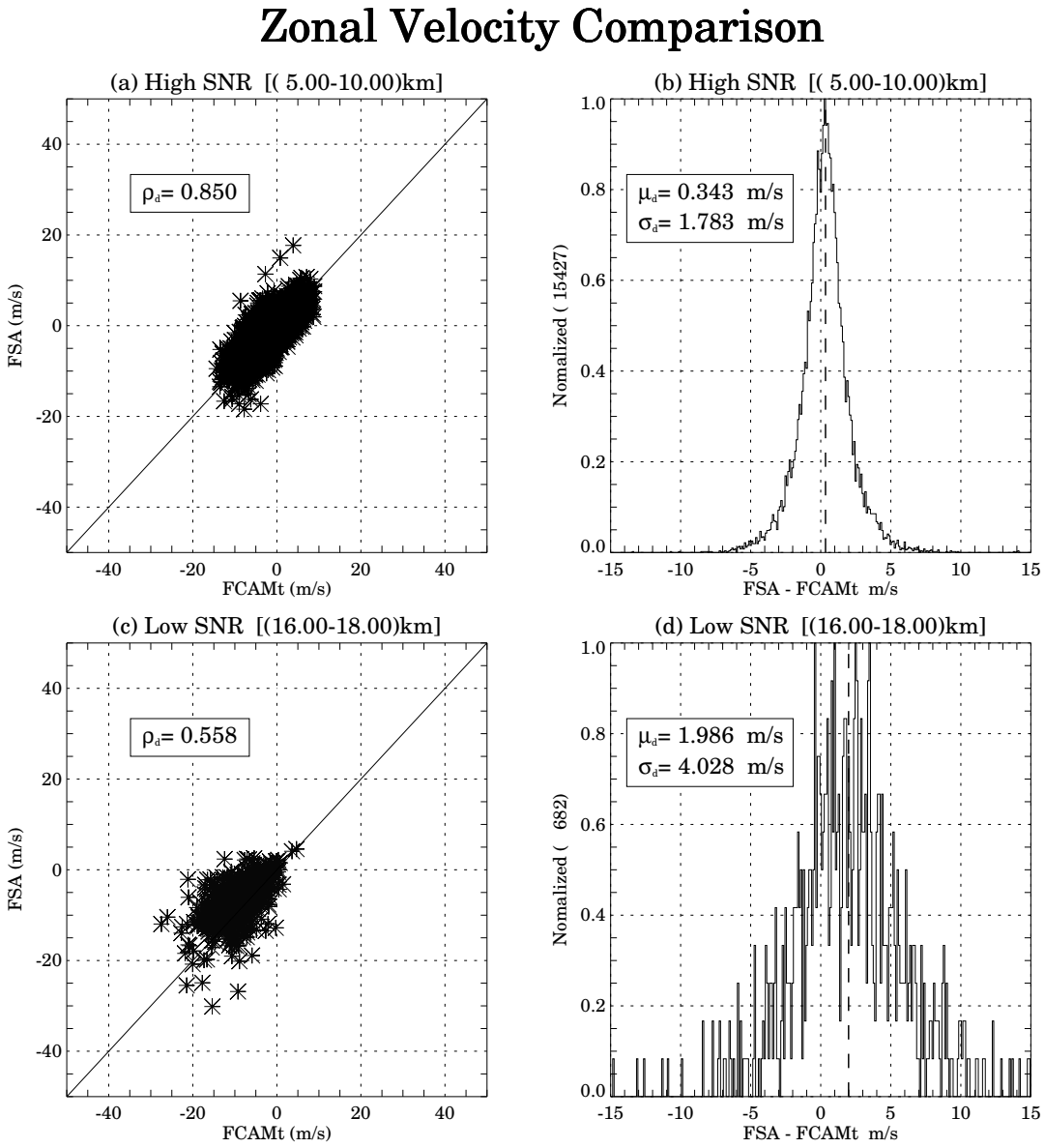

Figure 4.3. Examples of correlation and histogram comparisons of 3-minute zonal velocities obtained by the FCAMt and the FSA SA techniques during the quiet period. (a) and (b) High SNR (5-10 km), and (c) and (d) Low SNR (16-18 km) comparisons. ρ_d represents the correlation coefficient. μ_d the mean and σ_d the standard deviation of the velocity differences (FCAMt - FSA).

Figure 4.5. The techniques being compared to the FCAMt reference are shown in the y-axis of the plots. The three altitude ranges include: (1) all the heights (3-21 km), (2) only tropospheric heights with high SNR (5-10 km), and (3) just near-tropopause heights (16-18 km) where the SNR is low (≈ 0 dB). Similar results for the meridional wind velocity under quiet conditions are plotted in Figure 4.5.

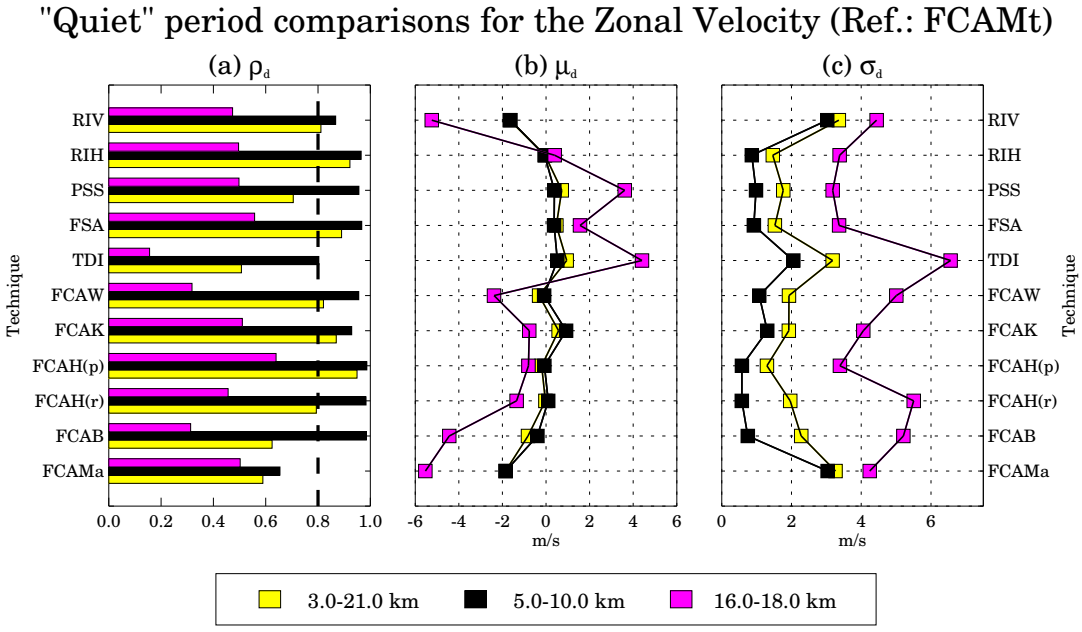

Figure 4.4. Statistical comparisons of hourly-average zonal velocity for three sets: 3-21 km (light gray), 5-10 km (black) and 16-18 km (dark gray); during the quiet period (20-Jan-97 to 27-Jan-97). (a) Correlation coefficient (ρ_d). (b) Mean (μ_d) and (c) standard deviation (σ_d) of the velocity differences.

Examination of Figures 4.4 and 4.5 shows reasonable agreement between most of the SA techniques for the 5-10 km quiet period (black squares) with some exceptions, both wind component comparisons show a high correlation ($\rho_d > 0.8$), a small mean difference ($|\mu_d| < \pm$ 1 m s^{-1}) and a small standard deviation of the differences ($\sigma_d <$ 2 m s^{-1}). The agreement gets worse in the 16-18 km range (dark gray squares), where ρ_d decreases (≤ 0.6), μ_d has more variability ($\pm$4 m s^{-1} in the zonal comparisons), and σ_d is larger ($>$ 3 m s^{-1}). This decreased agreement is consistent with the increased statistical errors as SNR decreases. Note that the

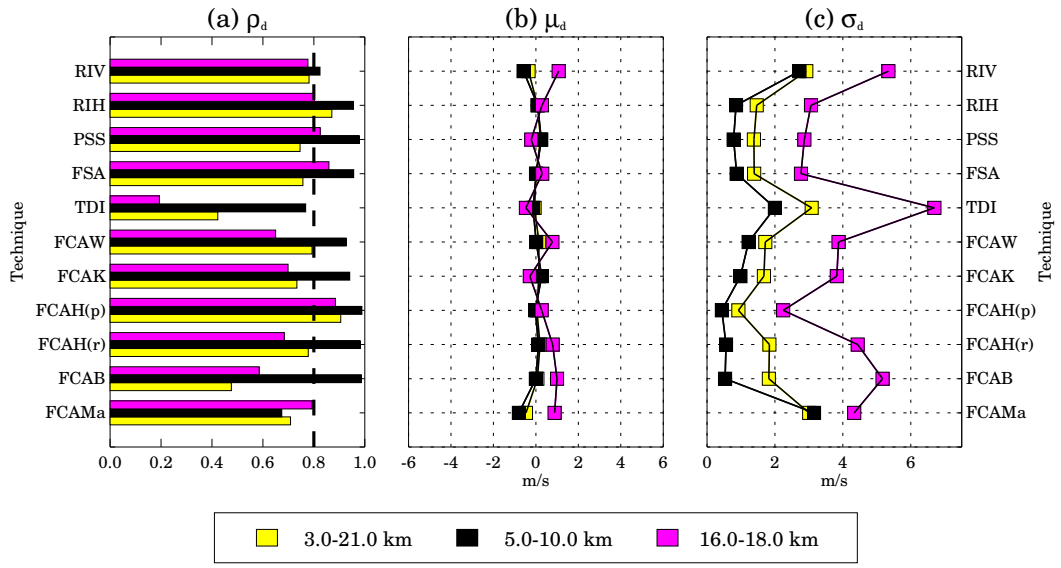

Figure 4.5. Statistical comparisons of hourly-average meridional velocity for three sets: 3-21 km (light gray), 5-10 km (black) and 16-18 km (dark gray); during the quiet period (20-Jan-97 to 27-Jan-97). (a) Correlation coefficient (ρ_d). (b) Mean (μ_d) and (c) standard deviation (σ_d) of the velocity differences.

meridional comparisons for this region are better, with smaller μ_d than the zonal comparisons. Note also that the TDI technique shows the poorest agreement with the reference (FCAMt), particularly in σ_d.

4.4.2 Active period results

The active period analysis corresponds to the 5-day data set taken in March, 1997. Figure 4.6 shows similar results to Figure 4.2 but for the active period. The magnitudes of the winds are much stronger than those in Figure 4.2. Again, all the different techniques show a good agreement in the direction of the wind, with a mean westward wind for the $\approx$ 16-18 km region, and a south-eastward mean wind at the lower heights. The relative magnitude differences, Δ, have the same features as the quiet period, except that the FCAK results are closer to the reference, particularly in the 16-18 km height range, and FCAW, FCAH(r) and FCAH(p) results show a slight overestimation that increase with increasing height. Again for all the techniques,

biases increase with decreasing SNR.

Statistical comparisons similar to those presented for the quiet period are presented next. In Figure 4.7 we present examples of scatter plots and histograms, similar to Figure 4.3, for the FCAMt and FSA comparison under the active period. Much larger velocities, somewhat higher values of ρ_d, and larger values of σ_d relative to Figure 4.3 are apparent in this figure. The higher correlation relates to smaller relative errors in velocity even though σ_d has increased. The underestimation by the near-tropopause FSA measurements, is also clear in Figure 4.7 (c). This underestimation is also seen in the positive displacement of the peak in Figure 4.7 (d). Note the skewness in this figure, which probably is due to the different degrees of underestimation at different heights (see Figure 4.6 (e)).

The zonal and meridional hourly results for this active period are shown in Figure 4.8 and Figure 4.9 respectively. Both figures have the same format as Figure 4.4. In the 5-10 km region (black squares) the high correlation persists in most of the techniques, although μ_d and σ_d have increased ($|\mu_d| < 2$ m s^{-1}, $\sigma_d \approx 2$ m s^{-1}). For the 16-18 km region (dark gray squares), the two wind components have similar ρ_d and σ_d, but μ_d is larger for the zonal component where this zonal component is greater than the meridional wind (see Figure 4.6 (a)-(b)). Again the poor intercomparison appears to lie with the TDI technique.

In Figure 4.10 we present a bar chart of 3-minute zonal velocity "failures" (α, in percent), for the three range sets used previously, during both (quiet and active) periods. The percent of failures here is defined as, the ratio of the measurements rejected over the total number of measurements, by 100. The α values represent the data rejected in the two cleaning stages mentioned earlier, i.e., in "pre-cleaning" and "post-cleaning". Figure 4.10 (a) shows the failures for the quiet period, while Figure 4.10 (b) shows failures for the active period. The lowest percent of failures occurs in the FCAMt measurements. The percent of failures in the 5-10 km region, for all

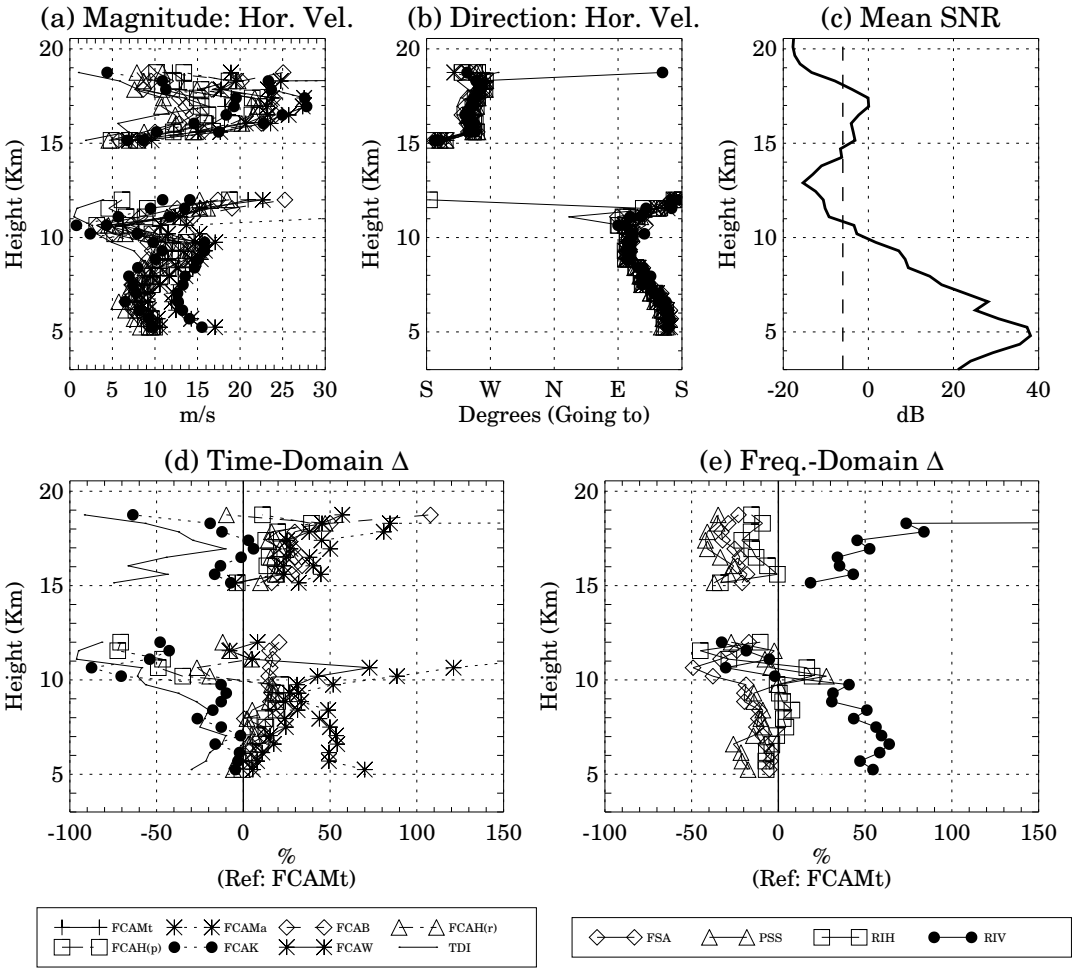

Figure 4.6. Mean horizontal velocity profiles from all techniques for the active period (25-Mar-97 to 29-Mar-97). (a) Magnitude, (b) Direction and (c) Mean SNR profile (the vertical dashed line represents the SNR threshold used to reject data). Relative magnitude difference in percent (Δ) for (d) time-domain techniques and (e) frequency-domain techniques at the bottom. See Section 4.2 for description of the different techniques.

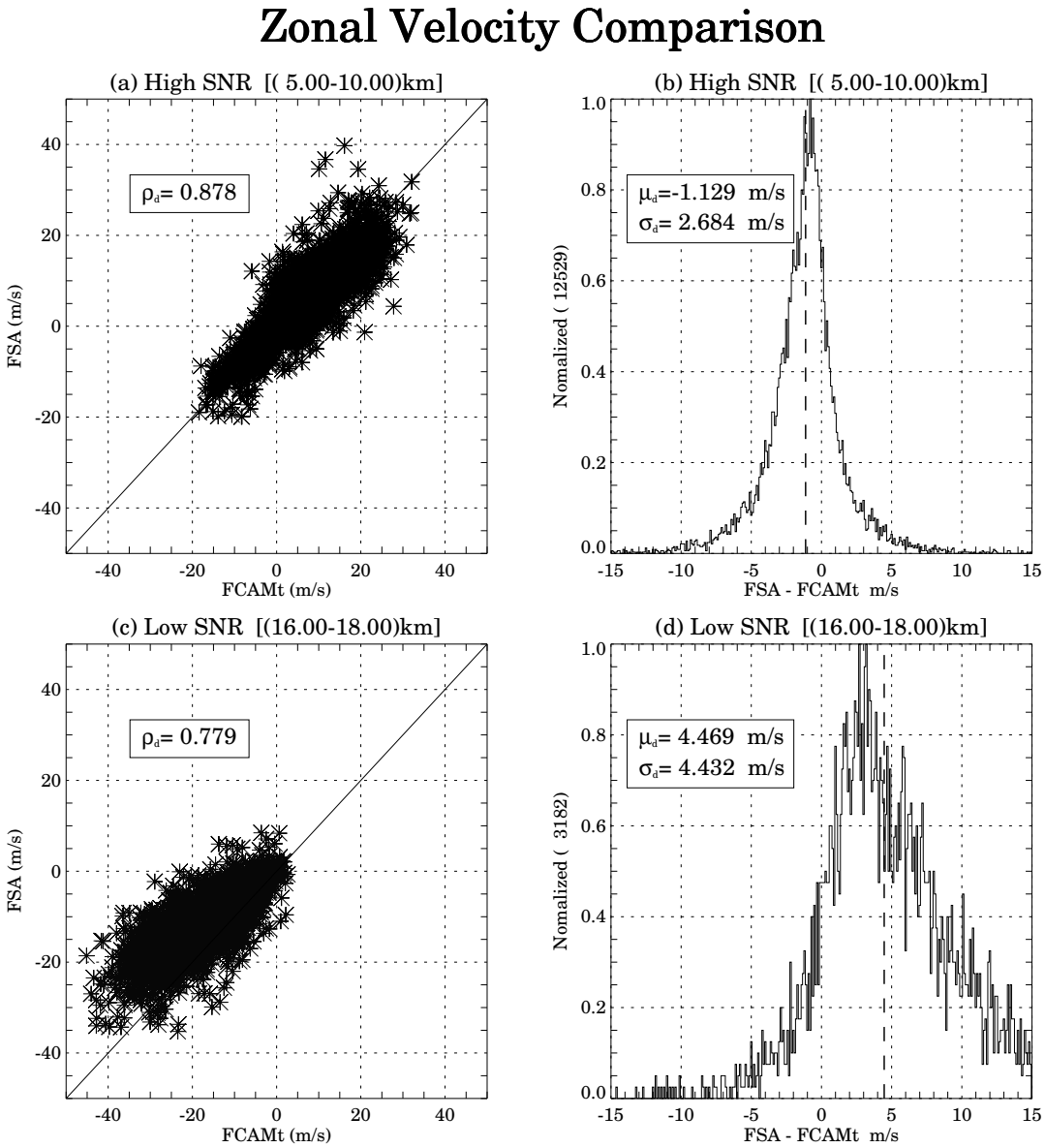

Figure 4.7. Examples of correlation and histogram comparisons of 3-minute zonal velocities obtained by the FCAMt and the FSA SA techniques during the active period. (a) and (b) High SNR (5-10 km), and (c) and (d) Low SNR (16-18 km) comparisons. ρ_d represents the correlation coefficient. μ_d the mean and σ_d the standard deviation of the velocity differences (FCAMt - FSA).

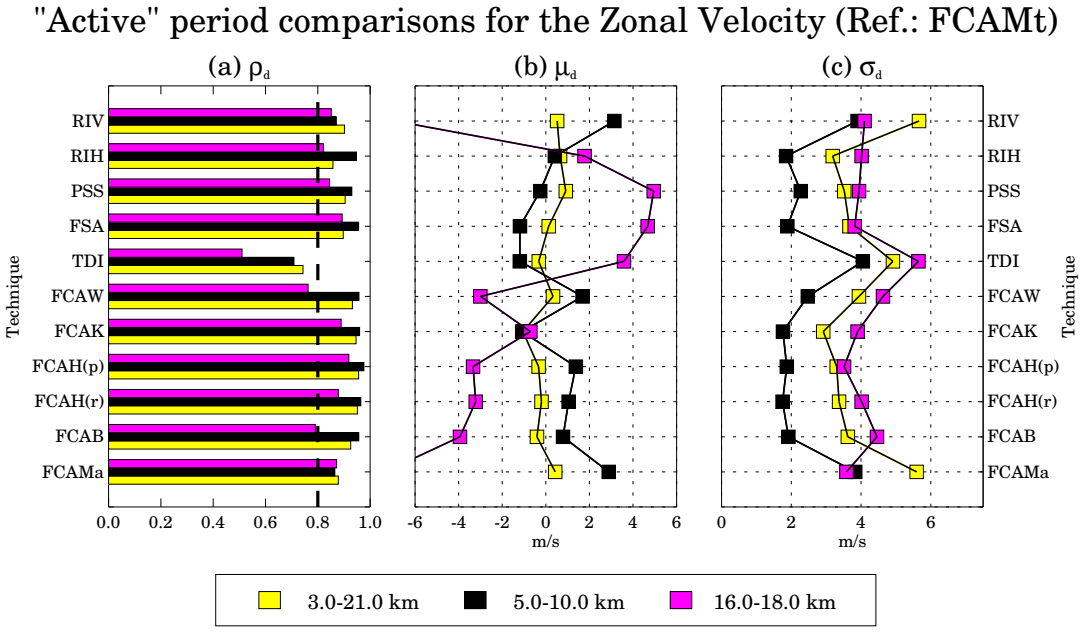

Figure 4.8. Statistical comparisons of hourly-average zonal velocity for three sets: 3-21 km (light gray), 5-10 km (black) and 16-18 km (dark gray); during the active period (20-Jan-97 to 27-Jan-97). (a) Correlation coefficient (ρ_d). (b) Mean (μ_d) and (c) standard deviation (σ_d) of the velocity differences.

the comparisons, is consistent for the quiet and active periods. The highest α is seen to occur for FCAW technique. In general the near-tropopause measurements show the highest values of α, as expected with low SNR, with the highest values occurring during the quiet period. This difference could be associated to radar sensitivity differences during the two periods. Most of the "failures" arise in "pre-cleaning". For example, for the 5-10 km region the "pre-cleaning" represents a 16% rejection rate, and the "post-cleaning" the other 6% for the FCAMt failures. Note that TDI results are not presented here due to the different effective sampling time used with this technique.

4.5 Discussion

On the basis of the above comparisons, we found an excellent agreement between the mean wind direction of wind obtained by all of the techniques. The

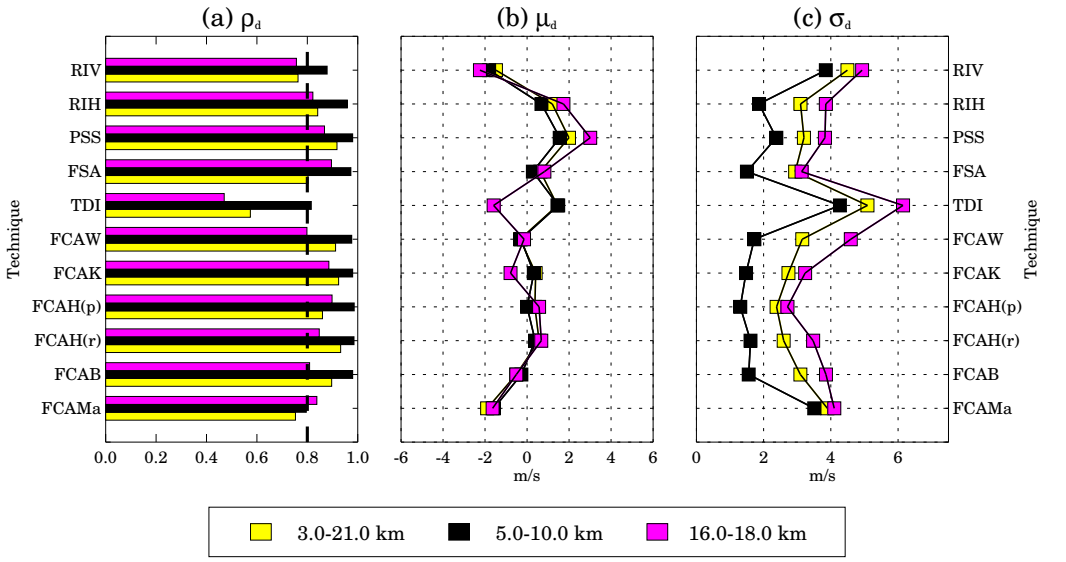

Figure 4.9. Statistical comparisons of hourly-average meridional velocity for three sets: 3-21 km (light gray), 5-10 km (black) and 16-18 km (dark gray); during the active period (20-Jan-97 to 27-Jan-97). (a) Correlation coefficient (ρ_d). (b) Mean (μ_d) and (c) standard deviation (σ_d) of the velocity differences.

major discrepancies occur primarily in the wind magnitude. In this section we discuss the degree of agreement of the different techniques and outline possible causes of these discrepancies.

In Section 4.2, we have seen the close relationship between the FCAB and the FCAMt (our reference). Because of this we would expect an excellent agreement in the two techniques. We see this agreement in the high correlation (≈ 0.98), the close-to-zero μ_d and the small σ_d at high SNR heights. The discrepancies, especially at low SNR heights, are primarily due to the greater uncertainties on the estimation of correlation peak positions and crossings values used by the FCAB technique, while the FCAMt have smaller uncertainties with the Gaussian fitting.

The FCAK velocity comparison shows better agreement (higher correlation and less underestimation) during the active period than during the quiet period. This result implies a possible correlation between the accuracy of this technique and the

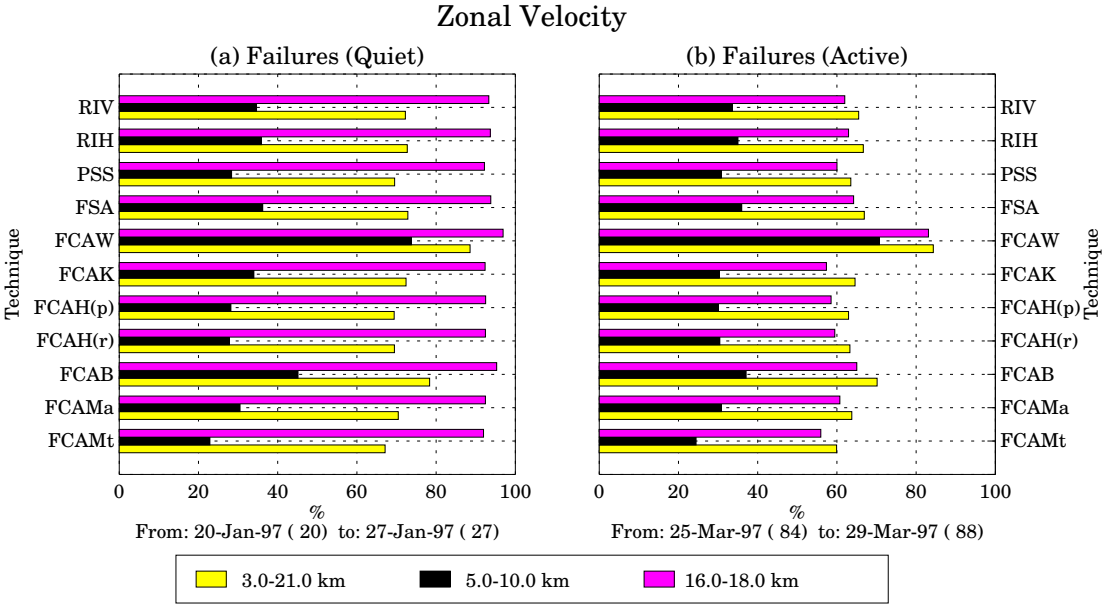

Figure 4.10. Percentage of 3-minute zonal velocity failures (α) for three sets: 3-21 km (light gray), 5-10 km (black) and 16-18 km (dark gray). (a) The quiet period, (b) The active period. This failures represents the estimates rejected in both cleaning stages: "pre-cleaning" and "post-cleaning".

inverse of the width of the ACF (i.e. the correlation time). During the active period the correlation time is shorter and the correlation samples are less correlated with each other, resulting in a better estimation of the wind magnitude.

The three time-domain techniques (FCAW, FCAH(r) and FCAH(p)) that rely on the assumption of horizontally isotropic, i.e. statistically homogeneous, scattering, show excellent agreement with the reference we have chosen (FCAMt)in the troposphere. This is the first time that these techniques have been tested at VHF, although they have been compared at UHF (Cohn et al. [1997]; Holloway et al. [1997a]). From the excellent agreement shown here these techniques are self consistent, at least for high SNR tropospheric heights.

Another way of testing the validity of the FCAH(r) and FCAH(p) measurements, is by comparing the theoretical antenna parameter, a_h, to measured β_h values obtained from Equation 4.6. For isotropic scattering, $\beta_h \approx a_h$ (see Holloway et al.

[1997a]). In Table 4.3, we show mean and standard deviation of β_h values obtained from measured values, for the FCAH(r) and FCAH(p) techniques for both quiet and active periods. These values show excellent agreement with the theoretical value of 0.040. As suggested by Cohn et al. [1997], comparisons of measured β_h values with theoretical values can be used as a "pre-cleaning" criterion.

Table 4.3. β_h results from histograms of the calculated values using Equation 4.6. The theoretical value is 0.040

Technique	Period	
	quiet	active
FCAH(r)	0.039 ± 0.008	0.038 ± 0.011
FCAH(p)	0.041 ± 0.010	0.039 ± 0.012

One advantage of using "isotropic" techniques lies with the small number of parameters required to estimate the horizontal wind. If $\beta_h = a_h$ is assumed, FCAW and FCAH(r) techniques use only two parameters to determine the wind velocity, while the FCAB technique requires four, provided that we assume a horizontally isotropic scattering (i.e., $A = B$ and $H = 0$ in Equation 4.2). Normally the FCAB technique requires six key time lags (see, e.g. Hocking et al. [1989]). Moreover, comparison between the results of FCAH(p), which relies on a Gaussian fit of the CCFs, and those from the FCAH(r), which uses "raw" CCFs, shows excellent agreement at high SNR heights. At near-tropopause heights, FCAH(p) results showed slightly better agreement with the reference than the FCAH(r) results. Therefore, reasonable and fast results could be obtained without a Gaussian fit, i.e. using FCAH(r).

Discrepancies in the FCAW are associated with the high percentage of failures (α), suggesting a poor estimation of the crossings of the CCFs. The crossing estimates depend on the size of the "window" used (e.g. 20% of total lags) and on the correlation time of the signals. An "adaptive" approach, changing the size of the window, may improve the outputs of this technique when a Gaussian form is not assumed (Recall from Section 4.2 that, if a Gaussian form is assumed the FCAW

technique is the same as the FCAH(p)).

The largest discrepancies, for all heights and all conditions, are given by the TDI technique, with lower correlations ($\rho_d \leq 0.8$), large standard deviations of the differences, and considerable underestimations. Vandepeer and Reid [1995] show good agreement with half-hour average FCAB estimates at MF and at mesospheric heights. However, in their configuration they used a wider transmitting beam (10° HPBW), sometimes tilted 10° off-vertical. This configuration includes atmospheric sampling at larger off-vertical angles with correspondingly larger AOAs and radial velocities. The contributions of random errors in the AOAs are also smaller. In our study we used a vertical beam with an $\approx 4°$ HPBW. Most of our AOA measurements were confined to less than 4°, so that random errors in the AOA measurements may be the cause of the differences we present. Other possible causes for these discrepancies, are the effects of antenna spacings and anisotropic scattering on AOA measurements (e.g. May [1993]).

Frequency domain techniques dealing with turbulence, i.e. FSA and RIH show less correlation and a slight underestimation compared with their time-domain counterparts (FCAB and FCAH respectively). Possible factors that could cause these discrepancies include:

• Spectral width estimation. From Equation 4.10 we see that an underestimation of the spectral width results in an underestimated RIH horizontal velocity. This dependence on the spectral width can also be seen by the FSA estimates. An improved spectral width estimate can be obtained by smoothing the CSFs as suggested by Sheppard et al. [1993] or by iteratively eliminating the dominant spikes of the spectra as suggested by Holdsworth [1997]. As mentioned in Section 4.2 we smoothed the spectra in our analysis. Without the smoothing, the velocity underestimation was more severe (not shown) relative to smoothing.

• Linear fitting of the phase of the CSFs. An underestimate of the phase slope of

the CSFs is usually caused by the random phases in the noisy portions of the spectra when a poor fitting is performed. This underestimation of the phase slope, as pointed out by Sheppard et al. [1993] and Holdsworth [1997], produces an overestimation of the "apparent" velocity (RIV). On the other hand, examination of Equation 4.10 suggests that an underestimation of the phase slope produces an underestimation of the RIH velocity. However, there is a good agreement between the time-domain "apparent" velocity (FCAMa) and the frequency-domain "apparent" velocity (RIV) (Figure 4.2 and Figure 4.6). Therefore the poor linear fitting does not appear to be the main source of the FSA and RIH underestimation since RIV measurements rely on the linear fitting of the phase.

• Number of incoherent averages. Incoherent averaging is one way of smoothing the CSFs. The dependence of frequency domain techniques on the number of incoherent averages has being mentioned by Franke et al. [1990] and Holdsworth [1997]. Holdsworth [1997] recommended using a sufficient number of incoherent averages to produce comparable FSA (referred as BVFSA in his paper) and FCAB results. His results show that the errors in the FSA measurements are larger than the FCAB measurements, a result similar to our results discussed in Section 4.4.

• Time and Frequency fitting regions. Sheppard et al. [1993] pointed out that some of the differences between the FCAMt and the FSA techniques may be due to the slightly different temporal scales emphasized by the two domains. FCA type of techniques, concentrate on the lower lags of the CCFs whereas frequency-domain technique (FSA type) place more emphasis on the lower frequency components of the CSFs.

The underestimation in the PSS velocities are primarily due to the off-vertical pointing direction combined with an aspect sensitivity function which biases the synthesized pointing directions. Palmer et al. [1993] also related the underestimation of PSS velocities to aspect sensitivity. However, the high ρ_d (≥ 0.95) and

small σ_d are encouraging results. The advantages of the PSS techniques are related to the advantages of the DBS method and are discussed by Sürücü et al. [1992].

The parameters needed for the majority of time-domain techniques converge to a common set of parameters if we assume a Gaussian form to the CCF magnitudes. Therefore, once the main Gaussian parameters (amplitude, delay and width) have been saved, the following techniques could be implemented: FCAB, FCAM, FCAK, FCAW, FCAH(p). It would also be possible to implement a new approach presented by Holloway et al. [1997b] that includes horizontally anisotropic scattering. Thus, in a sense, the time domain techniques form a set with varying estimators analogous to using different moment estimators with the DBS method.

A similar approach could be applied to the frequency domain techniques, provided that a Gaussian fit is applied to the magnitudes, a linear fit to the phases of the CSFs, and if the amplitude, mean Doppler, spectral width, phase slope and power are saved. Thus not only the FSA, RIV, and RIH techniques could be used, but also some other FSA approaches (e.g. Sheppard and Larsen [1992], Liu and Pan [1993]).

In both domains, when a Gaussian form is assumed, one way to check for the quality of the measurements is to intercompare the widths of the different CCFs/CSFs. In theory, all the widths should be the same as, or close to, the autocorrelation/self-spectrum width (e.g. Meek [1980]; Briggs and Vincent [1992]).

Since CCFs and CSFs are Fourier transform pairs, all the aforementioned techniques (FCAB, FCAM, FCAK, FCAH(p), FSA, RIV, RIH) could be applied provided that a Gaussian form is assumed and the fitting is done just in one domain. The question is: which domain?. One could select the time domain, where CCFs are usually smooth and monotonically decreasing, but the correlation samples are correlated with "neighbor" samples. Alternatively, one could select the frequency domain where spectral estimates are uncorrelated from each other but CSFs are

"noisier".

4.6 Conclusions

In this paper, we have compared the full correlation analysis approach by Meek [1980] (FCAMt) with other time and frequency domain SA techniques. Comparisons have been made with mean values of magnitude, direction, and magnitude difference of the horizontal winds. We have also statistically intercompared 3-minute and hourly values of zonal and meridional velocities. These intercomparisons have been made using correlation coefficients, mean differences, and standard deviation of the differences for all the techniques relative to the FCAMt reference technique. In addition, we have presented the percent of failures for each of the techniques.

Time-domain horizontal velocity measurements techniques that rely on the assumption of statistically isotropic patterns (FCAH(p), FCAH(r), FCAW) show excellent agreement with measurements using more complicated full correlation analysis techniques (FCAM, FCAB). These "isotropic" techniques could represent alternatives for situations where one needs fast measurements of the horizontal wind, particularly at tropospheric heights. Given the excellent agreement between the FCAH(r) and the FCAH(p) results, a Gaussian fit is not recommended when fast measurements are needed.

Frequency domain techniques that correct for turbulence (i.e. techniques that incorporate spectral width) exhibit larger σ_d than their time-domain counterparts. These techniques (FSA and RIH) also consistently underestimate the wind values and require a good spectral width estimation.

The assumption of a Gaussian form of the CCFs is demonstrated to be reasonable at high SNR tropospheric heights, given the excellent agreement of the reference (FCAMt) with techniques not assuming this form (i.e. FCAB and FCAW).

Other possible sources of errors, particularly for the TDI (underestimation

and larger σ_d) and PSS (underestimation), involve the effects of the antenna spacing and anisotropic scattering on AOA measurements and effective pointing positions (e.g. May [1993]). Such effects have not been considered here. They will be subjects for future studies.

The "apparent" velocities (i.e RIV, FCAMa), as expected, show a consistent overestimation ($\approx 50\%$) at all heights. At the very least, their usage is questionable. We do not recommend incorporating the "apparent" velocity measurements as one of the potential techniques for horizontal velocity determination.

In general, for all the techniques examined, there is excellent agreement in the wind direction. On the other hand, considerable discrepancies occur in the wind amplitude estimates. This problem needs further study. Depending on a number of factors, the differences in the horizontal velocity estimates can be significant. For example, errors in estimating the horizontal wind magnitude can produce errors in the correction of vertical wind measurements (e.g. Röttger and Ierkic [1985]; Larsen and Röttger [1991]; Palmer et al. [1991]; Van Baelen et al. [1991]), particularly when the horizontal wind is used in conjunction with angle-of-arrival measurements to get a "true" vertical velocity. Such biases in vertical velocities can produce a major impact in meteorological studies.

Even though the results presented here are based on an arbitrary reference velocity (we have chosen the FCAMt), the majority of the results can be implied if any other reasonable technique were to be chosen. For example, overestimation by "apparent" velocities (FCAMa, RIV), underestimation by FSA, PSS and TDI and the good agreement in the direction of the wind should all be expected.

In the results presented here, the major discrepancies occur near tropopause heights. One can attribute these discrepancies to the percent of failures presented in Figure 4.10 and to the low SNR. Alternatively, a different scattering mechanism may also contribute. In future studies, comparisons at near-tropopause heights should be

done with higher radar sensitivity in order to understand better the differences in this region.

Finally, based on the above discussions, it is impossible to select the best technique. This is due to the fact we do not know the true wind field. Our purpose here has been only to intercompare the major SA techniques that are currently used for horizontal wind measurements.

CHAPTER 5

INTERPRETATION OF ANGLE-OF-ARRIVAL (AOA) MEASUREMENTS IN THE LOWER ATMOSPHERE USING SPACED ANTENNA RADAR SYSTEMS

5.1 Introduction

Atmospheric measurements by very high frequency (VHF) radars tend to show aspect sensitivity effects, i.e., the received signal strength decreases as the beam is tilted off vertical (e.g. Green and Gage [1980]; Tsuda et al. [1986, 1997b]). Usually the aspect sensitivity function is centered at zenith. Some observations, however, show that on occasions the highest reflectivity arrives from small off-vertical locations ($< 2^{\circ}$) (Green and Gage [1980]; Röttger and Ierkic [1985]; Röttger et al. [1990a]; Tsuda et al. [1997a]). These off-vertical centers have been related to tilted scattering/reflecting structures (e.g. Röttger et al. [1990a]; Larsen and Röttger [1991]; Palmer et al. [1991]). Tsuda et al. [1997a] recently suggested that these off-vertical centers are caused by a corrugated layer that is modified following the vertical displacement caused by gravity waves.

Measurements of these off-vertical centers require systems with sufficient flexibility in beam-pointing and beam-steering capabilities, like the MU radar in Japan (see, Fukao et al. [1990]); or, alternatively, a spaced antenna (SA) system (Larsen and Röttger [1989]; Hocking et al. [1989]).

Most VHF radars currently operate in a Doppler beam swinging (DBS) mode, where the antenna beam is sequentially switched through a series of (at most five) beam positions. Because of the lack of many, closely-spaced, beam positions, measurements of off-vertical centers are not performed with these radars. SA systems, on the other hand, are able of obtaining angle-of-arrival (AOA) returns by

measuring the phase path differences between signal returns using three or more spatially separated, vertically pointing, receiving antennas (Röttger and Ierkic [1985]). These AOA measurements can be associated with off-vertical signal returns.

AOA measurements at VHF, have been used to correct vertical wind measurements by correcting for "leakage" of the horizontal wind into the vertical measurements when off-vertical returns are present (Larsen and Röttger [1991]; Palmer et al. [1991]; Van Baelen et al. [1991]). Recently, Vandepeer and Reid [1995] and Thorsen et al. [1997] have used AOAs to measure the three-dimensional wind field using medium frequency (MF) radars.

The importance of the relative positions of the transmitting and receiving antennas in AOA measurements and vertical velocity corrections, has been pointed out by May [1993]. May also suggested that these measurement should be done with SA systems using "collocated" transmitting and receiving antennas in order to unambiguously interpret the AOA in terms of tilted layers. In addition, according to May, the "leakage" of the horizontal velocity in the vertical beam can be accurately removed only if the antennas are "collocated" (i.e., receiving antennas are symmetrically placed about the transmitter).

In this paper we present the theoretical aspects of various contributions to AOA measurements using SA systems. This development will help to clarify the interpretation of AOA measurements, and their usage in vertical velocity corrections. We have expanded on the scattering model presented by Doviak et al. [1996] (hereafter Doviak et al.), to investigate AOA returns. The modifications to Doviak et al. consist of adding a tilted layer and a slightly off-verticaltransmitting (or receiving) beam, and by explicitly showing the phase terms of Doviak et al.'s original model. We then examine two different methods (time- and frequency-domain) for determining AOAs. We also analyze an expression for the statistical errors in these measurements. AOA measurements using non-collocated SA systems are discussed

in Section 5.3 in terms of vertical velocity corrections and off-vertical atmospheric returns. In Section 5.4, we compare AOA results obtained from both time- and frequency-domain methods. In Section 5.4 we also compare some of the expressions developed in Section 5.2 against experimental data. In addition, a number of interesting time series of orthogonal AOA results are shown. A summary of our results is provided in Section 5.5.

5.2 Angle-of-arrival theory for SA systems

In this section, assuming horizontally isotropic scattering, we first use the scattering theory presented by Doviak et al. to show different contributions to AOA measurements. We then present two different methods of measuring AOAs. Finally, we relate a previously published statistical error for AOA measurements (Thorsen [1996]) with Doviak et al.'s development. Expressions for the horizontal anisotropic case are derived in Appendix E and the results are related to the horizontal isotropic case in this section.

5.2.1 AOA contributions

Here we make use of the formulation derived by Doviak et al., by including some additional off-vertical contributions and by explicitly presenting the important phase terms of the complex cross-correlation functions (CCFs). As pointed out by Röttger and Ierkic [1985], AOAs are obtained from the phase differences between signal returns at receiving antennas. These phase differences can be obtained from the phase terms of the complex CCFs. The end result will be a modified expression of the phase term of the normalized CCF given in Doviak et al.'s Equation 58,

$$\phi_{ij}(\tau) = -2k_0 v_{0z}\tau \tag{5.1}$$

where ϕ_{ij} is the phase term of the CCF between receiving antennas i and j, k_0 is the radar wave number, v_{0z} is the vertical velocity and τ is a time delay. It is important

to point out that Equation 58 in Doviak et al. is valid for collocated SA systems and is a simplify version of their Equation 56.

We consider the following AOA contributions:

• Tilted layer contribution. We have represented a tilted layer effect by incorporating a tilted spatial spectrum of the refractive index field. This tilted spectrum is represented by the following Gaussian function

$$\Phi_n(\boldsymbol{K}) = \Phi_n(0) \exp\left[-\frac{\tilde{\rho}_{ch}^2 \left|\boldsymbol{K}_h - K_z\boldsymbol{\delta}_0\right|^2 + \rho_{cz}^2 \left|\boldsymbol{K}_h\right|^2 + \tilde{\rho}_{cz}^2 K_z^2}{2}\right] \tag{5.2}$$

where

$$\tilde{\rho}_{ch}^2 = \rho_{ch}^2 - \rho_{cz}^2 \tag{5.3}$$

$$\tilde{\rho}_{cz}^2 = \rho_{cz}^2 - \rho_{ch}^2 |\boldsymbol{\delta}_0|^2 \tag{5.4}$$

$$\boldsymbol{\delta}_0 = (\delta_{0x}, \delta_{0y}) \tag{5.5}$$

ρ_{ch} and ρ_{cz} are the irregularity correlation lengths in the parallel and orthogonal directions of the tilted layer, and δ_{0x} and δ_{0y} are the small off-vertical angles of the normal to the tilted plane in the x and y axes, respectively. Note that if $\boldsymbol{\delta}_0 = (0, 0)$, Equation 5.2 is equal to Doviak et al.'s Equation 28.

Using Equation 5.2 in Doviak et al.'s Equation 21 and assuming that $\Phi_n(\boldsymbol{K})$ varies slowly compared to the spectral sampling function $[F_s(\boldsymbol{K})]$ for $\boldsymbol{K}$ along K_z about the Bragg wavenumber $(2k_0)$, Equation 5.1 becomes

$$\phi_{ij}(\tau) \approx -2k_0 v_{0z}\tau - 4k_0[\boldsymbol{v}_{0h} \cdot \boldsymbol{\Omega}]\xi_h^{-2}\tau + 2k_0[\Delta\boldsymbol{\rho}_{ij} \cdot \boldsymbol{\Omega}]\xi_h^{-2} \tag{5.6}$$

where $[\,\cdot\,]$ denotes an inner product operation, $\boldsymbol{v}_{0h}$ is the horizontal vector velocity (v_{0x}, v_{0y}), and

$$\boldsymbol{\Omega} = 2\tilde{\rho}_{ch}^2 \boldsymbol{\delta}_0 \tag{5.7}$$

$$\xi_h^2 = 2a_h^{-2} + (2\rho_{ch})^2 \tag{5.8}$$

$$a_h \approx k_0 \alpha \sigma_T / z_0 \tag{5.9}$$

$$\alpha^2 = \frac{2\sigma_R^2}{\sigma_T^2 + \sigma_R^2} \tag{5.10}$$

$$\Delta\boldsymbol{\rho}_{ij} = \boldsymbol{\rho}_j - \boldsymbol{\rho}_i \tag{5.11}$$

The parameter α is a function of the difference in the sizes of the transmitting and receiving antennas, ξ_h is related to the horizontal correlation length of the diffraction pattern, a_h is an antenna parameter, z_0 represents the height range under study, $\sigma_{T/R}$ is the transmitting/receiving antenna beam width, and $\boldsymbol{\rho}_i/\boldsymbol{\rho}_j$ is the vector position of receiving antenna i/j. The term $2\boldsymbol{\Omega}\xi_h^{-2}$ is similar to the anisotropic part of Equation 6 presented by Muschinski [1996]. Moreover, this term is proportional to the antenna beam width when the antenna beam width is less than the width of $\Phi_n(\boldsymbol{K})$. The width of $\Phi_n(\boldsymbol{K})$ is $\propto 1/\rho_{ch}$ and is also proportional to the width of the aspect sensitivity function.

This off-vertical contribution could be caused by scattering/reflecting structures (Röttger et al. [1990a]; Palmer et al. [1997b]) that could be associated to Kelvin-Helmholtz instabilities (Muschinski [1996]). Larsen and Palmer [1997] showed that this type of off-vertical AOA can also be produced by gradients in the flow due to divergence.

Examining Equation 5.6, we see that if the scatter is isotropic (i.e, $\rho_{ch} \ll a_h^{-1}$ so $\xi_h^2 \approx 2a_h^{-2}$), then there is no tilted layer contribution ($\boldsymbol{\Omega} = 0$). For non-isotropic scatter, on the other hand, measurements of ξ_h^2 are needed for accurate measurements of $\boldsymbol{\delta}_0$.

• Off-vertical beams. We now add the contribution arising from an off-vertical transmitting beam by assuming that its gain function is represented by,

$$g_T^{1/2}(\boldsymbol{\rho}) = g_T^{1/2}(0) \exp\left[-\frac{|\boldsymbol{\rho} - z_0\boldsymbol{\theta}_0|^2}{4\sigma_T^2}\right] \tag{5.12}$$

where $\boldsymbol{\rho}$ represents the horizontal vector (x, y), σ_T is the transmitting antenna beam width, and $\boldsymbol{\theta}_0 = (\theta_{0x}, \theta_{0y})$ are the small off-vertical pointing angles in the x and y axes, respectively. It is important to point out that the transmitter is located at

(0,0) coordinates in the x-y plane and that this modification does not change the Fresnel zone centers. In addition, we have assumed a non-tilted spatial spectrum of the refractive index field.

Using Equation 5.12 in Doviak et al.'s Equation 10, Equation 5.1 is now modified and represented by,

$$\phi_{ij}(\tau) \approx -2k_0 v_{0z}\tau - 4k_0[\boldsymbol{v}_{0h} \cdot \boldsymbol{\Psi}]\xi_h^{-2}\tau + 2k_0[\Delta\boldsymbol{\rho}_{ij} \cdot \boldsymbol{\Psi}]\xi_h^{-2} \tag{5.13}$$

where

$$\boldsymbol{\Psi} \approx \frac{\alpha^2 \boldsymbol{\theta}_0}{2a_h^2} \tag{5.14}$$

In Equation 5.13, note the dependence on ρ_{ch} via ξ_h^2. For a horizontally isotropic atmosphere, i.e., $\xi_h^2 \approx 2a_h^{-2}$, this contribution will depend just on the pointing direction of the antennas, the antenna beam widths, and the height range.

In the case the receiving beams are pointing off-vertical, instead of the transmitting beam, $\boldsymbol{\Psi}$ is given by

$$\boldsymbol{\Psi} \approx \frac{\alpha^2 \sigma_T^2 \boldsymbol{\theta}_0}{2\sigma_R^2 a_h^2} \tag{5.15}$$

where $\boldsymbol{\theta}_0$ is the off-vertical pointing angle of the receiving antennas, and the following function was assumed for the receiving pattern

$$g_R^{1/2}(\boldsymbol{\rho}) = g_R^{1/2}(0) \exp\left[-\frac{|\boldsymbol{\rho} - (\boldsymbol{\rho}_i - z_0\boldsymbol{\theta}_0)|^2}{4\sigma_R^2}\right] \tag{5.16}$$

Off-vertical pointing beams could be due to small imperfections on vertically-directed antennas (Huaman and Balsley [1996]) or to intentional tilting of the antenna beams. For example, Vandepeer and Reid [1995] used off-vertical beam directions (10°) in their SA configuration, to obtain the wind velocity vector from AOA measurements.

• Geometrical contribution dependent on the horizontal correlation scale. For this third contribution, we have again assumed a non-tilted spatial spectrum of the refractive index field. By grouping geometrical phase terms that depends on ρ_{ch}, Equation 5.1 is modified into,

$$\phi_{ij}(\tau) \approx -2k_0 v_{0z}\tau - 4k_0[\boldsymbol{v}_{0h} \cdot \boldsymbol{\Gamma}_{ij}]\xi_h^{-2}\tau + 2k_0[\Delta\boldsymbol{\rho}_{ij} \cdot \boldsymbol{\Gamma}_{ij}]\xi_h^{-2} \tag{5.17}$$

where

$$\mathbf{\Gamma}_{ij} \approx -\frac{(\boldsymbol{\rho}_i + \boldsymbol{\rho}_j)(\alpha^2 - 1)}{4 z_0 a_h^2} \tag{5.18}$$

Examining Equation 5.18, $\mathbf{\Gamma}$ is a function of the geometry of the system, i.e., of the antenna positions and of the antennas sizes (α), and decreases with increasing height range. However, the whole contribution varies as ρ_{ch} changes (via ξ_h^2 in Equation 5.17). For example, independent of the value of ρ_{ch}, this geometric contribution becomes zero: (a) when the receiving antennas i and j are located symmetrically respect to the transmitting antenna ($\boldsymbol{\rho}_i = -\boldsymbol{\rho}_j$), or (b) when all the antennas have the same size, i.e., the same beam widths ($\alpha = 1$). Note that for an auto correlation function ($i = j$) and if $v_{0z} = 0$, $\partial\phi_{ii}(\tau)/\partial\tau$ reduces to Doviak et al.'s Equation 36.

• Geometrical contribution independent of the horizontal correlation scale. This last contribution comes from the phase terms that do not depend on ρ_{ch}. Moreover, the contribution of these phase terms, is constant for a specific system's geometry and for a specific height. Including these geometrical phase terms, Equation 5.1 becomes,

$$\phi_{ij}(\tau) \approx -2k_0 v_{0z}\tau + k_0 |\Delta\boldsymbol{\rho}_{ij}| \Lambda_{ij} \tag{5.19}$$

where,

$$\begin{aligned} \Lambda_{ij} &\approx -\frac{2(D_j - D_i)}{|\Delta\boldsymbol{\rho}_{ij}|} \\ D_i^2 &= z_0^2 + |\boldsymbol{\rho}_i/2|^2 \\ D_j^2 &= z_0^2 + |\boldsymbol{\rho}_j/2|^2 \end{aligned}$$

This geometrical contribution becomes zero in SA systems where the receiving antennas are equidistant from the transmitter ($|\boldsymbol{\rho}_i| = |\boldsymbol{\rho}_j|$), independent of ρ_{ch} or the pointing direction of the antennas.

It is important to mention that these four AOA contributions do not affect the magnitude of the normalized CCFs. In addition, the two geometric terms are present in Doviak et al.'s Equation 56, although they are not shown explicitly. Moreover, the expressions just presented are valid under the condition $|\boldsymbol{\rho}_i|, |\boldsymbol{\rho}_j| \leq \sigma_T$.

Putting together all the aforementioned contributions, the phase term of the complex CCF, $c_{ij}(\tau)$, is

$$\phi_{ij}(\tau) \approx -2k_0 v_{0z}\tau - 2k_0[\boldsymbol{v}_{0h} \cdot \boldsymbol{\Theta}_{ij}]\tau + k_0[\Delta\boldsymbol{\rho}_{ij} \cdot \boldsymbol{\Theta}_{ij}] + k_0|\Delta\boldsymbol{\rho}_{ij}|\Lambda_{ij} \tag{5.20}$$

where

$$\boldsymbol{\Theta}_{ij} = 2(\boldsymbol{\Omega} + \boldsymbol{\Psi} + \boldsymbol{\Gamma}_{ij})\xi_h^{-2} \tag{5.21}$$

so $\boldsymbol{\Theta}_{ij}$ is an AOA that includes the tilted layer contribution, the off-vertical beam direction, one geometrical contribution, and the horizontal correlation length of the scatterers (via ξ_h^2).

We have derived this phase expression assuming horizontally isotropic scattering (i.e., $\rho_{ch} = \rho_{cx} = \rho_{cy}$). It is worthwhile to note, that a similar expression can be obtained if we assume horizontally anisotropic scattering (see Equation E.4). In both scattering cases, measurements of the scattering parameters are needed to estimate most AOA contributions. The scattering parameters can be calculated from a FCA analysis (Briggs [1984]; Meek [1980]; Holloway et al. [1997b]).

The need for correction of vertical velocities for horizontal "leakage" can be seen by examining Equation 5.20. Moreover, the three-dimensional velocity vector can be obtained from this equation. This approach has been used by Vandepeer and Reid [1995] and Thorsen et al. [1997] and is called time-domain interferometry (TDI).

In this derivation, we have assumed that the phase difference among receivers lines is zero. Usually these phase differences are not zero (e.g. different cable lengths), and calibration procedures, like the one described in Section 5.4, are needed to removed them. Other calibration procedures have been described by Palmer et al. [1996]; Vandepeer and Reid [1995]; Thorsen et al. [1997]; Röttger et al. [1990a].

5.2.2 Methods of estimating AOAs

Basically there are two methods to estimate AOA returns, a time-domain and a frequency-domain method. A description of these two methods follows:

• Time-Domain method. This method was first proposed by Röttger and Ierkic [1985]. Basically, AOA measurements are obtained by measuring the phase angles of the CCFs at $\tau = 0$ for at least two antenna baselines. From Equation 5.20, the phase of baseline $i - j$ at $\tau = 0$ is,

$$\phi_{ij}(0) \approx k_0[\Delta\boldsymbol{\rho}_{ij} \cdot \boldsymbol{\Theta}_{ij}] + k_0|\Delta\boldsymbol{\rho}_{ij}|\Lambda_{ij} \tag{5.22}$$

then measuring the phase of another baseline at $\tau = 0$, knowing the positions vectors (e.g. $\boldsymbol{\rho}_1$, $\boldsymbol{\rho}_2$ and $\boldsymbol{\rho}_3$), and calculating the constant geometric terms (for instance, Λ_{12}, Λ_{13} and Λ_{23}, for a three receiver SA system), we can calculate the two dimensional AOA $\boldsymbol{\Theta}$.

• Frequency-Domain method. This method was discussed by Briggs and Vincent [1992] for the two dimensional case. Holdsworth [1997] presented an extension for the three dimensional situation. Basically, Fourier transforming Doviak et al.'s Equation 58 and including Equation 5.20, the phase of the resulting cross-spectrum function (CSF) is given by,

$$\phi_{ij}(f) = m_{ij}(f - f_{dij}) + k_0[\Delta\boldsymbol{\rho}_{ij} \cdot \boldsymbol{\Theta}_{ij}] + k_0|\Delta\boldsymbol{\rho}_{ij}|\Lambda_{ij} \tag{5.23}$$

where

$$f_{dij} = -\frac{2}{\lambda}(v_{0z} + [\boldsymbol{v}_{0h} \cdot \boldsymbol{\Theta}_{ij}]) \tag{5.24}$$

is the Doppler shift, λ is the radar's wavelength, and m_{ij} is a slope that depends on $\boldsymbol{v}_{0h}$, ξ_h^2, $\Delta\boldsymbol{\rho}_{ij}$ and the turbulence intensity (σ_t).

From Equation 5.23, the two-dimensional AOA $\boldsymbol{\Theta}$, can be obtained by evaluating the phase $\phi(f)$ at the frequencies $f = f_d$, and by calculating the geometrical terms Λ, for at least two antenna baselines.

5.2.3 Statistical errors in time-domain AOA measurements

Thorsen [1996] presented an expression for the variance of the estimate of the CCF phase ϕ, assuming the following CCF,

$$C_{ij}[\tau] = S_{ij} \exp\{-8[\pi\sigma_v T_s(\tau - \tau_{pij})/\lambda]^2\} \exp(j\omega_d \tau T_s + \varphi_{ij}) + N_{ij}\delta[\tau] \qquad (5.25)$$

where σ_v is the spectral width, T_s is the sampling time, τ_{pij} is the delay to the peak of C_{ij}, ω_d is a Doppler shift, φ_{ij} a phase difference, S_{ij} is the signal power and N_{ij} is the noise power. The phase difference φ_{ij}, and the delay to the peak τ_{pij}, are equal to zero for $i = j$. The separate receiver noises are assumed uncorrelated ($N_{ij} = 0$ for $i \neq j$).

Instead of using Equation 5.25, we have used Doviak et al.'s Equation 58 along with Equation 5.20. Then, the CCF is given by

$$C_{ij}[\tau] = S_i S_j A_{ij} \exp\left[-\frac{(\tau - \tau_{pij}/T_s)^2}{2(\tau_c/T_s)^2}\right] \exp(j\phi_{ij}[\tau]) + N_{ij}\delta[\tau] \qquad (5.26)$$

where

$$\begin{aligned} \tau_c^2 &= \frac{1}{2[2\xi_h^{-2}\,|\boldsymbol{v}_{0h}|^2 + (2k_0\sigma_t)^2]} \\ \tau_{pij}^2 &= 2\xi_h^{-2}(\boldsymbol{v}_{0h} \cdot \Delta\boldsymbol{\rho}_{ij})\tau_c^2 \\ A_{ij} &= \exp\left(-\frac{|\Delta\boldsymbol{\rho}_{ij}|^2}{2\xi_h^2} + \frac{\tau_{pij}^2}{2\tau_c^2}\right) \end{aligned}$$

Examination of Equation 5.25 and Equation 5.26 shows that they are very similar. However Equation 5.26 relates its amplitude (A_{ij}), delay to the peak and correlation time (τ_c), to the SA parameters (antenna positions, antenna beam widths, etc.) and to the atmospheric parameters (horizontal velocity, turbulence intensity and ρ_{ch}).

Using Equation 5.26 and following the derivation of Thorsen [1996], the variance of an estimated phase is,

$$E[(\delta\hat{\phi}_{ij}[\tau])^2] \approx \frac{1}{2M\mathrm{coh}_{ij}^2[\tau]} \left\{ \left(\frac{N_i^2}{S_i^2} + \frac{N_j^2}{S_j^2} + \frac{N_i^2}{S_i^2}\frac{N_j^2}{S_j^2} \right) + (1 - \mathrm{coh}_{ij}^2[\tau]) \frac{\sqrt{\pi}\tau_c}{T_s} \right\} \qquad (5.27)$$

for $i \neq j$, where

$$\mathrm{coh}_{ij}^2[\tau] = A_{ij}^2 \exp\left[-\frac{(\tau - \tau_{pij}/T_s)^2}{(\tau_c/T_s)^2}\right] \tag{5.28}$$

$\delta\hat{\phi}_{ij} = \hat{\phi}_{ij} - \phi_{ij}$, $\hat{\phi}_{ij}$ are the measured values, ϕ_{ij} represent the true values, and M represent the number of points used in the estimate. For small τ, $E[\hat{\phi}_{ij}] = E[\phi_{ij}]$ (Thorsen [1996]), therefore $E[\delta\hat{\phi}_{ij}] = 0$.

For the time-domain method, the variance of the estimated phase (statistical error), is obtained by evaluating Equation 5.28 at $\tau = 0$. At high signal-to-noise ratio ($\mathrm{SNR}_i = S_i^2/N_i^2$), this variance becomes,

$$\varepsilon_{\phi ij}^2 = E[(\delta\hat{\phi}_{ij}[0])^2] \approx \frac{1}{2M}\frac{(1 - \mathrm{coh}_{ij}^2[0])}{\mathrm{coh}_{ij}^2[0]}\frac{\sqrt{\pi}\tau_c}{T_s} \tag{5.29}$$

where $\mathrm{coh}_{ij}^2[0] = \exp[-|\Delta\boldsymbol{\rho}_{ij}|^2/(2\xi_h^2)]$. Note that this derivation is valid for horizontally isotropic scattering. In the case of horizontal anisotropy, i.e. $\rho_{cx} \neq \rho_{cy}$, Equation 5.29 remains the same. However, the coherence value $\mathrm{coh}_{ij}[0]$, is given by Equation E.9, and the new correlation time by Equation 28 in Holloway et al. [1997b]. In practice, $\mathrm{coh}_{ij}^2[0]$ is calculated after the "spike" at zero-lag, i.e., noise, has been removed from autocorrelation and cross-correlation functions (Briggs [1984]).

5.3 On the use of non-collocated SA systems for AOA measurements

In a collocated SA system, the geometrical center of the transmitting antenna coincides with the geometrical center of the array of receiving antennas. Examples of these systems are equilateral triangles and square configurations, where the transmitting antenna is located in the center of such configurations. In a non-collocated SA system such geometrical centers do not coincide. In this section, we examine some issues on the AOAs obtained by non-collocated SA systems.

Examining Equation 5.20, the only terms that contribute to the measured AOA and depend on the antenna positions are the geometrical terms $\boldsymbol{\Gamma}$ and Λ. A similar contribution has been pointed out by Vincent et al. [1987] and May [1993]

(hereafter May). Based on this contribution, May suggested that collocated transmitting and receiving antennas should be used in atmospheric AOA and corrected vertical velocity measurements. In the following paragraphs we analyze these assertions.

To begin, we examine a similar example to the one given by May. A narrow transmitting beam and wide receiving beams are assumed, implying $\alpha^2 = 2$. An isotropic scatter is represented with $\xi_h^2 \approx 2a_h^{-2}$, and a specular scatter with $\xi_h^2 \to \infty$. The positions of the receivers, with respect to the transmitter position, are $\boldsymbol{\rho}_1 = (2x_1, 0)$ and $\boldsymbol{\rho}_2 = (2x_2, 0)$. We assume zero vertical velocity ($v_{0z} = 0$), perfect vertically-directed antennas [$\boldsymbol{\theta}_0 = (0,0)$], and atmospheric contribution centered at zenith [$\boldsymbol{\delta}_0 = (0,0)$]. With these assumptions we analyze the following two effects:

• Horizontal "leakage". The "leakage" of the horizontal velocity in the radial velocity can be seen by using Equation 5.20 and evaluating the Doppler shift $d\phi_{11}(\tau)/d\tau$. The results for the isotropic and specular cases are,

$$\frac{d\phi_{11}(\tau)}{d\tau} = \begin{cases} \frac{k_0(2x_1)v_{0x}}{z_0} & \text{Isotropic} \\ 0 & \text{Specular} \end{cases} \tag{5.30}$$

which are the same to those presented by May.

• Receiver's separation. Evaluating Equation 5.20 at $\tau = 0$, the phase term $\phi_{12}(0)$ becomes

$$\phi_{12}(0) = \begin{cases} \frac{2k_0(x_1^2 - x_2^2)}{z_0} & \text{Isotropic} \\ \frac{k_0(x_1^2 - x_2^2)}{z_0} & \text{Specular} \end{cases} \tag{5.31}$$

where we have used a Taylor series expansion for D_1 and D_2. Again, these expressions are the same to those presented by May.

Evaluating the Doppler shift from

$$f_d = \left[\frac{d\phi_{11}(\tau)}{d\tau} + \frac{d\phi_{22}(\tau)}{d\tau}\right] \Big/ 2 \tag{5.32}$$

show that the leakage of the horizontal velocity can be removed using the cross-correlation phase $[\phi_{12}(0) - k_0|\Delta\boldsymbol{\rho}_{ij}|\Lambda_{ij}]$, without knowing ρ_{ch} (recall that Λ_{ij} are constant for a given height and depend just on the receiver spacing).

Based on this example we see that May's horizontal "leakage" and receiver's separation effects are related through Equation 5.17, and vertical velocity corrections are also possible using non-collocated systems.

One disadvantage of using non-collocated systems appears in some calibration procedures. In Section 5.2, we saw that a calibration procedure is needed to eliminate the phase difference among receiver lines. Some of these procedures use long-term atmospheric data, and assume that the mean off-vertical atmospheric return is zero (Röttger et al. [1990a]; Thorsen et al. [1997]). However, in the lower atmosphere, such a procedure will calibrate out the geometrical term ($\boldsymbol{\Gamma}$) that is needed for vertical velocity corrections.

Following our analysis, the unambiguous determination of the off-vertical atmospheric returns requires accurate measurements of the scattering parameters, i.e., ξ_h^2 when horizontal isotropic scattering is assumed, or ξ_x^2, ξ_y^2 and ψ (orientation) for horizontal anisotropic scattering. The latter parameters can be obtained from a FCA procedure. This requirement is true not only for non-collocated SA systems but also for those that are collocated. On the other hand, vertical velocity corrections can be done without knowing the scattering parameters under both collocated and non-collocated SA systems.

5.4 Experimental results

We have used the large VHF radar at the Jicamarca Radio observatory in Perú for our AOA studies. The Jicamarca radar operates at ≈ 50 MHz ($\lambda \approx 6m$) and has an ≈ 300 m by 300 m antenna array. The antenna is composed of 64 separate modules. Each module consists of a 12 by 12 array of cross-polarized half-wave

dipoles. In Figure 5.1, we show the antenna configuration for these experiments. For transmission, we phased four modules (section D) to point precisely vertically, with a one-way half-power beam width (HPBW) of $\approx 4°$. Antenna sections A, B and C were used for reception. Each receiving antenna was pointed on-axis ($\approx -1.46°$ from vertical along the the y-axis, i.e. toward the SW) and had a one-way HPBW of $\approx 8.2°$. The output from each of the receiving antennas was independently received, sampled, and recorded. Ground clutter effects in each receiver were reduced separately in both the real and imaginary signal channels from the recorded data. To do this, we calculated the mean complex voltages in each of the individual time blocks defined by the incoherent averaging period. We then fitted a second degree polynomial to the time-series of the real and imaginary components of these mean values. Ground clutter effects were removed by subtracting this function from the original voltages values to provide the modified time series for subsequent analysis.

We present here the results of a 5-day run taken in March, 1997 (from March 25, 16:50 LT to March 29, 22:15 LT). The operational parameters for this data set are presented in Table 5.1.

Table 5.1. Operating parameters for the experiments conducted at Jicamarca (from 25-Mar-97 to 29-Mar-97)

Parameter	Value
Pulse repetition period	2 ms
Number of coherent integrations	128
Number of incoherent integrations	6
Number of points	128
Effective sampling time	256 ms
Height resolution	0.45 km
Initial height	3 km
Number of heights	40
Transmitting power	100 kW

A calibration procedure was performed before and after the experiment to determine the possible phase differences arising from differing lengths of the receiving

Figure 5.1. Antenna setup for the Jicamarca experiment. The transmitting antenna is the vertically pointing D module; and the receiving antennas are the "on-axis" pointing A,B and C modules. The "on-axis" position differ from the zenith position because antenna surface is not exactly horizontal, but is tilted $\approx 1.46°$, approximately towards the Southwest. Notice that neither of the antenna axes, (x, y), is aligned with the geographic coordinates (E, N). The antenna centers are given in (x, y) coordinates, respect to the transmitting antenna center.

lines. Briefly, a common signal (either an output from one of the antennas or amplified sky noise) was fed in parallel to each of the receiving lines (cables, front-ends, amplifiers and receivers). This signal was recorded and processed using parameters similar to those listed in Table 5.1. Phase differences determined from this process were incorporated into the subsequent analysis.

AOA measurements were obtained every ≈ 3 minutes using both time- and frequency-domain methods (see Section 5.2.2). In both methods the measured AOA includes the four contributions described in Section 5.2.1. We have ignored estimates with very low signal-to-noise ratio (SNR < -6 dB, after coherent and incoherent integrations) in our analysis. It is important to point out that the AOAs

presented next are relative to the antenna surface and not to the horizontal plane (see Figure 5.1 for details).

We determined the time domain AOAs by fitting a line to the phase of each CCF pair (BA, BC and CA) and evaluating that line at $\tau = 0$. This process was used in order to minimize the residual contributions from noise at $\tau = 0$.

In Figure 5.2, we present histograms of AOAs obtained in this manner in the two orthogonal bases BC and BA (see Figure 5.1) for heights between 7 and 8 km. This figure shows the distributions of "raw" AOA values (solid line) and a Gaussian-fitted function (stars). Mean (μ_Θ) and standard deviation (σ_Θ) values are shown for both the "raw" (subscript r) and Gaussian-fitted (subscript g) data. Note that the results are almost the same with and without Gaussian fitting.

As mentioned above, these AOA values are relative to the antenna baseline, i.e., the true zenith position translates into $\Theta_{BC} = 0^\circ$ and $\Theta_{BA} = 1.46^\circ$.

In Figure 5.3, we present results for the frequency-domain AOAs in a format similar to Figure 5.2 for the same time period. We obtained these measurements by fitting a line to the phase of the CSFs and evaluating them at $f = f_d$, where f_d is the Doppler shift of the respective CSF (see Section 5.2.2). Examination of this figure shows the presence of more "outliers" in the frequency-domain results than using the time-domain method. The "outliers" are graphically manifested by the presence of a constant "floor" extending across the histograms, i.e., values that raise the level of the base of the Gaussian-like functions at all values of AOAs. These "outliers" are also noticed in the standard deviation values, where $\sigma_{\Theta r}$ is considerably larger than $\sigma_{\Theta g}$ for both baselines. Note that the Gaussian fitted values are similar to those obtained from the time-domain measurements.

From these similarities, we see that both methods give essentially the same information. It is important to point out that implementation is easier and calculation is faster in the time-domain. Frequency-domain methods, however, have the

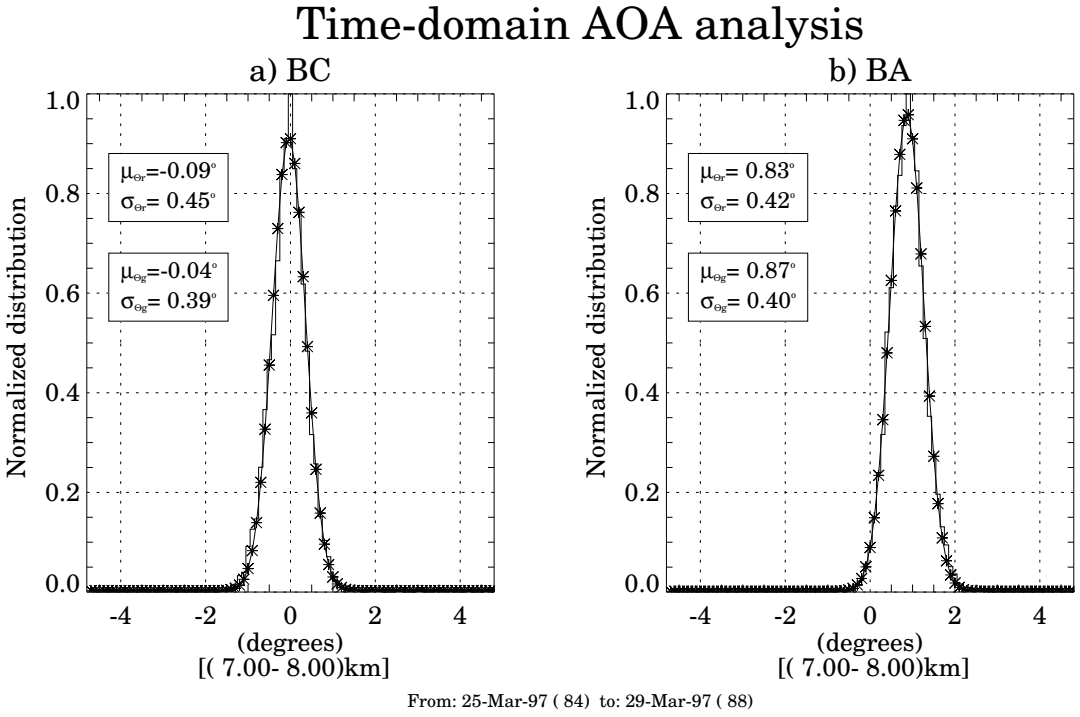

Figure 5.2. Histograms of 3-minute AOAs obtained by a time-domain method (see Section 5.2.2) using the BC (Θ_x), and BA (Θ_y) antenna pairs. Solid lines represent the actual measurements, and the fitted Gaussian functions are represented by stars. Mean (μ_Θ) and standard deviation (σ_Θ) of the AOA measurements are given for the "raw" (subscript r) and Gaussian fitted (subscript g) data. These AOA measurements are relative to the antenna plane (see Figure 5.1) and include heights between 7 and 8 km.

distinct advantage when interference is encountered. In the following analysis, we will use only AOAs obtained with the time-domain method.

We now compared results obtained using the expressions presented in Section 5.2.1 with those obtained from measured values of AOAs. The (x, y) receiver locations relative to the transmitter are $\boldsymbol{\rho}_A = (-18\text{ m}, 90\text{ m})$, $\boldsymbol{\rho}_B = (-18\text{ m}, 54\text{ m})$ and $\boldsymbol{\rho}_C = (18\text{ m}, 54\text{ m})$ (see Figure 5.1). The transmitting beam position is $\boldsymbol{\theta}_0 = (0, 1.46°)$ where $1.46°$ is the tilt of the antenna plane. The beam widths $\sigma_{T,R}$ (in meters) are related to the $\text{HPBW}_{T,R}$ (in radians) by, $\sigma_{T,R} = z_0 \text{HPBW}_{T,R}/(2\sqrt{2\ln 2})$. Using these values we have calculated the theoretical AOAs assuming an isotropic atmosphere ($\rho_{ch} \ll a_h^{-1}$). These theoretical curves are shown in Figure 5.4 for the

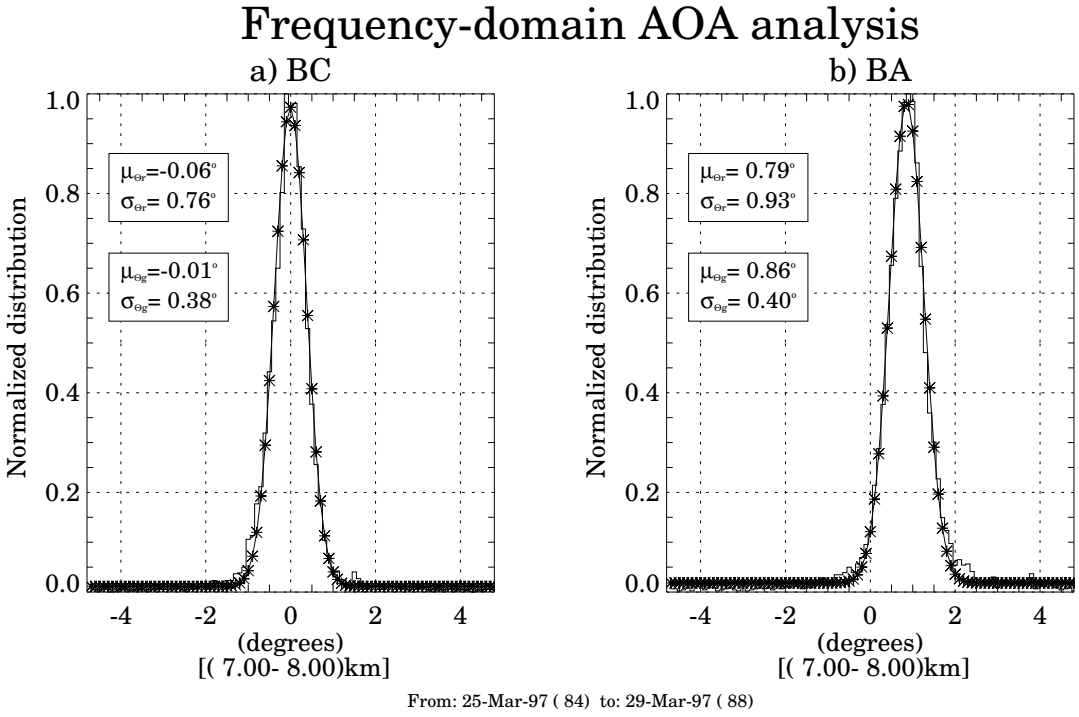

Figure 5.3. Histograms of 3-minute AOAs obtained by a frequency-domain method (see Section 5.2.2) using the BC (Θ_x), and BA (Θ_y) antenna pairs. Solid lines represent the actual measurements, and the fitted Gaussian functions are represented by stars. Mean (μ_Θ) and standard deviation (σ_Θ) of the AOA measurements are given for the "raw" (subscript r) and Gaussian fitted (subscript g) data. These AOA measurements are relative to the antenna plane (see Figure 5.1) and include heights between 7-8 km.

two orthogonal baselines. The transmitting beam contribution ($2\Psi\xi_h^{-2}$) is shown by stars, the variable geometrical contribution ($2\Gamma\xi_h^{-2}$) by pluses, the constant geometrical contribution (Λ) by diamonds, and the combined contribution $[2(\Psi+\Gamma)\xi_h^{-2}+\Lambda]$ by triangles. Notice the constant value of zero, for all contributions, in baseline BC (aligned with x). These values will be the same if the isotropic condition is not satisfy ($\xi_h^2 \neq 2a_h^{-2}$). This result is mainly due to symmetric locations (in x) of receiving antennas B and C with respect to the transmitting antenna (see Figure 5.1).

For baseline BA the combined contribution have an asymptotic behavior with height, towards the antenna pointing contribution ($2\Psi\xi_h^{-2}$). If the atmosphere is specular ($\xi_h^2 \to \infty$), extreme case, the combined contribution will be just the

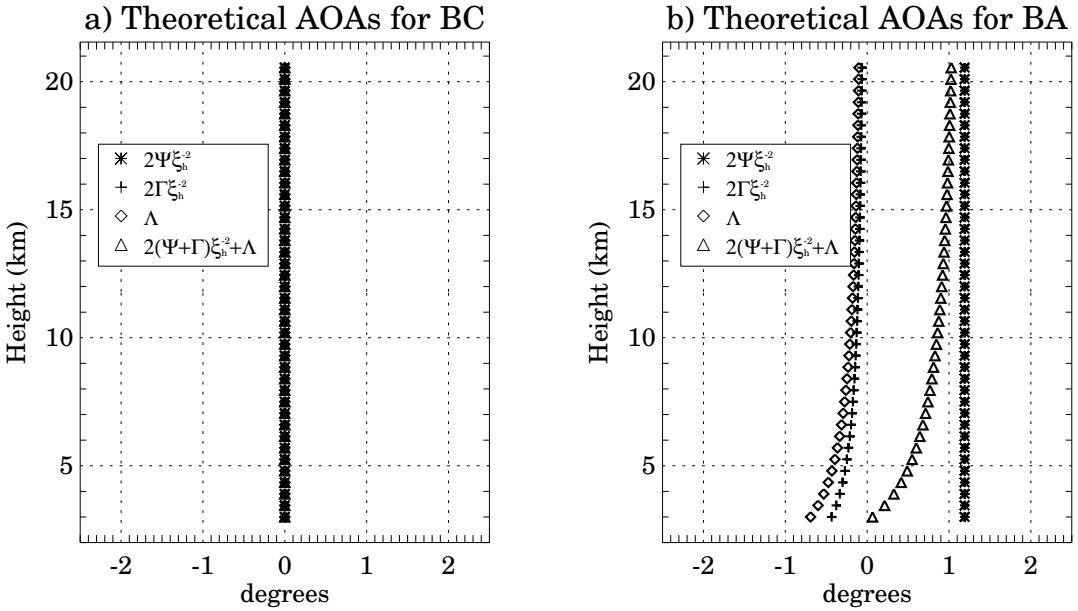

Figure 5.4. Theoretical AOAs under isotropic conditions ($\xi_h^2 \approx 2a_h^{-2}$), including just the SA system contributions. Transmitting beam contribution ($2\Psi\xi_h^{-2}$), two geometric terms ($2\Gamma\xi_h^{-2}$ and Λ), and the combined contribution $[2(\Psi+\Gamma)\xi_h^{-2}+\Lambda]$. (a) BC ($\Theta_x$), and (b) BA ($\Theta_y$).

constant geometrical term (Λ). Moreover, Λ decreases with increasing height.

In Figure 5.5, we present the 5-day AOA measurements in panels (a) and (b), for both orthogonal baselines (BC and BA), and the mean SNR profile in panel (c). The mean AOAs (triangles) are compared to the theoretical AOAs assuming isotropic conditions (thick line, $[2(\Psi+\Gamma)\xi_h^{-2}+\Lambda]$ shown in Figure 5.4). Sampled standard deviations are denoted with horizontal dashed lines. On the upper axis, we present the median value of the statistical errors of the AOAs ε_Θ (diamonds, see Equation 5.29), with values $< 0.2^\circ$ for heights with good SNR. Notice the excellent agreement between the empirical and theoretical mean values, particularly, in the lower heights ($<$ 15 km). The small differences in the near-tropopause heights ($\approx$ 17 km) could arise from non-isotropic scattering and/or "off-vertical" atmospheric returns $[\boldsymbol{\delta}_0 \neq (0,0)]$ under anisotropic scattering.

We have tried to quantify the accuracy of Equation 5.29 for the statistical

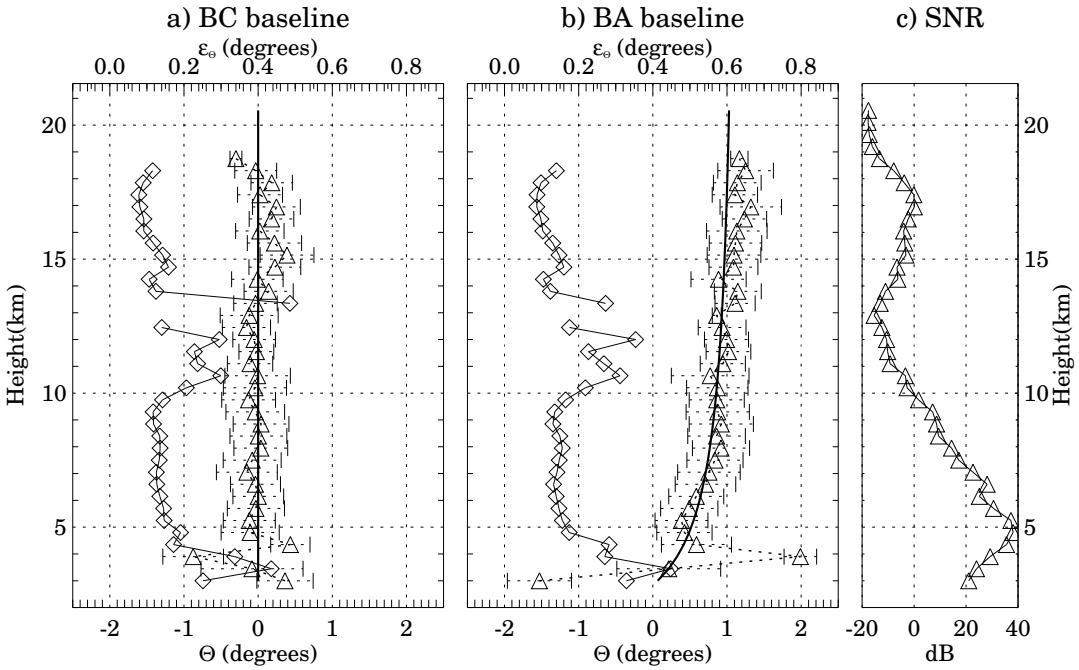

Figure 5.5. AOA profiles for the five-day data set. AOA results for (a) baseline BC (Θ_x) and (b) baseline BA (Θ_y). The mean SNR profile appears in (c). The means and standard deviations of empirical values (triangles and horizontal dotted lines, respectively), in panels (a) and (b) using the bottom scales, along with the mean theoretical value for isotropic conditions (thick solid line). Statistical errors (ε_Θ) denoted by diamonds are shown in panels (a) and (b) plotted using the top scales.

errors of AOA measurements. In Figure 5.6, we have plotted both autocorrelation values of AOAs along with AOA time series for an 8-hour interval. The 3-minute AOA values are represented by stars, and the 15-minute smoothed values by thick solid lines. The empirical statistical errors ($\hat{\varepsilon}_\Theta$) are shown by the arrows between the two horizontal lines in (a) and (c). These empirical values are obtained from the difference between the 3-minute autocorrelation values and the autocorrelation of the smoothed values at $\tau = 0$. The theoretical statistical error (ε_Θ) is obtained using Equation 5.29. Comparing these two values, we see that the theoretical value underestimates the empirical value for both baselines (in this example by $\approx 35\%$). This underestimation could be due either to the geophysical variability of the AOAs (notice the short-period oscillations in Figure 5.6 (b)-(d), with amplitudes $< 0.5°$), or

to inherent limitations involved in the approximations used in deriving Equation 5.29.

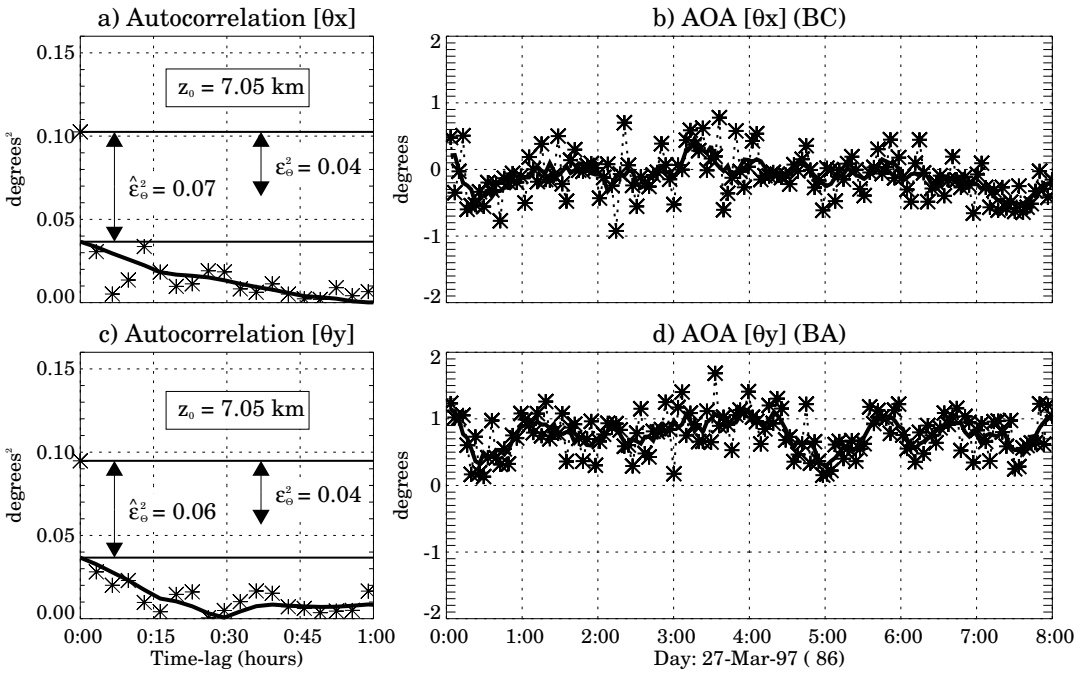

Figure 5.6. Examples of AOA autocorrelation functions ((a) and (c)) and AOA time-series ((b) and (d)) for baselines BC (Θ_x), and BA (Θ_y) respectively. AOA values for the 3-minute measurements are represented in (b) and (d) by stars. Corresponding 15-minute smoothed curves are shown by a thick continuous line. The empirical statistical variances are denoted by $\hat{\varepsilon}^2_\Theta$ (the horizontal lines in (a) and (c)), and the theoretical value by ε^2_Θ (see Equation 5.29). The empirical values are obtained from the difference between the autocorrelation of the 3-minute time-series and the autocorrelation of the smoothed time-series, at $\tau = 0$.

The theoretical and empirical statistical errors translate into CCF phase errors of $\varepsilon_\phi = 7.5°$ and $\hat{\varepsilon}_\phi \approx 9.6°$, respectively. The empirical values are closer to the model results presented by Hocking et al. [1989] (between 8° and 11° for similar coherence and time correlation values). This result, along with the fact that both statistical errors decrease in the same proportion if we use a larger number of points ($M > 768$ in Equation 5.29), results not presented here, suggest that underestimation errors indeed arise from limitations in Equation 5.29. It is possible that a constant of proportionality could be obtained from model simulations like those presented by

May [1988].

In Figure 5.7 we show histograms of correlation times τ_c (panel (a)), obtained from the width of the average auto-correlation function. The coherence values, coh_{BC} and coh_{BA}, for the two orthogonal baselines are shown in panels (b) and (c). The mean values in all panels are represented by dashed vertical lines, and theoretical values under isotropic conditions represented by solid vertical lines. Any difference between these two values are presumably due to anisotropic scattering, i.e., $\xi_h^2 \neq 2a_h^{-2}$.

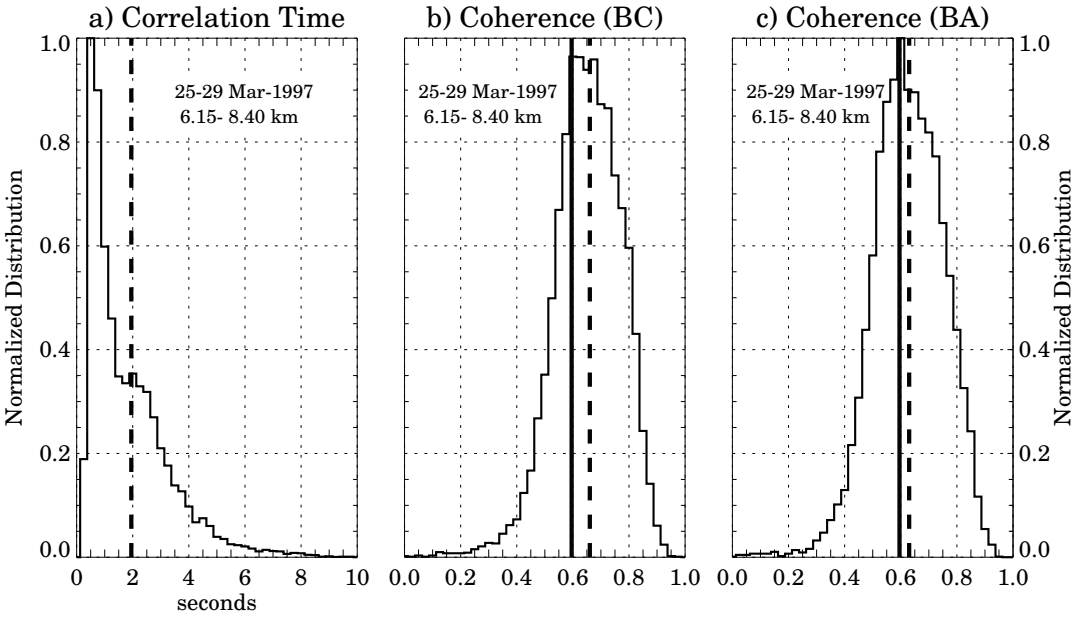

Figure 5.7. Histograms of (a) correlation times (τ_c), and coherence for baselines (b) BC ($\mathrm{coh}_{BC}[0]$) and (c) BA ($\mathrm{coh}_{BA}[0]$). The mean values in all panels are represented with vertical dashed lines, and the theoretical values under isotropic conditions ($\xi_h^2 \approx 2a_h^{-2}$), panels (b) and (c), by vertical solid lines. The anlysis is done for heights between 6.15 to 8.40 km.

In Figure 5.8, we show an $\approx$ 3-day data set of 3-minute AOAs for six separate heights. The theoretical "isotropic" mean values for both baselines, BC and BA, are represented by long dashed horizontal lines. Short dashed lines (in (b)) show the zero values at each height (recall the nonzero value of the BA AOAs, due to the geometry and antenna pointing). Examination of Figure 5.8, we see

the presence of long-period wave-like oscillations (> 12 hours) with amplitudes of $\approx 1^\circ$ (with respect to the theoretical mean values). These oscillations, which exhibit some coherency with height, are related clearly to geophysical causes. Röttger et al. [1990a] also related the AOA periodicities to long-period waves, with amplitudes of 1°-2°. Palmer et al. [1997b] and Tsuda et al. [1997a] have both observed wave-like structure in the azimuth scans of echo power, and relate them to gravity waves effects. These type of AOA oscillations have also been seen in the mesosphere by Meek and Manson [1992], using and MF radar and attributed by them to gravity waves.

5.5 Conclusions

Based on scattering theory, we have identified four separate contributions to AOA lower-atmospheric VHF radar measurements. Specifically, we can isolate contributions from: (a) tilted layers, (b) antenna pointing, and (c) two additional geometrical contributions. We have also shown that the estimation of most AOA contributions requires the measurement of the scattering parameters, under both horizontally isotropic and horizontally anisotropic scattering.

Based upon our theoretical derivation, it appears possible to relate AOA measurements to vertical wind velocities (see Equation 5.20). The correction of vertical velocities can be done without explicitly determining most AOA contributions (e.g. the tilt of reflecting structures).

Measurements of AOAs by non-collocated SA systems have been analyzed and discussed. We have shown that, in theory, vertical velocity corrections can be done with such SA systems. The unambiguous determination of the tilt of reflecting structures depend on the precision of: (a) the SA system (e.g. beam pointing, antenna positions) and (b) the measurement of scattering parameters. Nonetheless, this is also the case for collocated SA systems. The experimental corrections of

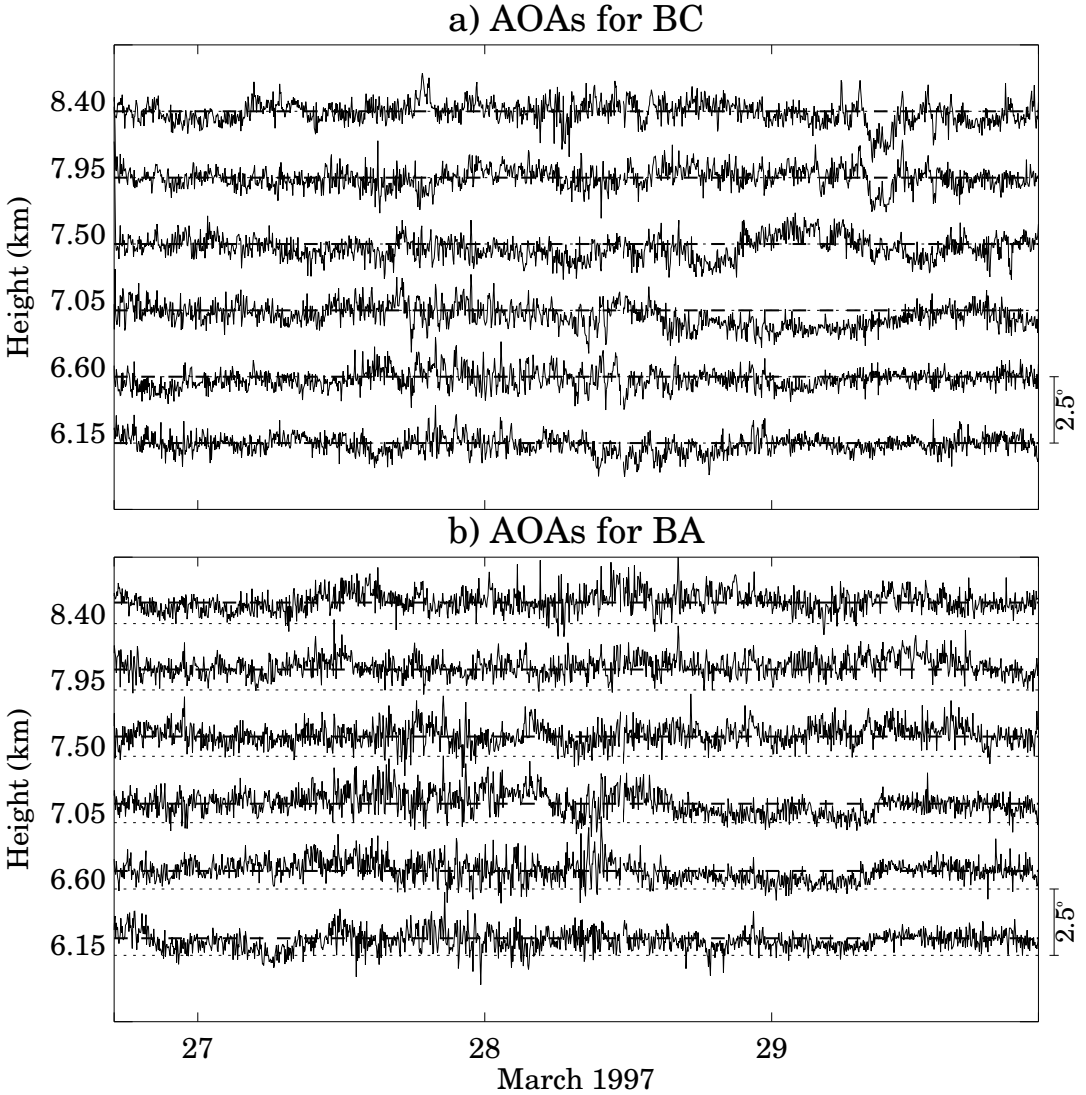

Figure 5.8. Time series of 3-minute AOAs for six tropospheric heights (6.15 to 8.40 km). Results for baseline (a) BC (Θ_x), and (b) BA (Θ_y). Mean theoretical values under isotropic conditions ($\xi_h^2 \approx 2a_h^{-2}$) represented by long dashed lines. The short-dashed lines in panel (b) represent the zero values at each height. Notice the long-period oscillations (> 12 hours).

vertical velocities are currently under study and will be presented in a future work.

We have compared frequency-domain AOA estimates to those from the time-domain method. Both methods give essentially the same information. However, the frequency-domain AOA estimates exhibited more variance (more "outliers") in our implementation, and their accuracy depends on the precision of the Doppler frequency measurement. In addition, the time-domain method is easier to implement, faster to calculate, and more reliable, than the frequency-domain method.

The non-atmospheric AOA contributions, assuming isotropic scattering ($\rho_{ch} \ll a_h^{-1}$), compared reasonably well with the experimental results, particularly below 15 km. Small differences above 15 km are probably due to anisotropic scattering and/or tilted layers.

Given the reasonable agreement between the empirical and theoretical statistical errors discussed here, a strong geophysical component can be seen in our AOA results. This geophysical component exhibit both short- (< 1 hour) and long-period (> 12 hours) oscillations with $\approx 1^\circ$ amplitudes. The detailed characterization of these AOAs measurements and their relationship to gravity waves, vertical velocities and aspect sensitivity will be left for future work.

CHAPTER 6

A STATISTICAL COMPARISON OF VHF TECHNIQUES TO STUDY CLEAR-AIR VERTICAL VELOCITIES IN THE LOWER ATMOSPHERE USING THE JICAMARCA RADAR

6.1 Introduction

Although they are of much smaller magnitude than horizontal motions of the atmosphere, vertical atmospheric motions are very important. Wind profilers offer the unique capability of directly measuring this vertical motion. Such measurements have proven valuable, for example, in defining the character and variability of the spectrum of gravity wave and tidal motions (VanZandt et al. [1991]; Gage et al. [1992]; Liziola and Balsley [1997]). Unfortunately, vertical velocity measurements, particularly mean vertical motions, have proven to be among the most challenging and least reliable of wind profiler measurements. For example, Balsley and Riddle [1984] found a typical value of the mean vertical wind in the summer mesosphere of ≈ -0.3 m s^{-1} that differed significantly from ≈ 0.05 m s^{-1} motion required to account for the summer mesopause thermal structure (e.g. Fritts and Luo [1995]). Although similar results have been reported by others, this discrepancy is not yet understood. Similar discrepancies between expected and observed vertical velocities have been reported by Nastrom and VanZandt [1994] (unreasonably strong downward motions in the tropospheric vertical velocity measurements over Flatland, Illinois), and Fukao et al. [1991] (downward velocities in the troposphere that appear to be coupled with an upward velocity in the stratosphere, in the vicinity of a strong jet stream over Japan).

All of the vertical velocity discrepancies mentioned above were obtained

using VHF radars that employ the Doppler beam-swinging (DBS) technique. The DBS technique uses a single vertically directed beam to measure the vertical velocity. Many of the DBS measurement biases have been attributed to an off-vertical "effective" pointing direction of the vertical beam, which adds a horizontal velocity contamination, or leakage, to the vertical data.

An alternative technique that could take care of this effective pointing problem is the spaced antenna (SA) technique. The SA technique was originally developed to look at ionospheric returns (Briggs et al. [1950]). The technique uses a vertically-directed antenna for transmission and three or more horizontally spaced antennas that are typically vertically directed, for reception (Larsen and Röttger [1989]). With the SA configuration, one can measure the angle-of-arrival (AOA) of the incoming atmospheric signals by measuring the phase difference of complex signals received at different antennas. A corrected vertical velocity could be obtained (Röttger and Ierkic [1985]) by additionally measuring both horizontal and radial velocities. Horizontal velocities are usually calculated from a full correlation analysis (Briggs [1984]), while radial velocities are obtained from the Doppler shift of the incoming signals.

Using this approach, Larsen and Röttger [1991] and Palmer et al. [1991] attempted to explain some of the vertical velocity discrepancies by associating the non-zero AOAs with aspect sensitive tilted layers of refractivity. Aspect sensitivity has been shown to be important at VHF (Tsuda et al. [1986, 1997a, 1997b]) but not at UHF. However, vertical velocity comparisons of concurrent VHF and UHF measurements presented by McAfee et al. [1995] show good agreement, a result that brings into question the aspect sensitivity issue.

To explain the observed large downward vertical velocities over Flatland (Illinois), Nastrom and VanZandt [1994] proposed that the dominant cause of the "apparent" mean vertical motions arises from small changes in the refractive index

induced by gravity waves with a vertical component of propagation. Briefly, for waves with upward energy propagation, the vertical velocity and static stability are negatively correlated; therefore, in such waves, regions of downward moving air will have a higher radar reflectivity on a statistical basis and will produce apparent downward velocities. This hypothesis has been supported by the mesospheric studies of Hoppe and Fritts [1995].

Palmer et al. [1997a] and Larsen and Palmer [1997] have suggested that gradients in the wind field can also affect vertical velocity estimates, particularly in radars that have relatively large beam-widths. This effect could explain intriguing results like those presented by Fukao et al. [1991].

The theoretical studies presented by Muschinski [1996] and Palmer et al. [1997a], show that measurements done with a very narrow antenna beam should be less contaminated by both aspect sensitivity and wind-field divergence effects.

In order to better assess the problems associated with VHF radar vertical velocity measurements, we have compared a number of the above techniques using a common data set. We have used the VHF radar at Jicamarca, Perú for these measurements. The Jicamarca antenna can be configured for a number of simultaneous measurements. The beam-width using the entire antenna, moreover, provides the narrowest VHF beam of any of the atmospheric radars. Taking these facts into account, we have made vertical velocity measurements with the narrow beam and used it as our reference profile in the current vertical velocity comparison studies. This is a reasonable approach, particularly since the validation of vertical velocity measurements is strongly hampered by the lack of a standard for comparison (there is no standard measurement of vertical velocity). In addition to the reference profile, we concurrently measured vertical velocities using (a) a wide beam direct measurement, (b) a "quasi" DBS inferred measurement, and (c) four corrected vertical measurements using the "classical" SA approach (these terms will be defined in the following

sections).

A description of the various vertical velocity techniques is given in Section 6.2. Details of the Jicamarca experiment follows in Section 6.3. The results of the vertical velocity comparisons are presented in Section 6.4. Finally, a discussion and a summary of our results are provided in Section 6.5 and Section 6.6, respectively.

6.2 VHF radar techniques for vertical wind velocity measurements

In this section, we describe two of the main techniques (Zenith and spaced antenna techniques) currently used by VHF radars for measurements of the vertical wind velocity (w). Sub-groups of these techniques are divided into separate sections for convenience.

6.2.1 The Zenith technique

Zenith techniques use a single vertically-directed antenna to directly measure w. Such systems operate in a monostatic mode, i.e., the same antenna is used for transmission and reception, to directly measure w. This technique corresponds to the vertical portion of a conventional DBS method.

One of the main disadvantages of the Zenith technique lies in the accuracy of the antenna pointing direction. Small deviations from vertical can caused significant horizontal velocity contributions on the measured vertical velocities (Huaman and Balsley [1996]), particularly in the mean vertical velocity values. Pointing errors in vertically-directed antennas can be caused by systematic problems and/or atmospheric contributions. Pointing errors due to systematic problems are usually small, and ways of measuring and correcting them have been presented by Balsley et al. [1988] and Huaman and Balsley [1996]. Atmospheric contributions, on the other hand, are usually attributed to "off-vertical" centered aspect sensitivity functions (e.g. Röttger and Ierkic [1985]; Röttger et al. [1990a]; Larsen and Röttger [1991]).

Pointing errors due to these types of atmospheric contributions are expected to be proportional to the antenna beam-width (Muschinski [1996]), i.e., the narrower the beam the smaller the deviation from vertical.

In this chapter we compare two different Zenith technique measurements using: (a) a narrow beam and (b) a wide beam antenna. The two-way half-power beam-widths (HPBW) are $\approx 0.85^\circ$ and $\approx 3^\circ$ for the narrow and wide beam antennas, respectively. Hereafter, narrow beam results are denoted by Wn, and wide beam results by Ww. Both measurements were analyzed in the frequency-domain using NOAA's algorithm for spectral moment estimation described in Appendix B.

6.2.2 Spaced-antenna (SA) techniques

In contrast to the Zenith technique, SA techniques provide inferred measurements of w. SA techniques rely on radial velocities made in different pointing directions and make use of the following expression,

$$v_r \approx u \sin\Theta_u + v \sin\Theta_v + w(1 - \sin^2\Theta_u - \sin^2\Theta_v)^{1/2} \tag{6.1}$$

where v_r is the radial velocity (positive going away from the radar), Θ_u and Θ_v are the zonal and meridional beam direction angles, and where zonal, meridional and vertical wind velocities are denoted by u, v and w, respectively.

From Equation 6.1, SA techniques are subdivided into "quasi" DBS and "classical" SA techniques. These techniques are outlined separately below.

6.2.2.1 The "quasi" DBS approach

The "quasi" DBS approach requires at least three different beam positions. The three-dimensional wind vector is obtained by solving a set of at least three equations like Equation 6.1, where the radial velocities and the pointing directions are known. The main assumptions in this approach are: (a) u, v and w remain the same during the integration time and throughout the volume defined by the different

beams, and (b) the pointing directions Θ_u and Θ_v are well known.

We have implemented this approach at Jicamarca by synthesizing nine different beams through software (see Appendix D for details). This implementation is usually termed post statistics steering (PSS) and was introduced by Kudeki and Woodman [1990]. Once the beams are synthesized, the radial velocities can be calculated via NOAA's algorithm (Appendix B) used in the Zenith techniques. The beam directions are calculated considering the geometry involved, the height sampled, the antenna patterns and assuming an isotropic atmosphere. A similar approach has been used by Palmer et al. [1993], but using just three beam positions. The use of nine beams allows the possibility of averaging out the errors introduced by anisotropic scattering.

6.2.2.2 The "classical" SA approach

The "classical" SA approach uses only one beam direction (usually vertical) and multiple antennas (Röttger and Ierkic [1985]). This technique requires knowledge of the angle-of-arrivals (effective pointing directions) and the radial and horizontal velocities. The vertical velocity, also known as "corrected" vertical velocity (e.g. Larsen and Röttger [1991]), is obtained from

$$\hat{w} = v_r - (u \sin \Theta_u + v \sin \Theta_v) \tag{6.2}$$

where we are assuming small angles. The horizontal "leakage" on the radial velocity, due to "off-vertical" AOA contributions (atmospheric and systematic) can be removed to get a "corrected" w measurement ($\hat{w}$).

In the present study we have calculated the effective beam positions (Θ_u, Θ_v), also called angle-of-arrivals (AOAs), by calculating the phase differences between receiving antennas. To improve reliability, we have made these calculations in the time-domain (see Chapter 5 for details). In addition, we have also determined radial velocities (v_r) in the time-domain by measuring the phase slope at zero-lag of

the complex auto correlation functions (ACFs) (e.g. Woodman [1985]). The horizontal velocity measurements have been obtained from four different SA techniques (see Chapter 4) in order to study their effects on vertical velocity corrections. The four techniques include three separate "true" velocity estimates using full correlation analysis (FCA), and a "true" velocity estimate using a full spectral analysis (FSA). The three FCA "true" velocity estimates are obtained using techniques reported by Briggs [1984] (here: FCAB), Meek [1980] (here: FCAM), and Holloway et al. [1997a] (here: FCAH). The "corrected" w obtained by using the FSA horizontal velocity (here: FSAM), on the other hand, is a modification to the approach presented by Briggs and Vincent [1992]. We obtain the horizontal velocity from a frequency-domain analysis. The radial velocity (v_r) and the AOAs are obtained from a time-domain analysis.

Salient characteristics of the aforementioned SA techniques for horizontal wind measurements are summarized in Table 6.1. Additional details of these techniques can be found in Chapter 4, where the FCAMt and FCAH(r) there, corresponds to FCAM and FCAH in this chapter.

Table 6.1. Salient features of the SA techniques for horizontal wind measurements used in vertical wind velocity estimation.

Technique	Reference	Scattering[a]	Turbulence	Domain
FCAB	Briggs [1984]	Anisotropic	Yes	Time
FCAM	Meek [1980]	Anisotropic	Yes	Time
FCAH	Holloway et al. [1997a]	Isotropic	Yes	Time
FSAM	Briggs and Vincent [1992]	Anisotropic	Yes	Frequency

[a] Type of scattering in the horizontal plane

6.3 Experimental setup

The Jicamarca radar (near Lima, Perú) used for these studies operates at $\approx$ 50 MHz and has a 288 m by 288 m antenna array. The array is composed of 64 separate modules. Each module consists of a 12 by 12 array of cross-polarized

half-wave dipoles. Figure 6.1 shows the antenna configuration for our measurements. The vertically-pointing full array (narrow beam, E) was used for both transmission and reception in the "down" polarization (i.e., the lower set of dipoles [x aligned]). The "up" polarization (the orthogonal upper dipole set [y aligned]) was used for the vertically-pointing D antenna (wide beam) for both transmission and reception. The on-axis-directed A, B and C modules were used for reception only in the "up" polarization. Note that the on-axis pointing direction is not vertical but rather $\approx -1.46^\circ$ from vertical along the the y-axis, i.e. toward the Southwest and results from the slope of the valley floor. The characteristics of these five antennas have been summarized for convenience in Table 6.2.

Table 6.2: Antennas characteristics.

	Antennas				
	A	*B*	*C*	*D*	*E*
Area (m^2)	36x36	36x36	36x36	72x72	288x288
No. Modules	1	1	1	4	64
One-way HPBW	8.18°	8.18°	8.18°	4.05°	1.15°
Direction	On-axis	On-axis	On-axis	Vertical	Vertical
Transmission	No	No	No	Yes	Yes
Reception	Yes	Yes	Yes	Yes	Yes
Polarization	"up"	"up"	"up"	"up"	"down"

The outputs of each of the five receiving antennas were independently received, sampled, and recorded. Ground clutter effects were partially filtered separately in both the real and imaginary signal channels.

We obtained a 5-day data set in March, 1997 (from March 25, 16:50 LT to March 29, 22:15 LT) running simultaneously in the SA and Narrow-Wide beam modes. Operational parameters for this data set are presented in Table 6.3. Due to availability of only four receivers at the time of the experiment, complex signals from antennas D and E shared the same physical receiver. This process was possible using two sampling windows with an effective delay of 1 ms. After digitization, the two complex signals were recovered and recorded in independent channels (via software).

Figure 6.1. Antenna setup for the Jicamarca experiment. The full array, vertically pointing E module, was used for transmission and reception in the "Down" polarization (x-aligned). In the orthogonal polarization ("Up", y-aligned), the vertically pointing D module was used for transmission and reception. The "on-axis" pointing A,B and C modules are used only for reception. The "on-axis" position differ from the zenith position, because the antenna surface is not exactly horizontal, but is tilted $\approx 1.46°$, approximately towards the Southwest. Notice that neither of the antenna axes, (x, y), is aligned with the geographic coordinates (E, N).

Independent measurements were obtained every $\approx$ 3 minutes during this period for all heights between 3 km and 21 km for each antenna/receiver set. The resulting data set was used to analyze all of the techniques studied.

A calibration procedure was performed before and after each data set in order to determine the phase differences between the receiving lines (more details can be found in Appendix C). The ground clutter removal and calibration processes, were done in the same way described in Chapter 4.

Table 6.3. Operating parameters for the experiments conducted at Jicamarca (from 25-Mar-97 to 29-Mar-97).

Parameter	Value
Pulse repetition period	2 ms
Number of coherent integrations	128
Number of incoherent integrations	6
Number of points	128
Effective sampling time	256 ms
Height resolution	0.45 km
Initial height	3 km
Number of heights	40
Transmitting power at antenna D	100 kW
Transmitting power at antenna E	30 kW

6.4 Results

As mentioned in the Section 6.1, we adopted a "reference profile" in order to quantify the agreement of the different w measurements. We elected to use the narrow beam measurements (Wn) as our reference. These narrow beam measurements were expected to have less vertical velocity biases than those obtained using a wide beam (see Section 6.2). In addition, Wn measurements had a higher signal-to-noise ratio (SNR) owing to the large antenna area.

All of the vertical velocity measurements (both direct and inferred) were "cleaned" if the SNR was low (< -6 dB). In addition, inferred vertical velocities were edited out when either the zonal or meridional velocities were cleaned. Horizontal velocities were cleaned twice (pre-cleaning and post-cleaning) in the same manner as that described in Chapter 4.

Statistical comparisons were made over three different time periods: (1) the entire 5-day data set (All), (2) a selected 24-hour Quiet period, and (3) a selected 24-hour Active period. Additional information on these periods has been tabulated in Table 6.4.

Before presenting the results of our vertical velocity analyses, it will be useful to provide selected background results for these selected periods:

Table 6.4. Information on the periods (All, Quiet and Active) used in these analyses.

Parameter	Data set		
	All	Quiet	Active
Starting date	25-Mar-97	26-Mar-97	28-Mar-97
Starting time	17:00	16:00	22:00
Duration	5 days	24 hours	24 hours
Conditions	quiet/ active	quiet	active

• SNR profiles. SNR profiles are shown in Figure 6.2 for each period (All, Quiet and Active). A $\overline{\text{SNR}}$ profile for the SA configuration (the average SNR for antennas A, B and C) is plotted with pluses; profiles using the wide and narrow beam vertical antennas are shown by asterisks and diamonds, respectively. Clearly the largest SNR is recorded using the narrow beam antenna, particularly above 10 km. This statement is true even though the transmitted power on this antenna was ≈ 5 dB less than the transmitted power on the wide beam antenna. Below 10 km the SNR between the wide and narrow beams are more comparable. This is primarily due to the fact that this region lies in the near-field of the narrow beam antenna. Comparison of panels (b) and (c) in this figure suggests an enhancement of SNR during the active period relative to the quiet period (compare, for example, the SNRs at 7.05 km, where the active value is > 10 dB relative to the quiet value). Above 15 km, the peak $\overline{\text{SNR}}$ enhancement in the three panels suggests that the tropopause height is ≈ 17 km (Riddle et al. [1984]).

Based on these SNR profiles, hereafter we will show results only for heights with SNR > -6 dB. Also, we will exclude in our analysis heights below 5 km, where problems due to receiver recovery are known to exist.

• Turbulence intensity and correlation length. Using a full correlation analysis (FCA) we were able to obtain estimates of the turbulence intensity (σ_t) and the correlation length (ξ'). Turbulence intensity was determined from,

$$\sigma_t = \left[\frac{1}{2k_0^2}\left(\frac{1}{2\tau_c^2} + 4Av_{0x}^2 + 4Bv_{0y}^2 + 8Hv_{0x}v_{0y}\right)\right]^{1/2} \tag{6.3}$$

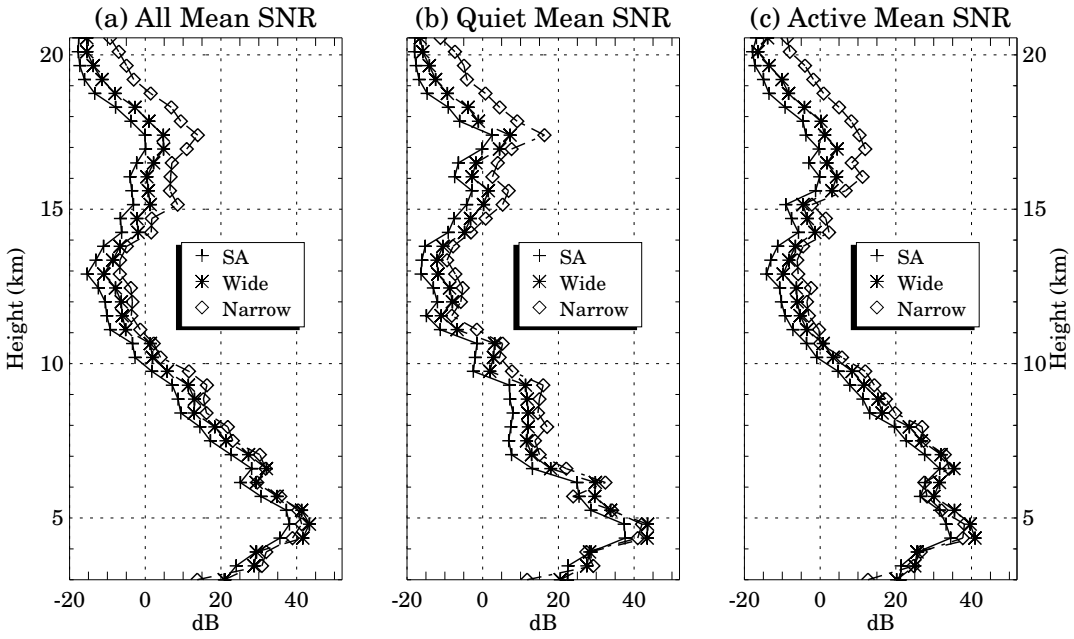

Figure 6.2. Mean SNR profiles for the following time periods: (a) All (b) Quiet and (c) Active. The SA $\overline{\mathrm{SNR}}$ profile is denoted by "+s", while the wide beam and narrow beam $\overline{\mathrm{SNR}}$ are denoted with asterisks ($*$) and diamonds ($\diamond$) respectively.

where τ_c is the correlation time, k_0 is the radar wavenumber, (A,B H) are FCA parameters, and v_{0x} and v_{0y} are the velocity projections in the x and y axes (see Holloway et al. [1997b] for more details).

The correlation length ξ' represents the average value of the major and minor axes of a horizontal aspect sensitivity function, and is equal to $(\xi'_x + \xi'_y)/2$ in Holloway et al. [1997b] and $\propto (a+b)/2$ in Meek [1980]. Thus, the bigger ξ', the more aspect sensitive the atmosphere.

Median values of these two parameters are plotted in Figure 6.3, for the three time periods. Examination of Figure 6.3 below 10 km suggests that the active period is considerably more turbulent and somewhat less aspect sensitive than the quiet period. It is also apparent that for both active and quiet periods, the region above 15 km appears to be more aspect sensitive than the lower heights.

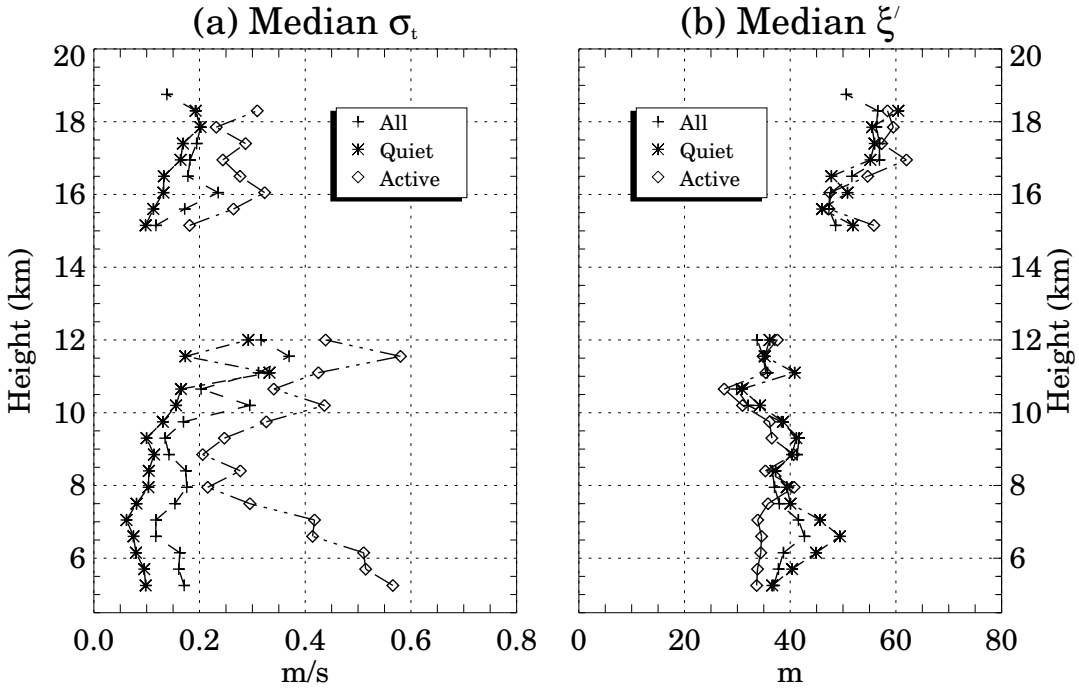

Figure 6.3. (a) Median turbulence intensity (σ_t), and (b) median correlation length (ξ'), for the time-periods: All (+), Quiet ($*$) and Active ($\diamond$).

• Horizontal wind velocity profiles. We have calculated zonal and meridional velocities from the SA configuration by applying some of the techniques used in Chapter 4. In Figure 6.4, the zonal (upper panels) and the meridional (lower panels) wind components are plotted for each of the three time periods. Examination of Figure 6.4 shows that, over all, there is a stronger meridional component during the active period, than during the quiet period. Furthermore, at near-tropopause heights (i.e., above $\approx$ 15 km), the zonal wind is westward and somewhat stronger during the active period ($u \approx -20$ m s^{-1}) than during the quiet period ($u \approx -10$ m s^{-1}).

In general the agreement among the SA techniques can be summarized as: good below 12 km and poor above 15 km. The discrepancy above 15 km is particularly obvious in the zonal component. At these heights, FCAB (with asterisks) and FCAH (with diamonds) measurements are somewhat larger than the FSAM (with triangles) and PSS (with squares) measurements. A detail discussion on the horizontal velocity

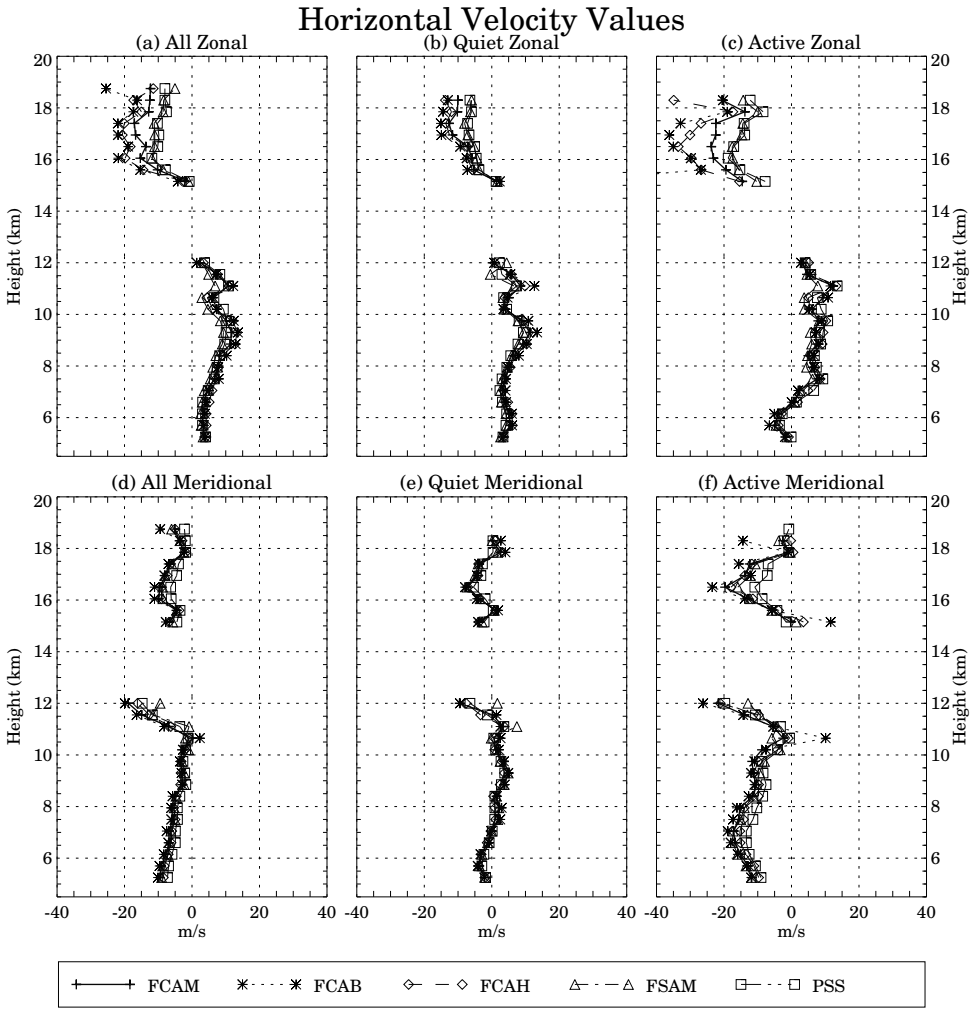

Figure 6.4. Profiles of mean zonal and meridional wind velocities (μ_u and μ_v) for the following SA techniques: the reference profile FCAM (+), FCAB ($*$), FCAH ($\diamond$), FSAM ($\triangle$), and PSS ($\square$). Each column corresponds to a particular selected time period (All: first column, Quiet: second column, and Active: third column).

agreement of these SA techniques is given in Chapter 4.

• AOA profiles. Median values (diamonds) with standard deviations (horizontal solid lines) of observed zonal and meridional AOAs are plotted in Figure 6.5. In addition, we show the AOA (solid curve) values that would be expected for scattering from an isotropic atmosphere, given the antenna geometry and pointing beam directions. Note that these theoretical values do not include the geometrical contributions that are independent of the horizontal correlation scales (Λ) discussed in Chapter 5. These geometrical contributions were removed from the AOAs plotted in Figure 6.5 and from the AOAs used in Equation 6.2 to get "corrected" vertical velocities ($\hat{w}$). AOA results show clearly that the echoes are coming from small "off-vertical" angles. This effect, on the other hand, is reasonably predictable, and clearly arises from geometric, pointing beam direction and atmospheric effects. Geometric and pointing beam direction effects alone would produce AOAs shown by the solid curve; additional atmospheric effects would produce departures from the solid curve. Note that the standard deviations in this figure can be seen to be as high as $0.6°$. Given the results shown in Figure 6.5, radial velocities measured with the SA system must be contaminated by the horizontal velocity. Clearly, a correction to these "vertical" velocities is required in order to get "true" vertical velocities. Usually, SA radial velocities are calculated by averaging the radial velocities of all the receiving antennas. This averaging process, however, will still cause biases in the "corrected" vertical velocities if a non-collocated SA system is used. These biases are caused by the geometrical contributions that depend on the horizontal correlation scales ($\mathbf{\Gamma}$) discussed in Chapter 5. Note that, in a non-collocated SA system, the geometrical center of the array of receiving antennas does not coincide with the geometrical center of the transmitting antenna. Since our SA system at Jicamarca is non-collocated, SA radial velocities (FCAr) that are used in Equation 6.2 to get $\hat{w}$ have been calculated from the average of the radial velocities of antennas A and B in order to avoid the

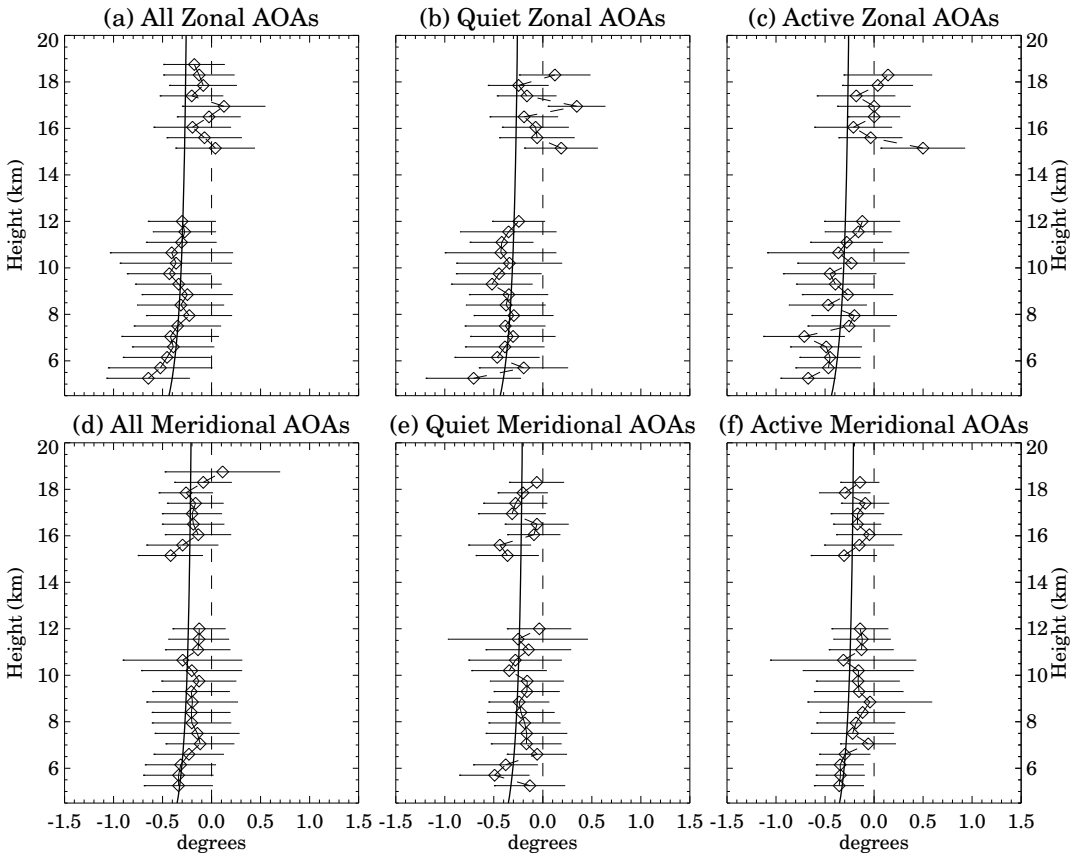

Figure 6.5. Zonal and meridional AOAs for the three selected time-periods: All (first column), Quiet (second column) and Active (third column) time periods. Median values are shown by diamonds and standard deviations are shown by horizontal solid lines. The solid curve in each plot represents theoretical values from Chapter 5 expected from an isotropic atmosphere, given the antenna geometry and pointing direction. The vertical dashed lines represent AOAs of zero degrees.

biases due to the variable geometrical contributions.

• Some vertical velocity characteristics. In Figure 6.6 we provide pertinent results for the standard deviation (σ_w) and percentage of failures (α_w) of the vertical velocity profiles for all three periods. Results are shown for the following techniques: a narrow beam Zenith technique (Wn), a "corrected" vertical velocity technique (FCAM), a "quasi" DBS technique (PSS) and a wide beam Zenith technique (Ww).

Examination of Figure 6.6 shows large variations of the percentage of failures with

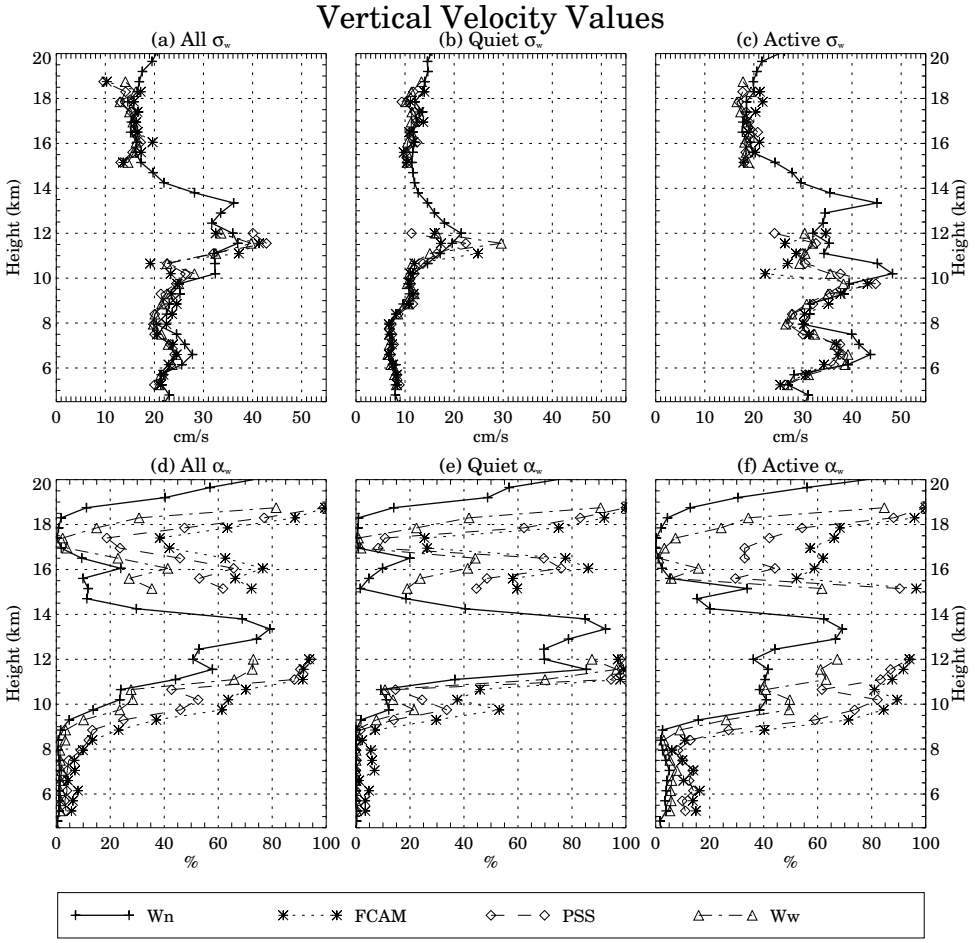

Figure 6.6. Profiles of vertical velocity characteristics: standard deviations (σ_w, upper panels) and percentage of failures (α_w, lower panels), for All (first column), Quiet (second column) and Active (third column) time periods. The w measurements are: Wn ($+$), FCAM ($*$), PSS ($\diamond$) and Ww ($\triangle$).

heights, with the largest failures occurring in the regions of weakest SNR (see Figure 6.2). Also, the inferred measurements (FCAM, PSS) exhibit large values of α ($> 10\%$) below 12 km and during the active conditions. The standard deviation estimates of all the techniques show $\sigma_w < 20$ cm s^{-1} during the quiet period, and $\sigma_w \geq 20$ cm s^{-1} during the active period. However, during the active period and below 12 km, the variance of the narrow beam technique is larger than the variance of the other techniques.

We present in Figures 6.7 and 6.8 a statistical comparison of various vertical velocity techniques. Using Wn as a reference, we first compare four "classical" SA techniques (FCA-type) in Figure 6.7. The other vertical velocity measurements (PSS, Ww and FCAr) are then compared against the same reference in Figure 6.8. All comparisons are done in terms of: (a) mean velocity difference ($\mu_{\Delta w}$), (b) standard deviation of the velocity difference ($\sigma_{\Delta w}$), and (c) correlation coefficient between velocities ($\rho_{\Delta w}$).

Examination of Figure 6.7 shows excellent agreement among the four "corrected" vertical velocity measurements ($\hat{w}$) at tropospheric heights, where all the techniques give similar values of $\mu_{\Delta w}$, $\sigma_{\Delta w}$ and $\rho_{\Delta w}$. Above 15 km, however, some discrepancies can be seen, particularly for the active period. Note that the mean differences ($\mu_{\Delta w}$) of $\hat{w}$ tend to be negative below 12 km and positive above 15 km during all three periods.

The general characteristics of the $\hat{w}$ standard "errors" ($\sigma_{\Delta w}$) apparent in Figure 6.7 are that they: (a) increase significantly with increasing height up to 12 km, (b) are relatively constant and small above 15 km, and (c) increase at all heights with increased wind activity. The $\hat{w}$ correlation coefficients, on the other hand, tend to decrease slightly with increasing height, and increase at all heights with increased wind activity.

Comparable statistical comparisons for the other ("uncorrected") vertical

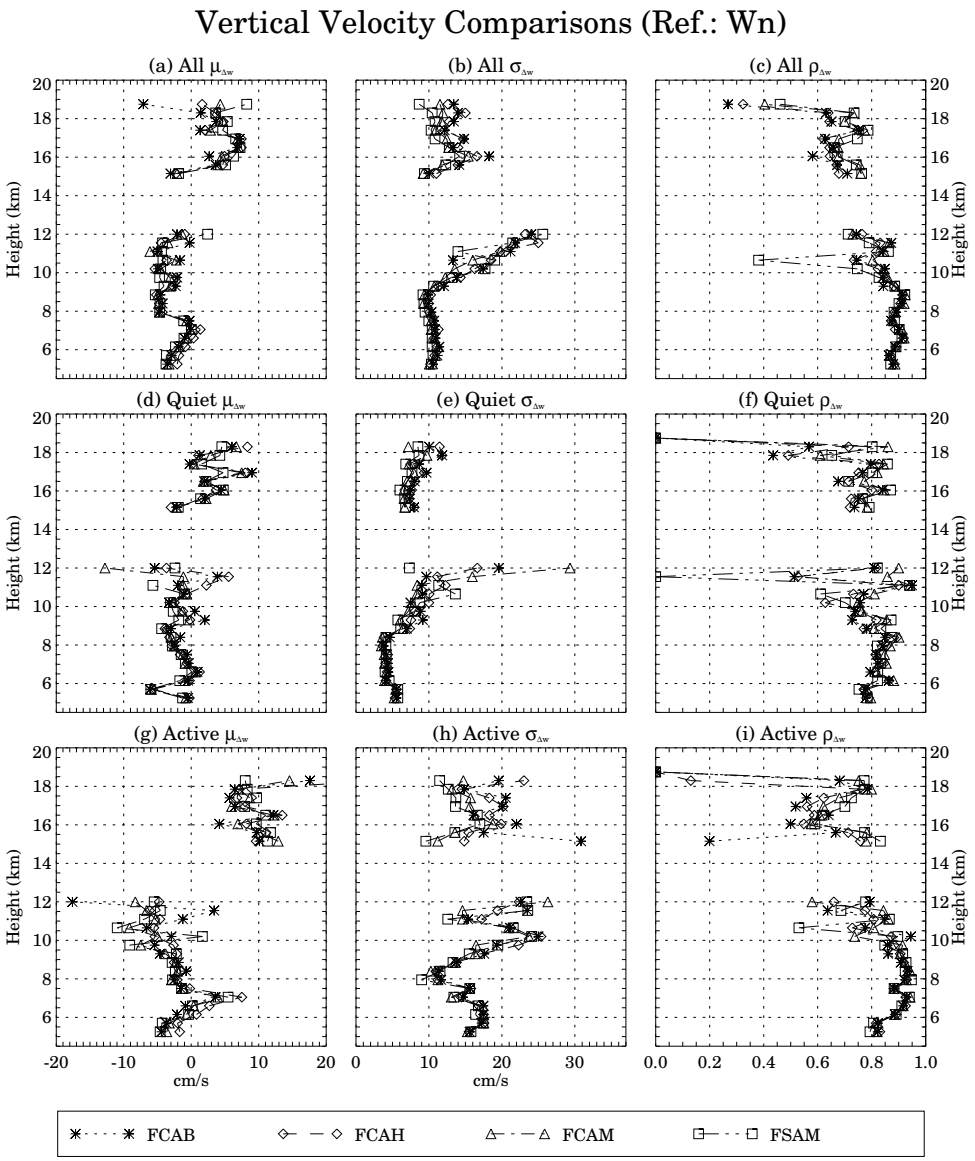

Figure 6.7. Profiles of vertical velocity comparisons for the following FCA-type measurements: FCAB ($*$), FCAH ($\diamond$), FCAM ($\triangle$) and FSAM ($\square$), using Wn as a reference. The comparisons are in terms of: mean velocity differences ($\mu_{\Delta w}$, first column), standard deviation of the velocity differences ($\sigma_{\Delta w}$, second column) and correlation coefficient ($\rho_{\Delta w}$, third column), for All (first row), Quiet (second row) and Active (third row).

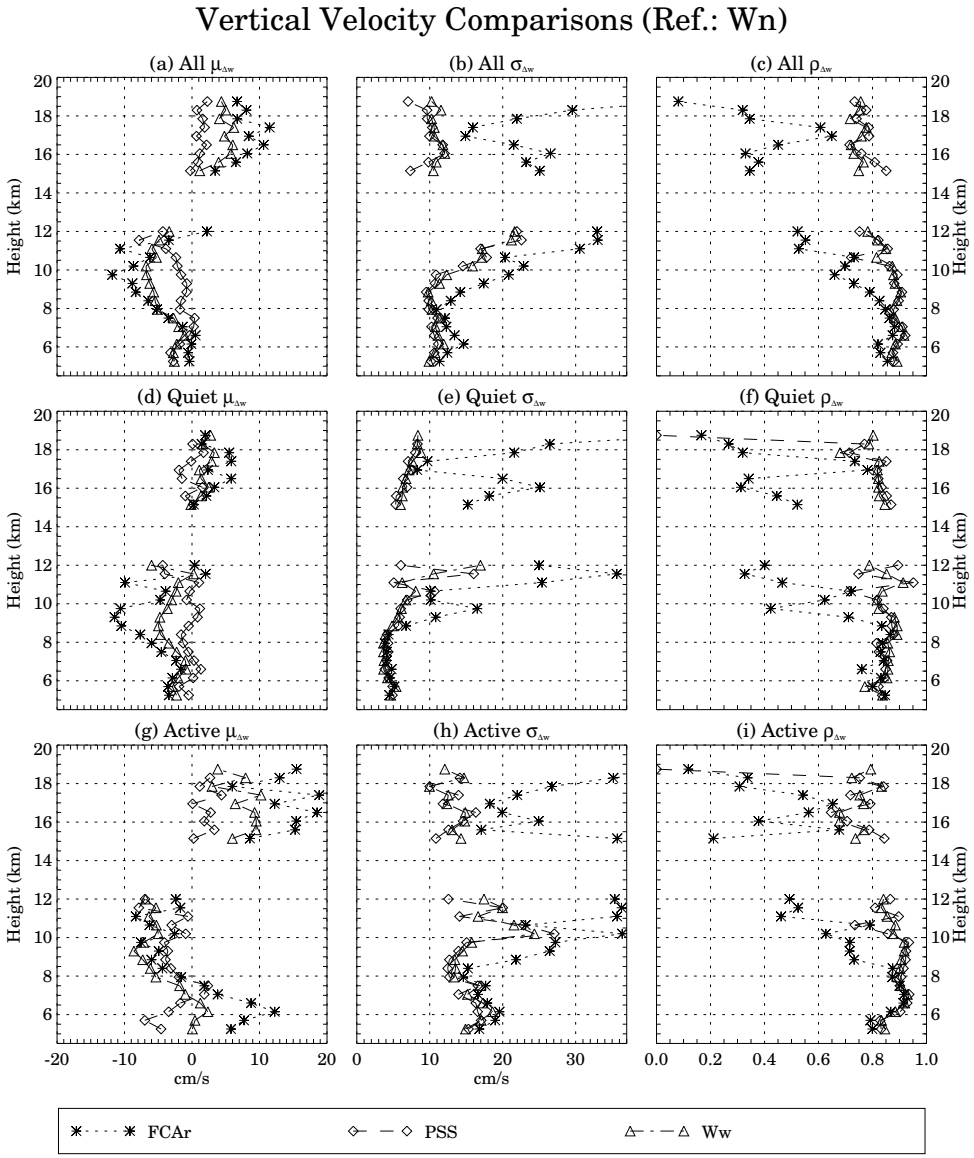

Figure 6.8. Profiles of vertical velocity comparisons for the following measurements: FCAr ($*$), PSS ($\diamond$) and Ww ($\triangle$), using Wn as a reference. The comparisons are in terms of: mean velocity differences ($\mu_{\Delta w}$, first column), standard deviation of the velocity differences ($\sigma_{\Delta w}$, second column) and correlation coefficient ($\rho_{\Delta w}$, third column), for All (first row), Quiet (second row) and Active (third row).

velocity measurements appear in Figure 6.8. To facilitate comparisons with Figure 6.7 results, we have included the "off-vertical" radial measurements (FCAr). It is worth noting that the biggest biases and errors and smallest correlations are given by these radial velocities.

The standard "errors" and correlation coefficient results for the Ww (triangles) and PSS (diamonds) techniques are very similar to the "corrected" results presented in Figure 6.7. The mean differences ($\mu_{\Delta w}$), on the other hand, show significant discrepancies: Ww differences are larger and PSS differences smaller than the differences shown in Figure 6.7.

In order to better see these differences, we have plotted in Figure 6.9 the mean values of the two Zenith techniques (Wn and Ww), in addition to a "classical" SA technique (FCAM) and the "quasi" DBS technique (PSS). Examination of Figure 6.9 shows that the Ww measurements tend to give downward velocities below 12 km, and upward velocities above 15 km. Similar comments can be applied to the FCAM results, although the Ww measurements tend to give more biases than the FCAM results, even when Wn is upward, i.e., at mid-tropospheric heights.

On the other hand, PSS results are in somewhat better agreement with the reference, particularly during quiet conditions ($|\mu_{\Delta w}| \leq 1$ cm s^{-1}). During active conditions, the PSS measurements also give negative mean differences at tropospheric heights and positive mean differences above 15 km relative to the reference profile (see Figure 6.8). Nonetheless, these mean differences are, in general, less than those obtained from the other techniques.

In Figure 6.10 we present the standard deviations of the vertical velocity difference (using Wn as reference), and the correlation coefficients between both wide and narrow beam measurements (stars). In addition we present the approximated values of the statistical errors (σ_ϵ) of the "instantaneous" vertical velocities (diamonds in upper panels), and theoretically-derived correlation coefficients ($\hat{\rho}_{\Delta w}$)

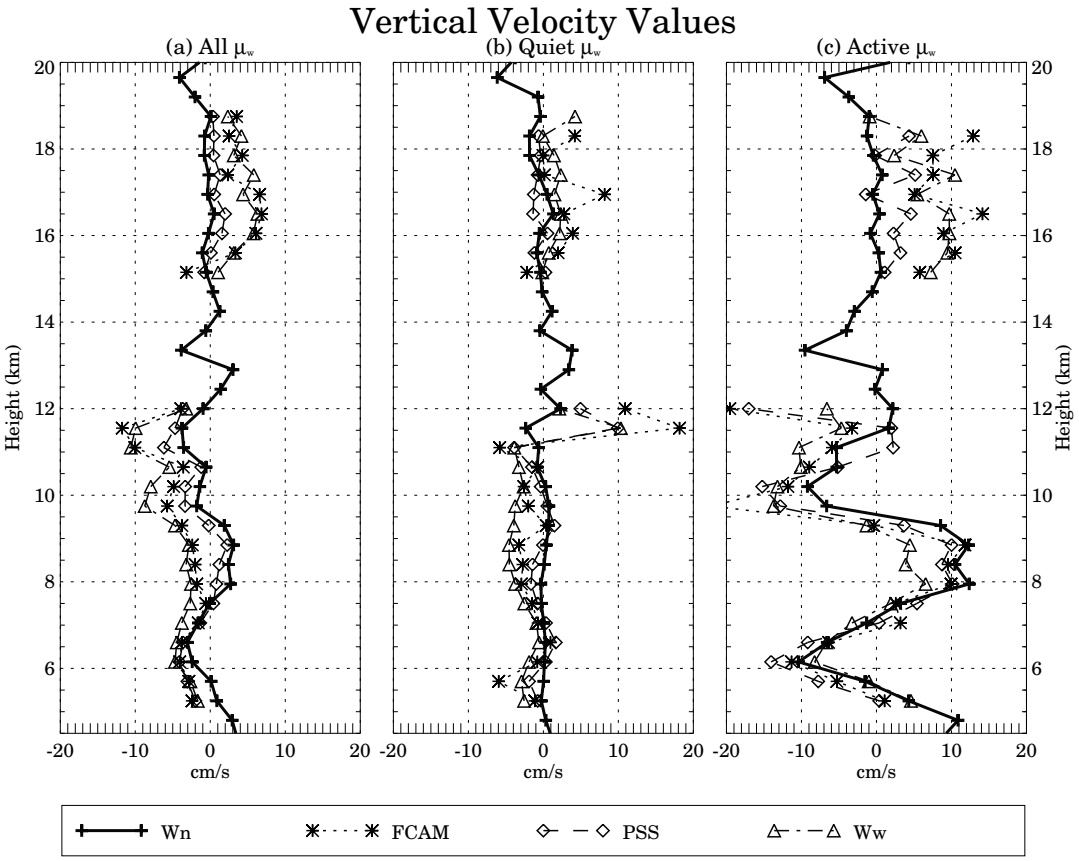

Figure 6.9. Profiles of mean vertical velocities (μ_w) for time-intervals of events (a) All, (b) Quiet and (c) Active. The measurements are: the reference profile Wn(+), FCAM ($*$), PSS ($\diamond$), and Ww ($\triangle$).

(diamonds in lower panels). The last two quantities have been obtained from:

$$\sigma_\epsilon^2 = \frac{\sigma_{\Delta w}^2}{2} \tag{6.4}$$

$$\hat{\rho}_{\Delta w} = \frac{\hat{\sigma}_w^2}{\sqrt{\hat{\sigma}_w^4 + \hat{\sigma}_w^2 \sigma_{\Delta w}^2 + \sigma_{\Delta w}^4/4}} \tag{6.5}$$

We have assumed that,

$$W_n = \bar{w} + w + x \tag{6.6}$$

$$W_w = \bar{w} + \Delta w + w + y \tag{6.7}$$

where W_n is the narrow beam and W_w the wide beam vertical velocities, $\bar{w}$ is the

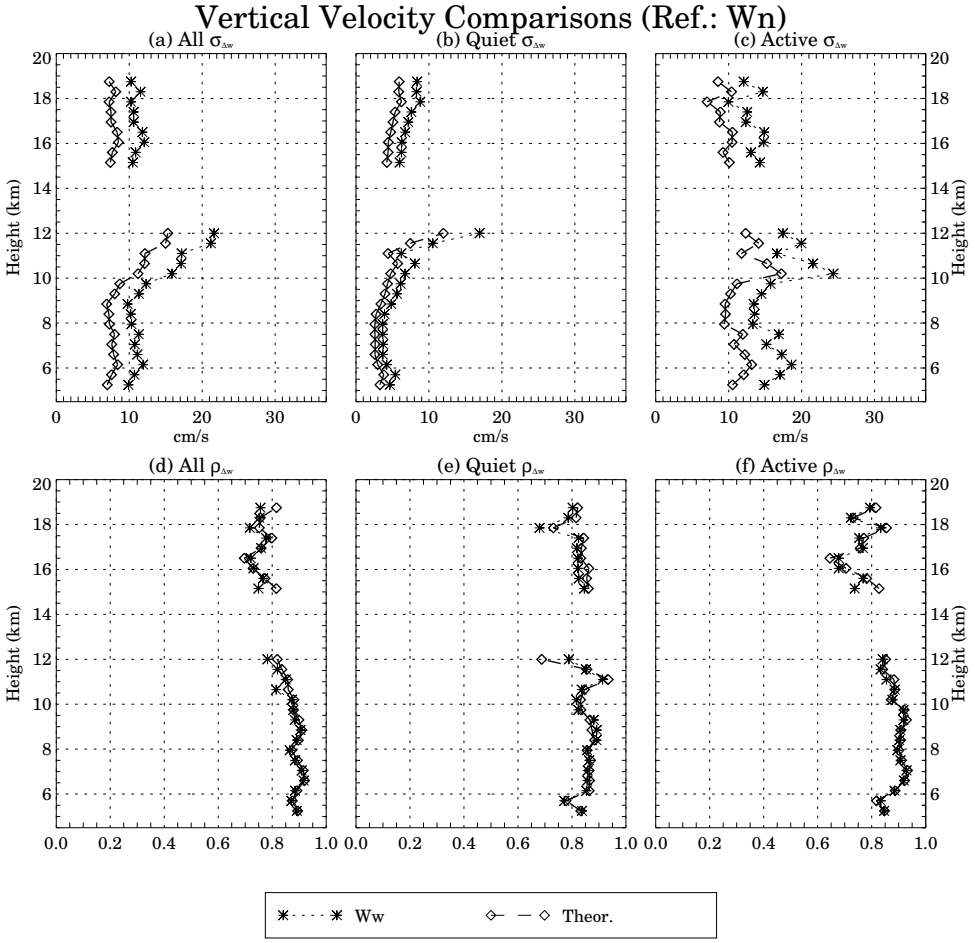

Figure 6.10. Standard deviations of the differences ($\sigma_{\Delta w}$ by stars in upper panels) and correlation coefficients ($\rho_{\Delta w}$ by stars in lower panels). In addition to the standard "errors" of vertical velocities (σ_ϵ by diamonds in first column) and theoretical-derived correlation coefficients ($\hat{\rho}_{\Delta w}$).

common mean vertical velocity, Δw is a constant difference, w is the "true" geophysical vertical velocity perturbation, and x and y are the "statistical" errors in the narrow and wide beam, respectively. The geophysical (w) and "statistical" (x and y) components have been assumed to be uncorrelated zero-mean Gaussian random processes with variances $\hat{\sigma}_w^2$, σ_x^2 and σ_y^2, respectively. Furthermore, the "statistical" variances of the two measurements are assumed to be equal, i.e., $\sigma_x^2 = \sigma_y^2 = \sigma_\epsilon^2$. The geophysical variance ($\hat{\sigma}_w^2$) is obtained from the difference between the narrow beam variance (σ_w^2 for Wn in Figure 6.6) and the "statistical" variance (σ_ϵ^2). A similar approach can be applied to the other vertical velocity techniques.

Given the good agreement between the measured and the theoretical correlation coefficients, approximated standard "errors" in the vertical velocities are between 2 cm s^{-1} and 5 cm s^{-1} during the quiet period, and $\approx$ 10 cm s^{-1} during the active period.

6.5 Discussion

This section begins by discussing the validity of using the narrow beam Zenith technique (Wn) as a reference for vertical velocity comparisons. Consider the following points:

• Theoretically the mean vertical velocity, $\bar{w}$, should go to zero at the tropopause in response to the reversal of the quasi horizontal temperature gradient. Moreover, even though the Jicamarca radar is located in a mountainous region, one would expect that under quiet conditions $\bar{w} \approx 0$. Finally, under active conditions, there could be a gravity wave with a vertical component of propagation. Such a wave, due to orographic effects, would decay in intensity with increasing height. This wave could have several levels of non-divergence (LNDs) without violating any physical principle (e.g. Bluestein [1992]). All of these statements appear to be best matched to the Wn profiles in Figure 6.9.

• The SNR of the narrow beam antenna (E) should be higher than the SNR obtained using the other antennas. It follows that Wn measurements will show less statistical uncertainties than the other w measurements (e.g. Woodman [1985]). The results shown in Figure 6.2 support this statement.

On the basis of these arguments we consider that Wn is a reasonably good reference profile for our comparisons. We now proceed to discuss the results obtained using the other techniques.

• Wide beam results (Ww). The profiles shown in Figure 6.8 provide a consistent picture of the mean relative differences between Ww and the reference profile. Specifically, the Figure 6.8 profiles show consistent negative values below 12 km and equally consistent positive values above 15 km. Presumably, most of these discrepancies are beam-width dependent. Moreover, in most of the heights these mean differences are proportional to the variability of the vertical wind. Above 15 km, there are also discrepancies apparent in the "instantaneous" values given by the relatively low correlation coefficients (Figure 6.8).

We have also examined the possibility that the wide and narrow beam discrepancies are due to the type of estimator used, and conclude that this is not the case. Different velocity estimators have been applied to both direct measurements using three ground clutter removal procedures, two types of spectral windows (Hanning and rectangular), and two moment estimators (NOAA's algorithm, Gaussian fitting). The greatest mean difference between estimators was less than 0.5 cm s^{-1}.

Similar patterns to the wide beam results, i.e., sinking in the troposphere and rising in the stratosphere, have been obtained at the tropics (Gage et al. [1991b]; Huaman and Balsley [1996]) and at mid-latitudes (Fukao et al. [1991]; Yoe et al. [1992]; Nastrom and VanZandt [1994]). The results at the tropics, however, are of smaller magnitude than the wide beam results, but the beam-widths in the tropics are also smaller ($\approx 2^{\circ}$). On the other hand, the results at mid-latitudes are of similar magnitude to

the wide beam results at Jicamarca. Recently, Muschinski [1996] has theoretically associated the effects of Kelvin-Helmholtz Instability (KHI) to the mean vertical velocity biases seen at mid-latitudes. The "KHI bias" is downward in the shear zone below the horizontal wind speed maximum of a jet stream and upward above. Muschinski has also suggested that the direction of the AOAs is defined by the sign of $\partial u/\partial z$. In our case, the wide beam vertical velocity profile changes direction around 15 km (Figure 6.9), while the horizontal wind speed maximum is above 17 km (Figure 6.4). Our median values of AOAs (Figure 6.5), however, appear to be uncorrelated with the sign of $\partial u/\partial z$ (Figure 6.4). From these statements, KHI effects alone are not the cause of the Wn and Ww discrepancies.

• "Quasi" DBS results" (PSS). In contrast to the wide beam results, PSS/Wn comparisons show better agreement in the mean values. It appears that by sampling different pointing directions (nine), we have decreased the differences present in the Ww results, particularly during quiet conditions. The PSS "instantaneous" results, on the other hand, show strong similarities to the Ww results.

• "Classical" SA results (FCA-type). Analysis of the "true" velocity estimators (FCAM, FCAB, FCAH and FSAM) shows good agreement among their measurements in the lower troposphere. This agreement corresponds to: (a) similar correlation coefficients ($\rho_{\Delta w} > 0.8$), (b) similar biases (within ± 0.5 cm s^{-1}), and (c) similar standard "errors". Most of the discrepancies between the FCA-type estimators are seen above 15 km. These results are consistent with the discrepancies in horizontal velocity estimates discussed in Chapter 4.

Comparing the radial velocity results (FCAr) of Figure 6.8, with the $\hat{w}$ results of Figure 6.7, we see that a major improvement is achieved using the corrected values (higher correlations, lower standard "errors" and lower "biases") than by using the radial velocities. Below 12 km, the biases given by the FCA-type techniques are less than those given by Ww, but still ≈ -1 cm s^{-1} and ≈ -4 cm s^{-1} for the quiet

and active period, respectively. Moreover, at these heights, the FCA-type results are closer to the Ww results than to the Wn results. Above 15 km, $\hat{w}$ results are very similar to Ww results, i.e. both exhibit similar rising motions.

Even though we have shown improvements of corrected vertical velocities relative to those obtained using direct measurements on the vertical wide beam, we have the following concerns with these corrections:

• Horizontal velocity percentage of failures. Since the corrections are done in a SA system, the horizontal velocity is obtained from a SA technique. However, the percentage of failures of the SA horizontal velocity techniques are $> 10\%$ (see Chapter 4). This failure rate causes a similar number of failures on the corrected vertical velocities. While these "gaps" are not so important in determining mean values of w, short-term spectral studies (e.g. gravity wave parameterization) will be strongly affected. This problem could be reduced by using other horizontal velocity estimates, e.g., the horizontal wind estimates from a simultaneous DBS configuration.

• Horizontal velocity magnitude. From the results presented in Chapter 4, and also in Section 6.4, we see that most SA "true" velocity estimators give close to the same horizontal values at lower tropospheric heights. Above 15 km, however, the horizontal velocity estimates using these different techniques vary considerably. In general, with respect to the horizontal velocity reference (FCAM), (a) FSAM estimates give underestimated values while (b) FCAB and FCAH estimates give overestimated values. As a result, the different techniques produce different corrected vertical velocities. Coincidentally, these heights are characterized by lower SNR and more aspect sensitivity than the tropospheric heights.

• Angle-of-arrival statistical errors. Typical statistical errors in AOA measurements are $\approx 0.15^{\circ}$ for 3-minute estimates (see Chapter 5). The magnitude of these errors decreases with increasing integration time. In long-term measurements, these errors should average out. However, in studies using short-term w measurements

(< 15 min.) these AOA errors can be significant, particularly during quiet periods when the w oscillations are low ($\sigma_w < 8$ cm s^{-1}). For example, a 20 m s^{-1} horizontal wind velocity would produce a vertical velocity error of 5 cm s^{-1}, a value comparable to the w fluctuations.

Although, in general, the corrected vertical velocities (for off-vertical effective pointing) compare better than the Ww velocities, with the Wn reference , they still show significant mean differences ($\approx$ -1 to -4 cm s^{-1} below 12 km and $\approx$ 3 to 8 cm s^{-1} above 15 km). Assuming that our reference is reasonable, there must be factors other than off-vertical effective pointing that contribute to biases in the wide beam techniques. It is important to stress that SA techniques also use wide beam antennas. Other possible factors that could contribute to the vertical velocity mean differences could be due to:

• Gravity waves. Nastrom and VanZandt [1994] suggested that downward-moving portion of gravity waves with a vertical component of propagation would exhibit larger reflectivity than the upward moving portion. Ww and the corrected vertical velocities seem to be in agreement with this theory, i.e. they show stronger downward velocities than our reference. However, this theory does not explain why Wn and PSS results do not show such pronounced downward velocities.

• Wind-field gradients. Larsen and Palmer [1997] and Palmer et al. [1997a] showed how gradients in the wind field could affect vertical velocity and AOA estimates obtained from a finite beam-width radar. Divergence effects depend on the beam-width, so that the smaller the beam-width the smaller the errors on w due to divergence. This process would explain differences between Wn and Ww measurements. It would also explain the closer agreement between corrected vertical velocities ($\hat{w}$) and Ww, relative to the poorer agreement between $\hat{w}$ and Wn. In addition, if vorticity is playing a major role, AOAs will be contaminated. This would produce biases in $\hat{w}$ estimates (Larsen and Palmer [1997]). The PSS results are explained if the

wind-field gradient effects depend on zenith angle, since those effects appear to be averaged out in our nine-beam configuration. Assuming that approximate values of horizontal divergence can be obtained from $\partial w/\partial z$ (continuity equation), profiles of the wide beam mean differences should change sign during the active period, particularly below 12 km. However, our observations do not display such a change of sign. We are not able to quantify the effects of gradients in the wind-field because we did not have other means to measure divergence and vorticity at the time of the experiment.

Examining Figure 6.9, we can see that the 5-day mean average has influences from the active mean values. These active mean values are almost certainly caused by orographic effects. Therefore, if validity of Wn measurements has to be tested against vertical velocities obtained by operational analysis, one would need quiet conditions to avoid this "meteorological" noise (Nastrom et al. [1985]).

6.6 Conclusions

We have shown that the choice of the narrow beam vertical velocity profile is a reasonable reference (Wn) for comparing a variety of vertical velocity measurement techniques. Our choice was based on the reasonable value of the observed mean vertical velocity profile, and on the high SNR signals available at almost all heights using this technique. While this type of measurement appears to give the most reasonable vertical velocity results, implementation of the Wn technique is very expensive. It is important to stress that the most reasonable profile is not necessarily the correct profile. In lieu of a true "standard" for comparison, it will be ultimately necessary to compare radar results with other methods. Currently the best comparison appears to lie with the synoptic-scale vertical velocity obtained from observational analysis.

The wide beam results (Ww) exhibit substantial discrepancies, primarily

in the mean values relative to the Wn profiles. The Ww show downward mean differences at tropospheric heights, and upward mean differences above 15 km. On the other hand, the validity of "instantaneous" vertical velocities obtained by wide beams are somewhat guarantee. Both wide and narrow beam Zenith techniques show very similar values of variances. Given the high correlation coefficients between both techniques, the small discrepancies in the instantaneous values are almost certainly of statistical nature. The statistical "errors" are < 5 cm s^{-1} during quiet conditions and ≈ 10 cm s^{-1} during active conditions. Similar conclusions can be inferred for the "instantaneous" vertical velocities of the other techniques, particularly below 12 km.

The PSS results are also very encouraging. Even though the PSS technique is supposed to be affected by anisotropic scattering, PSS results show better agreement with the reference than either the vertical wide beam profiles or the "corrected" profiles.

The concept of correcting vertical velocities does appear to work. Using the SA configuration, we were able to obtain "corrected" vertical velocities by compensating our "off-vertical" echo returns by subtracting out the horizontal velocity contributions. These off-vertical returns include a systematic contribution ("off-vertical" angle $> 0.46°$) due to the antenna pointing directions and the geometry of the SA system, as well as atmospheric contributions that can have instantaneous off-vertical values as high as 1°. While these corrected measurements give better mean value results than the wide beam Zenith technique, the corrected mean values lie between the Wn and Ww results, and are close to Ww profile.

Based on the above discussions, vertical velocity measurements, particularly mean values, appear to be affected not only by "effective" beam pointing problems, but also by other effects that depend on the radar beam-width. Future comparisons of narrow beam and wide beam results will help to qualify and possible to quantify

these beam-width-depend effects.

CHAPTER 7

SUMMARY AND FUTURE WORK

In this thesis, we have examined a number of techniques for wind velocity estimation, and have put special emphasis on the vertical component of the wind. In the process of these examinations, we have studied the angle-of-arrival (AOA) measurements that are needed for a specific type of vertical velocity techniques.

In Chapter 4, we have shown that the simpler horizontal velocity techniques that assume horizontally isotropic scattering compare very closely with more complicated full correlation analysis techniques, particularly below 12 km. The assumption of a Gaussian form of the cross-correlation functions is demonstrated to be reasonable at high SNR tropospheric heights. In general, for all of the horizontal velocity techniques examined, there is excellent agreement in the wind direction. On the other hand, considerable discrepancies between techniques occur in the wind speed estimates, particularly above 15 km.

In Chapter 5, based on scattering theory, we have shown that the interpretation of AOA measurements has been improved. We have isolated the contributions from (1) tilted layers, (2) antenna pointing, and (3) geometrical contributions. It is also shown that the estimation of most AOA contributions, requires the measurement of the scattering parameters. In addition, we have shown that the correction of vertical velocities can be accomplished without explicitly determining the off-vertical atmospheric contributions. The comparisons of a time- and a frequency-domain method for AOA measurements showed that the time-domain method is easier to implement, faster to calculate, and more reliable than the frequency-domain method. Assuming that the scattering, on average, is isotropic, AOA radar measurements are

in good agreement with theoretical values.

May [1993] suggested that collocated SA systems (where the transmitting antenna is centered on the array of receiving antennas) should be used in vertical velocity corrections instead of non-collocated configurations. However, using scattering theory and based on the same arguments used by May, we have shown in Section 5.3 that such corrections can be done even if one uses non-collocated systems. It is important, however, to correctly use the AOA and radial velocity information. Having said this, it still may be possible that there are other factors, which were not considered in our development, that make non-collocated systems unsuitable for vertical velocity corrections.

The choice of the narrow beam vertical velocity (Wn) profile as a reference (Chapter 6) has been shown to be reasonable for comparing concurrent vertical velocity measurements obtained by a variety of techniques. Our choice to use the narrow beam as a reference was based on the reasonable value of the mean of the observed vertical velocity profile, and the high SNR signals available at almost all heights using this technique. While the narrow beam measurement appears to give the most reasonable vertical velocity results, implementation of the technique is very expensive and more feasible alternatives should be considered.

Comparison of the vertical velocity techniques under different scenarios, shown in Table 7.1, is summarized with a subjective rating. We rate the following vertical velocity techniques: narrow beam Zenith technique (Wn), wide beam Zenith technique (Ww), "quasi" DBS technique (PSS) and the "classical" SA technique ($\hat{w}$). Our ratings are based on the results presented in Chapter 6. Specifically, the ratings on mean vertical velocities come from the results presented in Figure 6.9. The key for these ratings is: poor ($\star$), moderate ($\star\star$), good ($\star\star\star$), excellent ($\star\star\star\star$) and perfect ($\star\star\star\star\star$). Examination of Table 7.1 shows that the overall rating for each technique is: excellent for the narrow beam Zenith technique, moderate for the wide

beam Zenith technique, good for the "quasi" DBS technique, and moderate for the "classical" SA techniques.

Table 7.1. Subjective ratings for vertical velocity techniques. [Wn: narrow beam Zenith, Ww: wide beam Zenith, PSS: "quasi" DBS, and $\hat{w}$: "classical" SA]

	Wn	Ww	PSS	$\hat{w}$
Below 12 km	⋆⋆⋆⋆	⋆⋆	⋆⋆⋆	⋆⋆⋆
Above 15 km	⋆⋆⋆⋆	⋆⋆	⋆⋆⋆	⋆
Quiet conditions	⋆⋆⋆⋆	⋆⋆	⋆⋆⋆	⋆⋆
Active conditions	⋆⋆⋆	⋆⋆	⋆⋆	⋆⋆
Mean values	⋆⋆⋆⋆	⋆	⋆⋆⋆	⋆⋆
3-minute values	⋆⋆⋆	⋆⋆⋆	⋆⋆	⋆
On-line processing	⋆⋆⋆⋆	⋆⋆⋆⋆	⋆⋆⋆	⋆⋆
Overall	⋆⋆⋆⋆	⋆⋆	⋆⋆⋆	⋆⋆

It is important to stress here that an excellent profile rating does not necessarily imply that the profile is correct. In lieu of a true "standard" for comparison, it ultimately will be necessary to compare radar results with other methods. Currently the best comparison appears to lie with the synoptic-scale vertical velocity obtained from observational analysis.

Improvements to three-dimensional wind velocity measurement comparisons could be achieved in the future with the following activities:

• More narrow-wide beam comparisons. The cause of the discrepancies between narrow and wide beam vertical velocities is still not fully understood. Complementary measurements of divergence and vorticity by observational analysis could help to quantify their effects on vertical velocity measurements. A climatology of the narrow beam measurements could help to validate better these type of measurements. Nowadays, these type of measurements are only possible using the Jicamarca Radar.

• Concurrent collocated and non-collocated SA measurements. These types of measurements could help to confirm the assumptions used in Chapter 5. These additional measurements would give more inputs on the understanding of the actual scattering process. This configuration could be achieved using either the Jicamarca Radar or

the MU radar.

• Experiments using higher sensitivity. Among the various techniques studied throughout this thesis, most of the discrepancies occur above 12 km, where SNR values are low. The use of more power (> 100 kW) or pulse-coding would help to increase the SNR at these heights. This improvement would, in turn, increase the understanding of the observed discrepancies, particularly in the case of the SA techniques. Pulse-coding was not implemented in the data used in this work. This choice enabled us to have the lowest possible height coverage. These recommended experiments can be done by any SA VHF system with high power capabilities.

• Concurrent Full-DBS and SA measurements. The horizontal winds obtained with the Full-DBS configuration can be used to get corrected vertical velocities. This procedure decreases the percentage of gaps on such vertical velocities. As mentioned in Chapter 3, the Jicamarca radar is not suitable for Full-DBS measurements. This is because the maximum oblique angles are small, so horizontal velocity estimates are affected by aspect sensitivity (Tsuda et al. [1986]). The MU radar is an appropriate choice for these type of measurements.

• Scattering theory and the use of multiple receiving antennas. With some modifications to the scattering model used in Chapter 5, one can study the feasibility of using at least four non-coplanar receiving antennas for vertical velocity measurements. Moreover, the use of multiple antennas (coplanar or non-coplanar) allows the relaxation of some simplifying assumptions. For example, one can then assume that the spatial spectrum of the refractive index field is composed of more than one Gaussian "blob" (Woodman 1997, personal communication). Not only the wind-velocity estimation could be improved with this approach but also the "imaging" of the atmospheric scattering mechanisms could be achieved. We have already collected data with a four-antenna and a seven-antenna configuration. The processing of these data will be done in the near future. In addition, the PSS pointing can be

more precisely determined not only by incorporating aspect sensitivity parameters but also by using more than three receiving antennas.

A further benefit of using scattering theory is that one can study the feasibility of using rectangular antennas in SA techniques. For example, it is possible to make an SA modification to existing wind profilers that have two collocated COCO (coaxial collinear) antennas. This modification could split each antenna in halves, so that the resultant SA system would be composed of four rectangular antennas. The same array could be used simultaneously in the normal DBS mode, without loss of data.

• Evaluation of wind velocity estimators using simulated data. The precision of each of the wind velocity techniques has been a concern throughout this work. A careful evaluation of the different techniques using simulated data could better quantify the statistical uncertainties expected for each technique (May [1988]; Frehlich et al. [1994]). Not only can the statistical errors on the velocity estimators be obtained but also the statistical errors in AOAs and scattering parameters. Moreover, the generation of simulated data can be greatly improved by incorporating theoretical cross-correlation functions obtained with the scattering theory mentioned above.

• Scattering modeling. A simple computer model similar to the one presented by Holdsworth and Reid [1995] and Chau et al. [1995], could help to implement components that are not easy to incorporate on the scattering theory or simulated data. For example, one can incorporate a monochromatic specular wave in the model to study its effects on the different velocity estimators.

BIBLIOGRAPHY

Armstrong, J. W., and W. A. Coles, Analysis of three-station interplanetary scintillation, **J. Geophys. Res.**, **77**(25), 4602–4610, 1972.

Balsley, B., and R. Garello, The kinetic energy density in the troposphere, stratosphere, and mesosphere: a preliminary study using the Poker Flat MST radar in Alaska, **Radio Sci.**, **20**, 1355–1361, 1985.

Balsley, B. B., The MST technique - A brief review, **J. Atmos. Terr. Phys.**, **43**, 495–509, 1981.

Balsley, B. B., and D. A. Carter, Mountain waves in the tropical Pacific atmosphere: A comparison of vertical wind fluctuations over Pohnpei and Christmas Island using VHF wind profilers, **J. Atm. Sci.**, **46**, 2698–2715, 1989.

Balsley, B. B., and A. C. Riddle, Monthly mean values of the mesospheric wind field over Poker Flat, Alaska, **J. Atm. Sci.**, **41**, 2368–2375, 1984.

Balsley, B. B., W. L. Ecklund, D. A. Carter, A. C. Riddle, and K. S. Gage, Average vertical motions in the tropical atmosphere observed by a radar wind profiler on Pohnpei (7°N latitude, 157°E longitude), **J. Atm. Sci.**, **45**(3), 396–405, 1988.

Barnes, S. L., On the accuracy of Omega diagnostic computations, **Mon. Weather Rev.**, **114**, 1664–1680, 1986.

Battan, L. J., **Fundamentals of Meteorology**. Prentice-Hall, Inc., 1979.

Belt, C. L., and H. E. Fuelberg, The effects of random errors in rawinsonde data on derived kinematic quantities, **Mon. Weather Rev.**, **110**, 91–101, 1982.

Bluestein, H. B., **Synoptic-Dynamic meteorology in midlatitudes.** Oxford University Press, 1992.

Briggs, B. H., Radar observations of atmospheric winds and turbulence: a comparison of techniques, **J. Atmos. Terr. Phys.**, **42**, 823–833, 1980.

Briggs, B. H., The analysis of spaced sensors records by correlation techniques, in **Handbook for the Middle Atmosphere Program**, pp. 166–186, University of Illinois, Urbana. Special Committee for Solar-Terrestrial Physics Secretariat, 1984.

Briggs, B. H., and A. D. Maude, Spaced sensor observations of pattern motion, **J. Geophys. Res.**, **83**(A11), 5309–5311, 1978.

Briggs, B. H., and R. A. Vincent, Spaced-antenna analysis in the frequency domain, **Radio Sci.**, **27**(2), 117–129, 1992.

Briggs, B. H., G. J. Phillips, and D. H. Shinn, The analysis of observations on spaced receivers of the fading radio signals., **Proc. Phys. Soc. London**, **63**, 106–121, 1950.

Brown, W. O., G. J. Fraser, S. Fukao, and M. Yamamoto, Spaced antenna and interferometric velocity measurements with MF and VHF radars, **Radio Sci.**, **30**(4), 1281–1292, 1995.

Chau, J. L., B. B. Balsley, and L. E. Liziola, Preliminary results using a simple scattering model, Extended abstract and poster. Ninth International Symposium on equatorial aeronomy, Bali, Indonesia, 1995.

Cohn, S. A., C. L. Holloway, S. Oncley, R. Doviak, and R. Lataitis, Validation of a UHF spaced antenna wind profiler for high resolution boundary layer observations, **Radio Sci.**, **32**(3), 1279–1296, 1997.

Currier, P. E., S. A. Avery, B. B. Balsley, K. S. Gage, and W. L. Ecklund, Combined use of 50 MHz wind profilers in the estimation of raindrop size distributions, **Geophys. Res. Lett.**, **19**, 1017–1020, 1992.

Doviak, R., and D. S. Zrnič, **Doppler radar and weather observations**. Academic Press, Inc., second edn., 1993.

Doviak, R. J., R. J. Lataitis, and C. L. Holloway, Cross correlations and cross spectra for spaced antenna wind profilers, **Radio Sci.**, **31**(1), 157–180, 1996.

Dunn, L. B., Evaluation of vertical motions: Past, present, and future, **Wea. Forecasting**, **6**, 65–75, 1991.

Durran, D. R., and L. W. Snellman, The diagnosis of synoptic-scale vertical motion in an operational environment, **Wea. Forecasting**, **2**, 17–31, 1987.

Ecklund, W. L., B. B. Balsley, D. A. Carter, A. C. Riddle, M. Crochet, and R. Garello, Observations of vertical motios in the troposphere and lower stratosphere using three closely spaced ST radars, **Radio Sci.**, **20**(6), 1196–1206, 1985.

Franke, P. M., D. Thorsen, M. Champion, S. J. Franke, and E. Kudeki, Comparison of time- and frequency-domain techniques for wind velocity estimation using multiple-receiver MF radar data, **Geophys. Res. Lett.**, **17**, 2193–2196, 1990.

Frehlich, R., S. M. Hannon, and S. W. Henderson, Performance of a 2-μm coherent Doppler lidar for wind measurements, **J. Atmos. Oceanic Technol.**, **11**(6), 1517–1528, 1994.

Fritts, D. C., and Z. Luo, Dynamical and radiative forcing of the summer mesospause circulation and thermal structure I, mean solstice conditions, **J. Geophys. Res.**, **100**, 3119–3128, 1995.

Fukao, S., T. Sato, T. Tsuda, M. Yamamoto, M. D. Yamanaka, and S. Kato, MU radar: New capabilities and system calibrations, **Radio Sci.**, **25**(4), 477–485, 1990.

Fukao, S., M. F. Larsen, M. D. Yamanaka, H. Furukawa, T. Tsuda, and S. Kato, Observations of a reversal in long-term average vertical velocities near the jet stream wind maximum, **Mon. Weather Rev.**, **119**, 1479–1489, 1991.

Gage, K. S., Radar observations of the free atmosphere structure and dynamics, in **Radar in Meteorology**, edited by D. Atlas, pp. 534–565. Amer. Meteor. Soc., 1990.

Gage, K. S., and G. D. Nastrom, A simple model for the enhanced frequency spectrum of vertical velocity based on tilting of atmospheric layers by lee waves, **Radio Sci.**, **25**(5), 1049–1056, 1990.

Gage, K. S., D. A. Carter, and W. L. Ecklund, The effect of gravity waves on specular echoes observed by the Poker Flat MST radar, **Geophys. Res. Lett.**, **8**(6), 599–602, 1981.

Gage, K. S., J. R. MzAfee, W. G. Collins, D. Söderman, H. Böttger, A. Radford, and B. B. Balsley, A comparison of winds observed at Christmas Island using a wind profiler Doppler radar with NMC and ECMWF analyses, **Bull. Am. Meteorol. Soc.**, **69**, 1041–1057, 1988.

Gage, K. S., J. R. McAfee, D. A. Carter, W. L. Ecklund, and A. C. R. an G. C, Long-term mean vertical motion over the tropical Pacific: Wind-profiling Doppler radar measurements, **Science**, **254**, 1771–1773, 1991a.

Gage, K. S., B. B. Balsley, W. L. Ecklund, D. A. Carter, and J. R. McAfee, Wind profiler-related research in the tropical Pacific, **J. Geophys. Res.**, **96**(Supplement), 3209–3220, 1991b.

Gage, K. S., J. R. McAfee, and G. C. Reid, Diurnal variation in vertical motion over the central equatorial Pacific from VHF wind-profiling Doppler radar observations at Christmas Island (2°N, 157°W), **Geophys. Res. Lett.**, **19**, 1827–1830, 1992.

Green, J. L., and K. S. Gage, Observations of stable layers in the troposphere and stratosphere using VHF radar, **Radio Sci.**, **15**(2), 395–405, 1980.

Hardy, K. R., and K. S. Gage, The history of radar studies of the clear atmosphere, in **Radar in Meteorology**, edited by D. Atlas, pp. 534–565. Amer. Meteor. Soc., 1990.

Hildebrand, P. H., and R. S. Sekhon, Objective determination of the noise level in Doppler spectra, **J. Appl. Meteor.**, **13**, 808–811, 1974.

Hocking, W. K., P. May, and J. Röttger, Interpretation, reliability and accuracies of parameters deduced by spaced antenna method in middle atmosphere applications, **Pure Appl. Geophysics**, **130**(2/3), 571–604, 1989.

Holdsworth, D. A., An investigation of biases in the full spectral analysis technique, **Radio Sci.**, **32**(2), 769–782, 1997.

Holdsworth, D. A., and I. M. Reid, A simple model of atmospheric radar backscatter: Description and application to the full correlation analysis of spaced antenna data, **Radio Sci.**, **30**(4), 1263–1280, 1995.

Holloway, C., R. Doviak, S. Cohn, R. Lataitis, and J. V. Baelen, Cross correlations and cross spectra for spaced antenna wind profilers 2. Algorithms to estimate wind and turbulence, **Radio Sci.**, **32**(3), 967–982, 1997a.

Holloway, C., R. Doviak, and S. Cohn, Cross correlations of fields scattered by horizontally anisotropic refractive index irregularities, **Radio Sci.**, **32**(5), 1911–1920, 1997b.

Holton, J. R., **An introduction to dynamic meteorology**. Academic Press, Inc., third edn., 1992.

Hoppe, U. P., and D. C. Fritts, High-resolution measurements of vertical velocity with the european incoherent scatter VHF radar 1. Motion field characteristics and measurements biases, **J. Geophys. Res.**, **100**(D8), 16813–16825, 1995.

Houze, R. A., Observed structure of mesoscale convective systems and implications for large-scale heating, **Q. J. R. Meteorol. Soc.**, **115**, 425–461, 1989.

Huaman, M. M., and B. Balsley, Long-term average vertical motions observed by VHF wind profilers: The effect of slight antenna-pointing inaccuracies, **J. Atmos. Oceanic Technol.**, **13**(3), 560–569, 1996.

Kudeki, E., Spaced antenna and interferometry methods, Second International School of Atmospheric radar. Lecture notes, 1995.

Kudeki, E., and R. F. Woodman, A postatistics steering technique for MST radar applications, **Radio Sci.**, **25**(4), 591–594, 1990.

Larsen, M. F., and R. D. Palmer, A relationship between horizontal flow gradients, in-beam incidence angles, and vertical velocities, **Radio Sci.**, **32**(3), 1269–1277, 1997.

Larsen, M. F., and J. Röttger, The spaced antenna technique for radar wind profiling, **J. Atmos. Oceanic Technol.**, **6**, 920–938, 1989.

Larsen, M. F., and J. Röttger, VHF radar measurements of in-beam incidence angles and associated vertical-beam radial velocity corrections, **J. Atmos. Oceanic Technol.**, **8**, 477–490, 1991.

Larsen, M. F., J. Röttger, and T. S. Dennis, A comparison of operational analysis and VHF wind profiler vertical velocities, **Mon. Weather Rev.**, **116**, 48–59, 1988.

Larsen, M. F., S. Fukao, M. D. Yamanaka, T. Tsuda, and S. Kato, A comparison of VHF radar vertical-velocity measurements by a direct vertical-beam method and by a VAD technique, **J. Atmos. Oceanic Technol.**, **8**, 766–776, 1991.

Larsen, M. F., R. D. Palmer, S. Fukao, R. F. Woodman, M. Yamamoto, T. Tsuda, and S. Kato, An analysis technique for deriving vector winds and in-beam incidence angles from radar interferometer measurements, **J. Atmos. Oceanic Technol.**, **9**(1), 3–14, 1992.

Lee, J. L., G. L. Browning, and Y. F. Xie, Estimating divergence and vorticity from the wind profiler network hourly wind measurements, **Tellus, Ser. A, Dyn. meteorol. oceanogr.**, **47A**, 892–910, 1995.

Liu, C. H., and C. J. Pan, New observational techniques for studying the dynamics of the middle atmosphere using the Chung Li VHF radar, **J. Atmos. Terr. Phys.**, **55**(7), 1055–1066, 1993.

Liziola, L. E., and B. B. Balsley, Horizontally propagating quasi-sinusoidal tropospheric waves observed in the lee of the Andes, **Geophys. Res. Lett.**, **24**(9), 1075–1078, 1997.

Low, D. J., Studies of the lower atmosphere with a VHF wind profiler, Ph.D. thesis, University of Adelaide, Australia, 1996.

Mace, G. G., and T. P. Ackerman, Assesment of error in synoptic-scale diagnostics derived from wind profiler and radiosonde network data, **Mon. Weather Rev.**, **124**, 1521–1534, 1996.

Mace, G. G., D. O. Starr, T. P. Ackerman, and P. Minnis, Examination of coupling between an upper-tropospheric cloud system and synoptic-scale diagnosed from wind profiler and radiosonde data, **J. Atm. Sci.**, **52**(23), 4094–4127, 1995.

Mattocks, C., and R. Bleck, Jet streak dynamics and geostrophic adjustments processes during the initial stages of lee cyclogenesis, **Mon. Weather Rev.**, **114**, 2033–2056, 1986.

May, P., and R. G. Strauch, Reducing the effect of ground clutter on wind profiler velocity measurements, 1997.

May, P. T., Statistical errors in the determination of wind velocities by the spaced antenna technique, **J. Atmos. Terr. Phys.**, **50**(1), 21–32, 1988.

May, P. T., Comments on "VHF radar measurements of in-beam incidence angles and associated vertical-beam radial velocity corrections, **J. Atmos. Oceanic Technol.**, **10**, 432–434, 1993.

May, P. T., and D. K. Rajopadhyaya, Wind profiler observations of vertical motion and precipitation microphysics of a tropical squall line, **Mon. Weather Rev.**, **124**(4), 621–633, 1996.

May, P. T., and R. G. Strauch, An examination of wind profiler signal processing algorithms, **J. Atmos. Oceanic Technol.**, **6**, 731–735, 1989.

May, P. T., T. Sato, M. Yamamoto, S. Kato, T. Tsuda, and S. Fukao, Errors in the determination of wind speed by Doppler radar, **J. Atmos. Oceanic Technol.**, **6**, 235–242, 1989.

McAfee, J. R., K. S. Gage, and R. G. Strauch, Vertical velocities at Platteville Colorado: An intercomparison of simultaneous measurements by VHF and UHF profilers, **Radio Sci.**, **34**(4), 1027–1042, 1995.

Meek, C. E., An efficient method for analysing ionospheric drifts data, **J. Atmos. Terr. Phys.**, **42**, 835–839, 1980.

Meek, C. E., and A. H. Manson, Angle-off-arrival oscillations in the mesosphere as seen by medium frequency (MF) radar, **J. Atmos. Terr. Phys.**, **54**(3/4), 277–293, 1992.

Muschinski, A., Possible effect of Kelvin-Helmholtz instability on VHF radar observations of the mean vertical wind, **J. Appl. Meteor.**, **35**, 2210–2217, 1996.

Nastrom, G. D., Detection of synoptic-scale vertical velocities using a MST radar., **Geophys. Res. Lett.**, **11**(1), 57–60, 1984.

Nastrom, G. D., and T. E. VanZandt, Mean vertical motions seen by radar wind profilers, **J. Appl. Meteor.**, **33**(8), 984–995, 1994.

Nastrom, G. D., and T. E. VanZandt, Biases due to gravity waves in wind profiler measurements of winds, **J. Appl. Meteor.**, **35**, 243–257, 1996.

Nastrom, G. D., and J. M. Warnock, Vertical motions estimated using data from a single station and a form of the adiabatic method, **J. Appl. Meteor.**, **33**, 65–73, 1994.

Nastrom, G. D., W. L. Ecklund, and K. S. Gage, Direct measurements of large-scale vertical velocities using clear-air Doppler radars, **Mon. Weather Rev.**, **113**, 708–718, 1985.

Nastrom, G. D., M. R. Peterson, J. L. G. K. S. Gage, and T. E. VanZandt, Sources of gravity wave activity seen in the vertical velocties observed by the Flatland VHF radar, **J. Appl. Meteor.**, **28**, 783–792, 1990a.

Nastrom, G. D., K. S. Gage, and W. L. Ecklund, Uncertainties in estimates of the mean vertical velocity from MST radar observations, **Radio Sci.**, **25**(5), 933–940, 1990b.

Nastrom, G. D., W. L. Clark, K. S. Gage, T. E. VanZandt, J. M. Warnock, R. Creasey, and P. M. Pauley, Case studies of the vertical velocity seen by the Flatland radar compared with indirectly computed values, **J. Atmos. Oceanic Technol.**, **11**, 14–21, 1994.

O'Brien, J. J., Alternative solutions to the classical vertical velocity problem, **J. Appl. Meteor.**, **9**, 197–203, 1970.

Palmer, R. D., R. F. Woodman, S. Fukao, T. Tsuda, and S. Kato, Three-antenna postatistic steering using the MU radar, **Radio Sci.**, **25**(6), 1105–1110, 1990.

Palmer, R. D., M. F. Larsen, R. F. Woodman, S. Fukao, M. Yamamoto, T. Tsuda, and S. Kato, VHF radar interferometry measurements of vertical velocity and the effect of tilted refractivity surfaces on standard Doppler measurements, **Radio Sci.**, **26**(2), 417–427, 1991.

Palmer, R. D., M. F. Larsen, E. L. Sheppard, S. Fukao, M. Yamamoto, T. Tsuda, and S. Kato, Postatistic steering wind estimation in the troposphere and lower stratosphere, **Radio Sci.**, **28**(3), 261–271, 1993.

Palmer, R. D., S. Vangal, M. F. Larsen, S. Fukao, T. Nakamura, and M. Yamamoto, Phase calibration of VHF spatial interferometry radars using stellar sources, **Radio Sci.**, **31**(1), 147–156, 1996.

Palmer, R. D., M. F. Larsen, and S. Vangal, Effects of finite beam width and wind field divergence on Doppler radar measurements: Simulations, **Radio Sci.**, **32**(3), 1179–1191, 1997a.

Palmer, R. D., M. F. Larsen, S. Fukao, and M. Yamamoto, On the relationship between aspect sensitivity and spatial interferometric in-beam incidence angles, **J. Atmos. Sol-. Terr. Phys.**, **in press**, 1997b.

Panofsky, B. A., Large-scale vertical velocity and divergence, **Compendium of Meteorology**, pp. 639–646, 1951.

Panofsky, H. A., Methods of computing vertical motion in the atmosphere, **J. Meteor.**, **3**, 45–49, 1946.

Pedder, M. A., On the errors of kinematic vertical motion estimation using divergence bias adjustment procedures, **Mon. Weather Rev.**, **109**, 1813–1816, 1981.

Peterson, V. L., and B. B. Balsley, Clear air Doppler radar measurements of the vertical component of wind velocity in the troposphere and stratosphere, **Geophys. Res. Lett.**, **6**(6), 933–936, 1979.

Press, W. H., S. A. Teukolsky, W. T. Vetterling, and B. P. Flannery, **Numerical Recipes in C, The art of scientific computing**. Press Syndicate of the Univeristy of Cambridge, 40 West 20th Street, New York, NY 10011-4211, USA, second edn., 1992.

Ralph, F. M., M. Crochet, and S. V. Venkateswaran, Observations of a mesoscale ducted gravity wave, **J. Atm. Sci.**, **50**, 3277–3291, 1993.

Riddle, A. C., K. S. Gage, and B. B. Balsley, Practical use of a tropopause height determination algorithm on an MST radar data set, in **Handbook for the Middle Atmosphere Program, 14**, pp. 64–73, University of Illinois, Urbana. Special Committee for Solar-Terrestrial Physics Secretariat, 1984.

Røyrvik, O., Spaced antenna drift at Jicamarca, mesospheric measurements., **Radio Sci.**, **18**(3), 461–476, 1983.

Röttger, J., Improvement of vertical velocity measurements, in **Handbook for the Middle Atmosphere Program, 14**, pp. 164–173, University of Illinois, Urbana. Special Committee for Solar-Terrestrial Physics Secretariat, 1984.

Röttger, J., and H. M. Ierkic, Postset beam steering and interferometer applications to VHF radars to study winds, waves, and turbulence in the lower and middle atmosphere, **Radio Sci.**, **20**(6), 1461–1480, 1985.

Röttger, J., and M. F. Larsen, UHF/VHF radar techniques for atmospheric research and wind profiler applications, in **Radar in Meteorology**, edited by D. Atlas, pp. 253–281. Amer. Meteor. Soc., 1990.

Röttger, J., C. H. Liu, J. K. Chao, A. J. Chen, C. J. Pan, and I.-J. Fu, Spatial interferometer measurements with the Chung-Li VHF radar, **Radio Sci.**, **25**(4), 503–515, 1990a.

Röttger, J., C. L. Hoz, S. J. Franke, and C. H. Liu, Steepening of reflectivity structures detected in high-resolution Doppler spectra of polar mesosphere summer echoes (PMSE) observed with the ESICAT 224 MHz radar, **J. Atmos. Terr. Phys.**, **52**(10/11), 939–954, 1990b.

Sato, T., and R. F. Woodman, Spectral paramater estimation of CAT radar echoes in the presence of fading clutter., **Radio Sci.**, **17**, 817–826, 1982.

Sheppard, E. L., and M. F. Larsen, Analysis of model simulations of spaced antenna/radar interferometer measurements, **Radio Sci.**, **27**(5), 759–768, 1992.

Sheppard, E. L., M. F. Larsen, R. D. Palmer, S. Fukao, M. Yamamoto, T. Tsuda, and S. Kato, A statistical comparison of spaced and spatial interferometry wind estimation, **Radio Sci.**, **28**(4), 585–593, 1993.

Starr, D. O., and S. K. Cox, Cirrus clouds. part I: A cirrus cloud model, **J. Atm. Sci.**, **42**, 2663–2681, 1985.

Strauch, R. G., D. A. Merrit, P. Moran, K. B. Earnshaw, and D. van de Kamp, The Colorado wind-profiling network, **J. Atmos. Oceanic Technol.**, **1**, 37–49, 1984.

Sürücü, F., P. Franke, and E. Kudeki, On the use of software beam synthesis in multiple-receiver MF radar wind estimation, **Radio Sci.**, **27**(6), 775–782, 1992.

Thorsen, D., A statistical climatology of mesospheric gravity wave activity over Urbana, Ph.D. thesis, University of Illinois at Urbana-Champaign, 1996.

Thorsen, D., S. J. Franke, and E. Kudeki, A new approach to MF radar interferometry for estimating mean winds and momentum flux, **Radio Sci.**, **32**(2), 707–726, 1997.

Tsuda, T., T. Sato, K. Hirose, S. Fukao, and S. Kato, MU radar observations of the aspect sensitivity of backscattered VHF echo power in the troposphere and lower stratosphere, **Radio Sci.**, **21**(6), 971–980, 1986.

Tsuda, T., W. E. Gordon, and H. Saito, Azimuth angle variations of specular reflection echoes in the lower atmosphere observed with the MU radar, **J. Atmos. Terr. Phys.**, **59**(7), 777–784, 1997a.

Tsuda, T., T. E. VanZandt, and H. Saito, Zenith-angle dependence of VHF specular reflection echoes in the lower atmosphere, **J. Atmos. Terr. Phys.**, **59**(7), 761–775, 1997b.

Van Baelen, J. S., and A. D. Richmond, Radar interferometry technique: Three-dimensional wind measurement theory, **Radio Sci.**, **26**(5), 1209–1218, 1991.

Van Baelen, J. S., A. D. Richmond, T. Tsuda, S. K. Avery, S. Kato, S. Fukao, and M. Yamamoto, Radar interferometry technique and anisotropy of the echo power distribution: First results, **Radio Sci.**, **26**(5), 1315–1326, 1991.

Vandepeer, B. G. W., and I. M. Reid, Some preliminary results obtained with a new Adelaide MF Doppler radar, **Radio Sci.**, **30**(4), 1191–1203, 1995.

VanZandt, T. E., G. D. Nastrom, and J. L. Green, Frequency spectra of vertical velocity from Flatland VHF radar data, **J. Geophys. Res.**, **96**(D2), 2845–2855, 1991.

Vincent, R. A., and I. M. Reid, HF Doppler measurements of mesospheric gravity wave momentum fluxes, **J. Atm. Sci.**, **40**(5), 1321–1333, 1983.

Vincent, R. A., P. T. May, W. K. Hocking, W. G. Elford, B. H. Candy, and B. H. Briggs, First results with the Adelaide VHF radar: spaced antenna studies of tropospheric winds, **J. Atmos. Terr. Phys.**, **49**(4), 353–366, 1987.

Weber, B. L., D. B. Wuertz, D. C. Law, A. S. Frisch, and J. M. Brown, Effects of small-scale vertical motion on radar measurements of wind and temperature profiles, **J. Atmos. Oceanic Technol.**, **9**(3), 193–209, 1992.

Woodman, R. F., Spectral moment estimation in MST radars, **Radio Sci.**, **20**(6), 1185–1195, 1985.

Woodman, R. F., On the true velocity in full correlation analysis, **Radio Sci.**, **30**(5), 1459–1465, 1995.

Woodman, R. F., and A. Guillén, Radar observations of winds and turbulence in the stratosphere and mesosphere, **J. Atm. Sci.**, **31**(2), 493–505, 1974.

Yamamoto, Y., T. Tsuda, and T. Adachi, Frequency spectra of wind velocity and temperature fluctuations observed with the MU radar-RASS, **Geophys. Res. Lett.**, **23**(4), 3647–3650, 1996.

Yoe, J. G., M. F. Larsen, and E. J. Zipser, VHF wind-profiler data quality and comparison of methods for deducing horizontal and vertical air motions in a mesoscale convective storm, **J. Atmos. Oceanic Technol.**, **9**(6), 713–727, 1992.

APPENDIX A

GROUND-CLUTTER TREATMENT

In this section, we present some algorithms that deal with constant or "slowly fading" ground-clutter signals. By "slowly fading" we mean a signal with a correlation time much larger than the correlation time of the atmospheric signal. Usually, this is the case for signals obtained by VHF radars. However, at UHF the fading of ground-clutter signals are often faster than at VHF, although they are still "slower" than the atmospheric signals. Methods dealing with these "faster fading" signals can be found in Sato and Woodman [1982] and May and Strauch [1997]. It is worth mentioning, that part of the "ground-clutter" signal could also come from the receivers and/or the digitization process, although these contributions are usually constant in time.

In Figure A.1 we show an example of a time-series of one of the complex receiving channels (R), for a single height. For the procedures we cover below, we have subdivided the time-series in n blocks (n = number of incoherent integrations). Each block having the same number of points (N_p) and separated by the vertical dotted lines. Also, we have calculated the mean value of each block ($\bar{R}_i$), denoted with solid circles. The same procedure is performed on the imaginary channel.

We have treated the ground-clutter signals in the following three ways: (1) time-domain subtraction, (2) frequency-domain subtraction, and (3) frequency-domain interpolation.

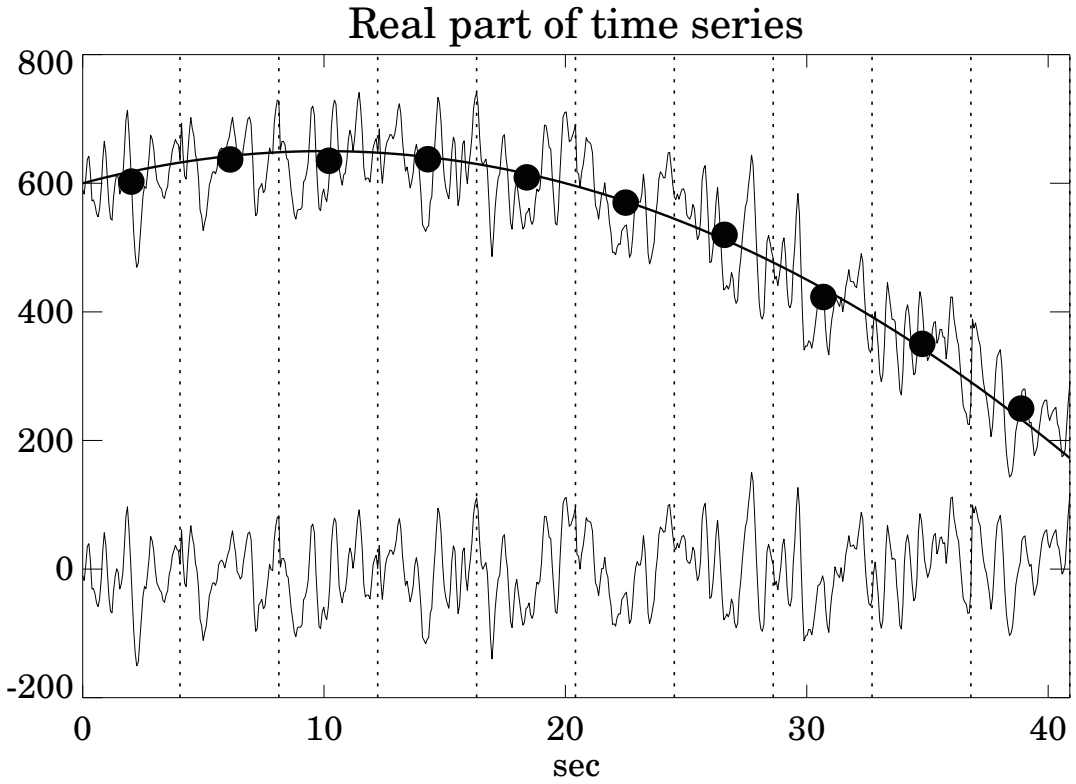

Figure A.1. Real part of a time-series for 10 blocks of 64 points each. Solid circles denote the mean values of each block, and vertical dotted lines delimit each block. The thick line represents the fitted second-degree polynomial to the circles. The ground-clutter-free signal is at the bottom, centered on zero.

A.1 Time-Domain subtraction

We perform a least-square second-degree polynomial fit to the mean values of each block ($\bar{R}_i$). Then this polynomial is sampled at the same points of the time-series, and subtracted from the time-series. In Figure A.1, the polynomial is represented by a thick line, and the ground-clutter-free time-series is centered at zero level. This procedure also works for a constant ground-clutter signal, where only the zeroth-order coefficient is different than zero.

The usage of this procedure is suitable for time-domain or for frequency-domain analysis. In both domains, time and frequency, once the "clutter" subtraction is performed in the time-series, the auto/cross correlations functions (ACFs/CCFs)

and self/cross spectrum functions (SSFs/CSFs) are computed for each block, respectively. Then these complex quantities are incoherently averaged to obtained the functions for that particular time-series, and the respective analysis follows (e.g., FCA in the time-domain, or FSA in the frequency-domain).

The main disadvantages of this procedure are: (1) the high amount of memory needed to do on-line processing (this is primarily due to the necessity to store n blocks before the time- or frequency-domain analysis is performed), and (2) for an off-line processing this procedure requires that the "raw" data be saved (i.e., voltages).

A.2 Frequency-Domain subtraction

We assume here that the Fourier transform of the complex voltages is given by:

$$s_f = a_f + c_f \tag{A.1}$$

where a_f represents the atmospheric and noise components, and c_f the ground-clutter component, at frequency-bin f. Furthermore, we assume that each A_f is a zero-mean Gaussian process, i.e., $< a_f >=< a_f^* >= 0$, c_f is a deterministic function and $<>$ denotes incoherent averaging. Then, the power spectrum, after incoherent averaging, is given by

$$S_f =< s_f s_f^* >=< a_f a_f^* > - < c_f c_f^* > \tag{A.2}$$

(Woodman 1995, personal communication). Therefore the power spectrum of the atmospheric and noise contribution can be obtained by subtracting the ground-clutter deterministic power spectrum function, from the power spectrum of the original data. In Figure A.2, the original spectrum is represented with a thick line, the ground-clutter spectrum with pluses and the atmospheric, and the noise spectrum with diamonds.

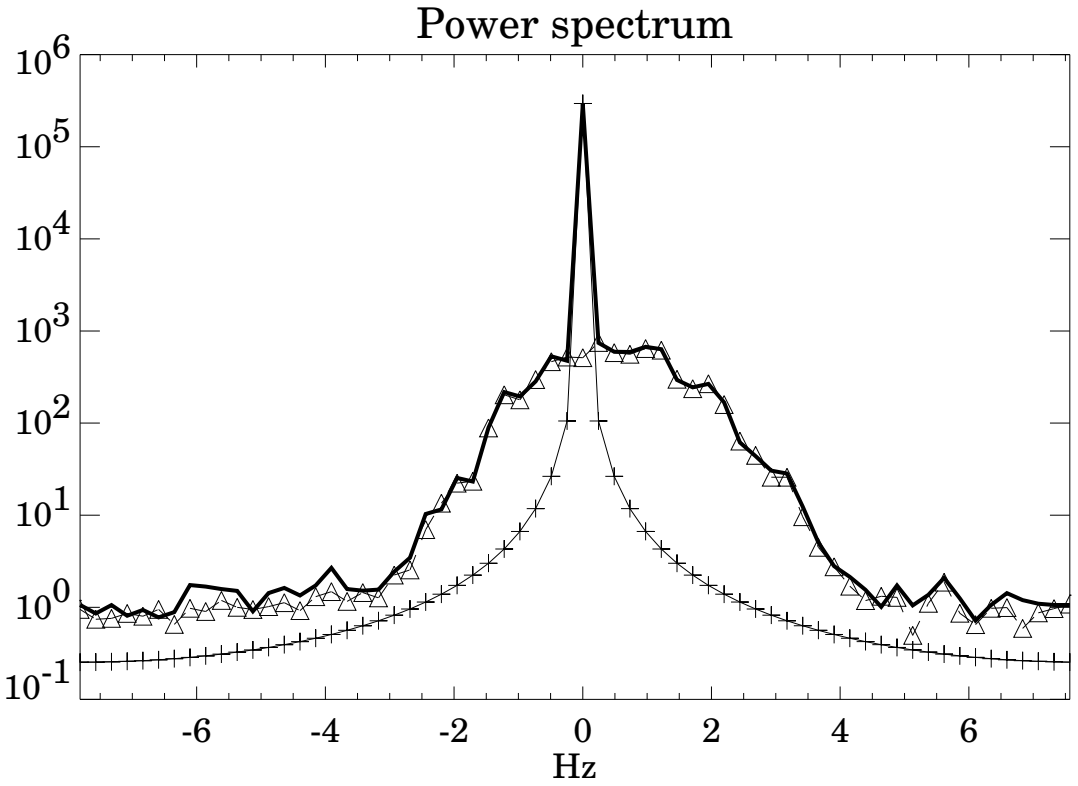

Figure A.2. Example of atmospheric power spectrum with ground-clutter and noise (thick line). Ground-clutter spectrum is denoted with pluses and the ground-clutter-free spectrum with triangles.

The deterministic spectrum $< c_f c_f^* >$ can be obtained by Fourier transforming the complex polynomial that was fitted to the complex mean values of each block. Then, the desired spectrum $< a_f a_f^* >$ is obtained from Equation A.2.

The main advantage of this procedure is that the ground-clutter removal is done after incoherent averaging, i.e., there is no need to keep the "raw" data in either an on-line or an off-line processing. Only $< s_f s_f^* >$ and the complex mean values of each block of the incoherent averaging process, are needed. This procedure, however, can not be applied in time-domain analysis. In addition, it requires a reasonable number of incoherent averages in order to better characterize the atmospheric spectrum.

For the case the ground-clutter signal is constant or near constant, there is

no need for fitting, and the only removal is done at frequency-bin $f = 0$.

A.3 Frequency-Domain interpolation

This last procedure is suitable only for frequency-domain analysis when ground-clutter signals are near constant (i.e., when most of the ground-clutter energy is concentrated at $f = 0$). Under these conditions the power at zero frequency, i.e., $< s_0 s_0^* >$, is replaced by an interpolated value. This value can be obtained from a simple linear interpolation using the two adjacent points, or from a cubic interpolation using two closest points at each side of $f = 0$.

APPENDIX B

SPECTRAL MOMENT ESTIMATION

The atmospheric signals obtained with VHF radars at any one height can be assumed to be Gaussian stationary processes with a Gaussian-shaped power spectrum (e.g. Woodman [1985]). In addition, to the atmospheric signals, the radar signals will be primarily composed of the following non-desirable signals: (1) ground clutter and (2) sky and receiver noise. The ground clutter is usually approximated to be a constant DC signal, although under certain circumstances it could have significant temporal variations. The sky and receiver noises, on the other hand, are well approximated by a white-noise process, i.e., a spectrum of constant value. Having said this, the power spectrum of the received signal can be assumed to be,

$$S(f) = \frac{P}{(2\pi\sigma_f^2)^{1/2}} \exp\left[-\frac{(f-f_d)^2}{2\sigma_f^2}\right] + N + D\delta(f) \tag{B.1}$$

where f is the frequency in Hz and $\delta(f)$ is a delta function. Then, this spectrum is fully characterize by the value of five parameters: total atmospheric power (P), mean atmospheric frequency shift (f_d), atmospheric spectral width (σ_f), total noise (N) and the ground clutter power (D) (see Figure B.1).

In this section we give a brief description of the two spectral moments estimators used throughout this thesis: one used by the Aeronomy Lab of the National Oceanic and Atmospheric Administration (NOAA) and one that performs a Gaussian fitting.

B.1 NOAA's algorithm

This algorithm is also known as first moment (FM) and has been successfully compared, in terms of frequency shift estimation, to other algorithms, by May

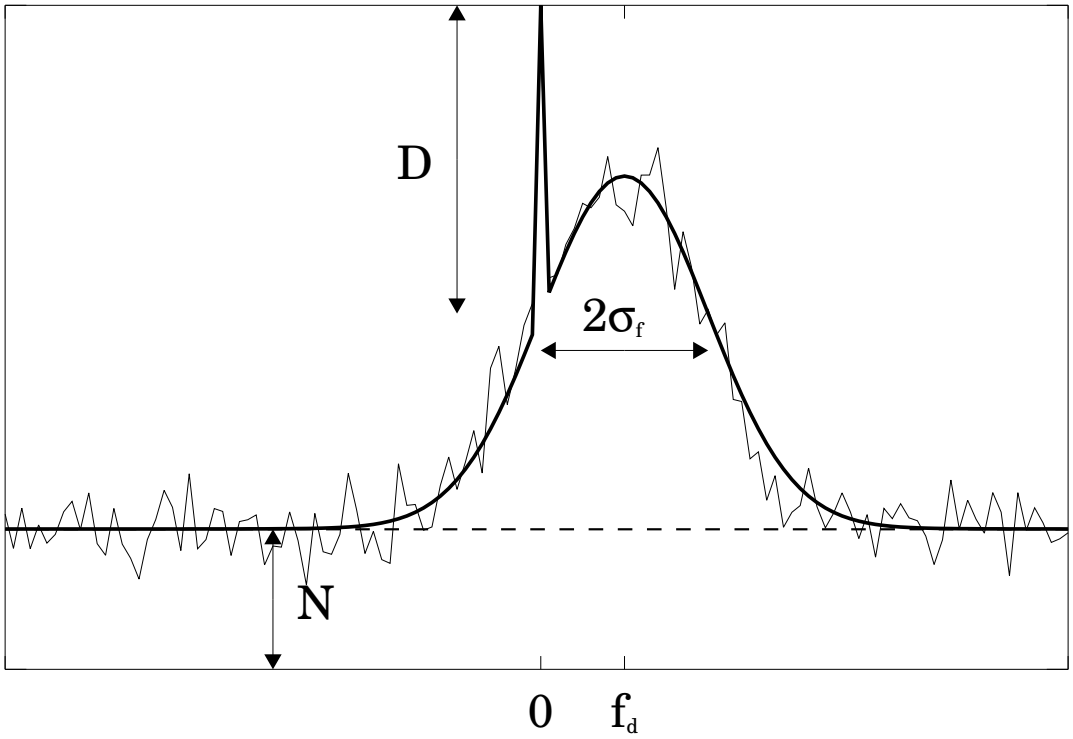

Figure B.1: An example of a frequency spectrum represented by Equation B.1.

and Strauch [1989]. Here we assumed that the ground clutter contribution has been already removed by one of those procedures described in Appendix A. Therefore the parameters to be estimated are: P, f_d, σ_f and N.

This FM algorithm involves several steps. First several Doppler spectra from each height range are averaged (Incoherent integration). Then the noise level (N) is objectively estimated using the technique of Hildebrand and Sekhon [1974]. A first guess for the position of the signal peak is obtained by finding the maximum spectral power density when the spectrum has been smoothed with a running mean of n points (usually 3). The moments (P, f_d and σ_f) are then calculated from the original (non-smoothed) spectrum over the interval surrounding this guess out to the first point where the spectrum power density falls below the noise level on either side of the guess. The noise level is subtracted from the spectral values over the signal interval before calculating the moments. Instead of total power (P), the parameter

that is of most common use is the signal-to-noise ratio (SNR = P/N).

The main advantages of this algorithm are that the moments are calculated quite fast, and the Doppler shift (first moment) estimates are very accurate. In contrast, however, the spectral width (second moment) is not accurately determined with this algorithm. More on this algorithm can be found in Strauch et al. [1984] and May and Strauch [1989].

We have applied this algorithm in Chapter 4 to compute the Doppler shifts of the synthesized beams used with the PSS technique. In Chapter 6, Doppler shifts of the Narrow and Wide vertically-directed beams were also computed with this algorithm.

B.2 Gaussian fitting algorithm

In this algorithm we fit the averaged Doppler spectrum to a known function that includes the theoretical shape of the spectrum (e.g. Equation B.1) and any instrumental function (e.g. a rectangular window). The concept is described in Figure B.2: For any single height, the outputs of the radar, i.e., the atmospheric signal, ground clutter, noise and the instrument function, are represented by the pairs $\hat{f}_i, \hat{S}_i$. These measured values are fitted by the theoretical values f_i, S_i in a least squares sense (Woodman [1996], personal communication).

In our case we have assumed that the theoretical spectrum is represented by Equation B.1. We have represented the instrument function by a "window", rectangular or Hanning (e.g. Press et al. [1992]). The theoretical pairs (f_i, S_i) are obtained by finding the inverse Fourier transform of the theoretical model, multiply it by the autocorrelation of the window used, and Fourier transforming back this product.

We can use this approach when the ground clutter has not been previously removed, or even when it has been removed. The latter approach will be in order to

Figure B.2: Block diagram for a least squares parameter estimation.

removed residual "spikes" (not enough removal) or "notches" (too much removal). Furthermore, this approach can also be applied when ground clutter is not constant, but it is slightly changing. Or in the presence of other known, but undesirable signals (e.g. sea echoes, interference, etc.).

The main advantages of this type of algorithms are: (1) accurate measurements of the atmospheric spectral width, and (2) good characterization of the atmospheric spectrum when the "a priori" information is good. The main disadvantage of this algorithm is that requires higher estimation time than using the NOAA's algorithm.

In order to initialize the fitting procedure, we obtain the initial guesses from the estimates of NOAA's algorithm. In Chapter 4, we have implemented this algorithm in the full spectral analysis technique (FSA) and in the radar interferometric techniques (RIV, RIH).

APPENDIX C

PHASE CALIBRATION OF SPACED ANTENNA SYSTEMS

Some of the spaced antenna techniques for wind measurements are inherently dependent on any phase imbalance in the system (e.g. see Section 4.2 and Section 6.2.2). The imbalance is usually caused by a path length difference between the multiple receivers. One way to measure this imbalance is by feeding a common signal to all the receiving lines simultaneously (Kudeki [1994], personal communication). These receiving lines include cables, receivers and Analog/Digital converters. Once the signals are recorded, the phase difference should be obtained with a similar analysis used to measure the winds. This last step is necessary in order to avoid, mainly, problems associated with sign conventions.

In our experiments, we have done the phase calibration during 30 minutes, at the beginning and at the end of each experiment. Two types of common signals were used. First, the atmospheric signal of one of the receiving antennas (transmitter on) was equally split and fed to all the receiving lines. With this procedure, we were able to test the phase imbalance under different signal amplitudes. The second common signal was an amplified "sky noise" measured at one of the receiving antennas (transmitter off). In both cases, we measured almost the same phase differences.

In Table C.1, we show the mean and the standard deviation of the phase differences between receiving lines, for the 5-day experiment run in March 1997. Notice the good agreement of the values under both atmospheric and "sky noise" signals. The biggest difference of the mean values for each receiver pair is $\approx 1.1^{\circ}$, that corresponds to an AOA error of $\approx 0.03^{\circ}$.

Table C.1: Phase calibration values for the 5-day experiment run in March 1997.

	AB	AC	BC
Atmospheric signal			
Mean	-82.2°	-109.4°	-26.1°
Standard deviation	1.2°	1.2°	1.7°
Sky noise			
Mean	-81.1°	-108.8°	-26.2°
Standard deviation	1.2°	1.1°	1.0°

APPENDIX D

IMPLEMENTATION OF THE POST STATISTICS STEERING TECHNIQUE

In configurations using multiple-receiving antennas, different beam directions can be synthesized by phasing the received signals. One of such technique is post set beam steering (PBS) (Röttger and Ierkic [1985]). This technique synthesizes the beam by introducing a phase shift on the signal itself. Post statistics steering (PSS) (Kudeki and Woodman [1990]) improved this approach by introducing the phase shift on the signal statistics (CCF, CSF) rather than the signal itself, thus reducing computation and storage. In the following paragraphs, we describe how a three-antenna PSS approach was implemented in the frequency domain.

Using three receiving antennas, the synthesized spectrum ($\Phi_{\alpha\alpha}$) in a desired beam direction can be obtained from

$$\Phi_{\alpha\alpha} = \Phi_{aa}+\Phi_{bb}+\Phi_{cc}+2\mathrm{Re}\{\Phi_{bc}e^{j\Delta_{bc}}\}+2\mathrm{Re}\{\Phi_{ba}e^{j\Delta_{ba}}\}+2\mathrm{Re}\{\Phi_{ca}e^{j(\Delta_{ba}-\Delta_{bc})}\} \quad \text{(D.1)}$$

where Φ are the complex spectra functions of the original signals (auto and cross spectra), and Δ are the phase shifts.

In order to obtain the effective beam pointing direction, one needs to take into account the patterns of the transmitting and receiving antennas, the location of the antennas, and an atmospheric function. Using the antenna setup of Figure 4.1, and assuming isotropic scattering, the synthesized pattern at height z_0 is

$$g_s(x,y) = |g_T(x,y)[g_{Rb}(x,y) + g_{Ra}(x,y)e^{-j\Delta_{ab}} + g_{Rc}(x,y)e^{-j\Delta_{cb}}]| \quad \text{(D.2)}$$

where g_T and g_R are the patterns of the transmitting and receiving antennas. From Figure 4.1, baseline BC is aligned in the x direction, and baseline BA in the y direction.

The effective pointing directions are calculated from

$$\theta_x = \sin^{-1}\left(\frac{\overline{MB} - \overline{MC}}{d_{bc}}\right) \tag{D.3}$$

$$\theta_y = \sin^{-1}\left(\frac{\overline{MB} - \overline{MA}}{d_{ba}}\right) \tag{D.4}$$

where M is the peak of the synthesized pattern in distance, d_{ba} and d_{bc} are the distances between antennas A and B, and between antennas C and B, respectively. The distances of point M to the receiving antennas A, B, C are denoted by $\overline{MA}$, $\overline{MB}$, $\overline{MC}$, respectively. In addition, we have calculated the position of point M, by fitting a two-dimensional Gaussian function to the synthesized pattern, over the region surrounding the peak.

The three-dimensional velocity vector can be obtained with n synthesized directions by solving the following system of equations

$$\begin{bmatrix} \sin\theta_{x1} & \sin\theta_{y1} & \sqrt{1-\sin^2\theta_{x1}-\sin^2\theta_{y1}} \\ \vdots & \vdots & \vdots \\ \sin\theta_{xn} & \sin\theta_{yn} & \sqrt{1-\sin^2\theta_{xn}-\sin^2\theta_{yn}} \end{bmatrix} \begin{bmatrix} v_{0x} \\ v_{0y} \\ v_{0z} \end{bmatrix} = \begin{bmatrix} v_{r1} \\ \vdots \\ v_{rn} \end{bmatrix} \tag{D.5}$$

where v_{ri} is the radial velocity (positive, going away from the radar) of the i synthesized direction. We have solved this system of equations using a singular-value decomposition and a back substitution (Press et al. [1992], section 2.6).

We have synthesized nine different beam directions at each height. For example, the angles of the effective beam directions synthesized at 7.50 km are given in Table D.1. Similar values have been obtained at the other heights. Briefly, we have selected values around the original pointing direction trying to: (a) effectively point the furthest from vertical, and at the same time, (b) avoid the generation of significant sidelobes. By synthesizing the furthest possible off-vertical angles, we try to decrease the influences of the pointing angles uncertainties on the velocity estimation.

Table D.1: Effective beam pointing directions at 7.50 km (in degrees).

	1	2	3	4	5	6	7	8	9
θ_x	-0.36	-0.36	-0.60	0.11	0.08	-0.12	0.61	0.67	0.58
θ_y	-0.41	-0.06	1.17	-0.36	-0.50	1.43	-0.23	0.29	1.20

In Equation D.1, zero phase differences between receivers and identical receiver gains are assumed. The zero phase difference was accomplished by subtracting the non-zero phases obtained from the calibration procedure described in Appendix C. In order to have identical receiver gains, we have balanced the spectral functions using the noise levels of the "noisy" heights (between 12 and 15 km). This procedure was performed before the synthesized spectra were achieved. The procedure of getting the effective beam directions of the synthesized beams, can also be applied to a PBS approach.

APPENDIX E

AOA INTERPRETATION UNDER HORIZONTALLY ANISOTROPIC SCATTERING

Using Equation 21 from Holloway et al. [1997b] and the AOA contributions of Section 5.2.1, we arrive to the following normalized cross-correlation function,

$$\begin{aligned} c_{ij}(\tau) &\approx \exp\left\{ -\frac{2(v'_{0x}\tau - \Delta\rho'_{xij}/2)^2}{\xi_x^2} - \frac{2(v'_{0y}\tau - \Delta\rho'_{yij}/2)^2}{\xi_y^2} \right. \\ &\quad \left. -2(k_0\sigma_t\tau)^2 - \frac{1}{8}\left(\frac{v_{0z}\tau}{\sigma_r}\right)^2 + j\phi_{ij}(\tau) \right\} \end{aligned} \tag{E.1}$$

where

$$\begin{aligned} \phi_{ij}(\tau) &\approx -2k_0 v_{0z}\tau - 2k_0 v'_{0x}\Theta'_{xij}\tau - 2k_0 v'_{0y}\Theta'_{yij}\tau \\ &\quad +k_0\Delta\rho'_{xij}\Theta'_{xij} + k_0\Delta\rho'_{yij}\Theta'_{yij} + k_0|\Delta\boldsymbol{\rho}'_{ij}|\Lambda_{ij} \\ \Theta'_{xij} &= 2(\boldsymbol{\Omega}'_x + \boldsymbol{\Phi}'_x + \boldsymbol{\Gamma}'_{xij})\xi_x^{-2} \\ \Theta'_{yij} &= 2(\boldsymbol{\Omega}'_y + \boldsymbol{\Phi}'_y + \boldsymbol{\Gamma}'_{yij})\xi_y^{-2} \\ \xi_x^2 &= 2a_h^{-2} + (2\rho'_{cx})^2 \\ \xi_y^2 &= 2a_h^{-2} + (2\rho'_{cy})^2 \end{aligned} \tag{E.2}$$

and ρ'_{cx} and ρ'_{cy} are the correlation lengths along the primed coordinate axes (x', y').

The irregularities are assumed to have the major/minor axes of their correlation ellipse aligned along the $x' - y'$ axes which are rotated by an unknown angle ψ with respect to the $x - y$ axes (the axes that define the transmitter and receiver locations).

Now, the primed coordinate system $(x' - y')$ is related to the $x - y$ system by the following transformation,

$$\boldsymbol{X}' = \boldsymbol{T}\boldsymbol{X} \tag{E.3}$$

where $\boldsymbol{X}' = (x', y')$, $\boldsymbol{X} = (x, y)$ and $\boldsymbol{T} = [(\cos\psi, \sin\psi), (-\sin\psi, \cos\psi)]$. Applying these transformation to all the primed variables (velocity, position and AOA contributions), the phase term given by Equation E.2 becomes,

$$\begin{aligned}\phi_{ij}(\tau) &\approx -2k_0 v_{0z}\tau - 2k_0 v_{0x}\Theta^a_{xij}\tau - 2k_0 v_{0y}\Theta^a_{yij}\tau \\ &\quad +k_0\Delta\rho_{xij}\Theta^a_{xij} + k_0\Delta\rho_{yij}\Theta^a_{yij} + k_0|\Delta\boldsymbol{\rho}_{ij}|\Lambda_{ij} \qquad \text{(E.4)}\end{aligned}$$

where $(\Theta^a_{xij}, \Theta^a_{yij})$ represents the observed AOA vector, and is given by,

$$\Theta^a_{xij} = \Theta_{xij}(\cos^2\psi + (\xi_x^2/\xi_y^2)\sin^2\psi) + \Theta_{yij}\cos\psi\sin\psi(\xi_y^2/\xi_x^2 - 1) \qquad \text{(E.5)}$$

$$\Theta^a_{yij} = \Theta_{yij}(\cos^2\psi + (\xi_y^2/\xi_x^2)\sin^2\psi) + \Theta_{xij}\cos\psi\sin\psi(1 - \xi_x^2/\xi_y^2) \qquad \text{(E.6)}$$

and

$$\Theta_{xij} = 2(\Omega_x + \Phi_x + \Gamma_{xij})\xi_x^{-2} \qquad \text{(E.7)}$$

$$\Theta_{yij} = 2(\Omega_y + \Phi_y + \Gamma_{yij})\xi_y^{-2} \qquad \text{(E.8)}$$

The influence of horizontal anisotropic irregularities on the statistical errors it is mainly through the correlation time (τ_c) and through the coherence term ($\mathrm{coh}_{ij}[0]$). Transforming Equation E.1 to the $x-y$ axes, the square of the coherence term become,

$$\begin{aligned}\mathrm{coh}^2_{ij}[0] &= \exp\Big\{-[\Delta\rho^2_{xij}(\xi_x^{-2}\cos^2\psi + \xi_y^{-2}\sin^2\psi) + \Delta\rho^2_{yij}(\xi_y^{-2}\cos^2\psi + \xi_x^{-2}\sin^2\psi) \\ &\quad +\Delta\rho_{xij}\Delta\rho_{yij}\cos\psi\sin\psi(\xi_x^{-2} - \xi_y^{-2})]/2\Big\} \qquad \text{(E.9)}\end{aligned}$$